THE EFFECTS OF MAGNETIC FIELDS AND FIELD-ALIGNED ROTATION ON LINE-DRIVEN HOT-STAR WINDS

by

Asif ud-Doula

A dissertation submitted to the Faculty of the University of Delaware in partial fulfillment of the requirements for the degree of Doctor of Philosophy in Physics

Fall 2002

THE EFFECTS OF MAGNETIC FIELDS AND FIELD-ALIGNED ROTATION ON LINE-DRIVEN HOT-STAR WINDS

by

Asif ud-Doula

Approved: _____

James MacDonald, Ph.D.
Chair of the Department of Physics and Astronomy

Approved: _____

Mark W. Huddleston, Ph.D.
Dean of the College of Arts and Science

Approved: _____

Conrado M. Gempesaw II, Ph.D.
Vice Provost for Academic Programs and Planning

I certify that I have read this dissertation and that in my opinion it meets the academic and professional standard required by the University as a dissertation for the degree of Doctor of Philosophy.

Signed: _____

Stanley P. Owocki, Ph.D.
Professor in charge of dissertation

I certify that I have read this dissertation and that in my opinion it meets the academic and professional standard required by the University as a dissertation for the degree of Doctor of Philosophy.

Signed: _____

James MacDonald, Ph.D.
Member of dissertation committee

I certify that I have read this dissertation and that in my opinion it meets the academic and professional standard required by the University as a dissertation for the degree of Doctor of Philosophy.

Signed: _____

James M. Stone, Ph.D.
Member of dissertation committee

I certify that I have read this dissertation and that in my opinion it meets the academic and professional standard required by the University as a dissertation for the degree of Doctor of Philosophy.

Signed: _____

Dermott J. Mullan, Ph.D
Member of dissertation committee

I certify that I have read this dissertation and that in my opinion it meets the academic and professional standard required by the University as a dissertation for the degree of Doctor of Philosophy.

Signed: _____

Harry L. Shipman, Ph.D
Member of dissertation committee

ACKNOWLEDGEMENTS

I wish to thank Prof. S. Owocki for all his help in my research. His patience and support have been of utmost value to me. I also thank Hans Mueller and David Cohen for helpful feedback.

This research was supported in part by NASA grant NAG5-3530 and NSF grant AST-0097983 to the Bartol Research Institute at the University of Delaware. I also would like to acknowledge the support of NASA's Space Grant College program at the University of Delaware.

TABLE OF CONTENTS

LIST OF FIGURES

LIST OF TABLES

ABSTRACT

There is extensive evidence that the radiatively driven stellar winds of OB-type stars are not the steady, smooth outflows envisioned in classical models, but instead exhibit extensive structure and variability on a range of temporal and spatial scales. This dissertation examines the possible role of stellar magnetic fields in forming large-scale wind structure. It is based on numerical magnetohydrodynamic (MHD) simulations of the interaction of a line-driven flow with an assumed stellar dipole field.

The first two chapters provide a brief historical overview and a background summary of the dynamics of line-driven winds. Chapter 3 then presents initial MHD simulations of the effect of a dipole field on *isothermal* models of such line-driven outflows. Unlike previous fixed-field analyses, the MHD simulations here take full account of the dynamical competition between field and flow, and thus apply to a full range of magnetic field strength, and within both closed and open magnetic topologies. A key result is that the overall degree to which the wind is influenced by the field depends largely on a single, dimensionless, 'wind magnetic confinement parameter', η_* $(= B_{eq}^2 R_*^2/\dot{M}v_\infty)$, which characterizes the ratio between magnetic field energy density and kinetic energy density of the wind.

Chapter 4 carries out semi-analytic analyses of the properties of these numerical simulations, with focus on the effect of magnetic field tilt on the mass flux and rapid flow-tube divergence on the terminal flow speed. The results show in particular that previous expectations of a strong, factor 2-3 enhancement were a consequence of assuming a point-star approximation for the wind driving, and that

in finite-disk-corrected models one obtains a much more modest 20-30% speed increase, in agreement with both the numerical MHD simulations and observational constraints.

Chapter 5 extends our MHD simulations to include field-aligned stellar rotation. The results indicate that a combination of the magnetic confinement parameter and the rotation rate as a fraction of the 'critical' rotation now determine the global properties of the wind. For models with strong magnetic confinement, rotation can limit the extent of the last closed magnetic loop, and lead to episodic mass ejections that break through the close loop and are carried outward with a slow, dense, equatorial outflow.

In contrast to these idealized isothermal models, wherein any hot gas is assumed to radiate away excess energy instantaneously, Chapter 6 carries out MHD simulations of the other extreme limit of *adiabatic* outflows, for which no energy is lost at all. The results show that adiabatic models with magnetic confinement $\eta_* < 1$ are very similar to their isothermal counterparts, but those with $\eta_* \geq 1$ are dramatically different from the isothermal case, with much greater level of equatorial confinement.

Chapter 7 summarizes the key conclusions of the thesis, and outlines directions for future work. Overall, the results here provide a dynamical groundwork for interpreting many types of observations – e.g., UV line profile variability; red-shifted absorption or emission features; enhanced density-squared emission; x-ray emission – that might be associated with perturbation of hot-star winds by surface magnetic fields.

Chapter 1

INTRODUCTION

Stars are classified based on their effective surface temperatures. The hottest of them are called O and B stars. Because OB stars are very luminous and some of them, like supergiant O stars, are up to a million times brighter than the sun, they often dominate light from many galaxies. Hot stars are also very massive, and they lose most of their mass in various ways over a relatively short period of time, of the order of a few million years. Thus they contribute significantly towards the the enrichment of interstellar medium. So, it is important to understand these hot stars.

In our daily lives light plays very little role as a direct source of momentum or force, yet in the case of hot stars with their overwhelming luminosities, light becomes the dominating mechanism in driving a continuous outflow of material called the *stellar wind*. It is surprising to think that the light can drive wind outflows as high as $10^{-5} M_{\odot}/yr$ as is the case for some hot stars. What makes it possible is the absorption and scattering of UV photons by the resonance lines of minor ions (ions heavier than He) which have relatively large opacities. Although the abundance of the minor ions is small (typically $\sim 10^{-4}$ for hot stars), they play a crucial role in converting the photon momentum into the wind momentum. We discuss this mechanism of line-driving in greater detail in Chapter 2.

In the past few decades rapid developments have been made in understanding the basic properties of hot-star winds, but there are a number of issues that are

contentious and still unclear. For instance, it is not well understood what possible role magnetic fields can play in perturbing such hot-star winds. In this work, we address this issue using numerical simulations as a tool.

In this chapter we outline the importance of the subject of line-driven winds, and discuss why we chose to study the effects of magnetic fields on such winds. We conclude this chapter with a brief description of the content of this dissertation.

1.1 Brief Historical Overview of Line-Driven Winds

Because virtually all the knowledge we have about stars other than the sun, is based on incoming light from the stars, it is not a simple matter to detect stellar winds directly. One of the first indirect evidence of the mass loss of stars, in general, came with the optical observations of objects called 'new stars' or novae, transient outbursts in brightness that are visible even by naked eye. Tycho Brahe's observation of such a 'new star' in 1572 was in fact what we now call a supernova. Another 'new star' was discovered by Blaeu in 1600 that later was named P Cygni. It was not clear at the time of their discoveries what the reasons were behind these apparent variations in brightness.

One of the first clues came with the application of spectroscopy to the light coming from distant stars in the late nineteenth century. Observations showed that spectral lines from many stellar objects had prominent line profiles similar to those observed in the spectrum of P Cygni. These 'P Cygni'-like profiles were characterized by having redshifted peaks along with blueshifted absorption troughs. By the end of 19th century, technological improvement in spectroscopic techniques allowed scientists to resolve the spectra of novae. It was clear that the broadening of lines, $\Delta\lambda$ was the result of the so called Doppler effect. But it was not clear what caused such broadenings.

It can be argued that one possible mechanism for the formation of such line profiles is the spherical expansion of the stellar atmosphere, shown schematically in

figure 1.1. Most of the P Cygni profiles observed in UV (ultraviolet) lines of hot stars are formed by scattering of photons. When a bound electron makes a transition between the ground state and the first excited state it absorbs a photon which thus is removed from the line of sight. But, the electron very quickly de-excites with the net result that the original photon is not lost but scattered in a different direction. From an observer's point of view, the original photon has been removed from the line of sight resulting in an absorption trough also known as resonance lines. The fact that these lines are blue-shifted indicates that the absorbers are moving towards the observer away from the star. Now, if we assume that this process is spherically symmetric, the photons scattered out elsewhere will come into the line of sight of the observer as an emission profile. In an ideal case where all the photons that have been absorbed are scattered back into the line of sight, this emission profile is symmetric with respect to the line center, but because the star occults the part of the atmosphere on the backside that is moving away from the observer, the emission profile on the red side is slightly weaker than that on the blue side. By adding the absorption trough and the emission profile, the characteristic P Cygni line is formed.

In addition to novae and stars that have P Cygni-like spectra, Wolf and Rayet (1867) discovered another class of stars (called now Wolf-Rayet (WR) stars) which have similar spectra that, in this case, do not have any outbursts and do not fade away with time. Based on the fact that the line widths for WR stars are very broad, Beals (1929) proposed a model where the star ejects gaseous material continuously and in radial direction with high velocities. In other words, the star is surrounded by a fast-expanding envelope whose spatial extension is large compared to the size of the star. We now know that this is a reasonable picture of the WR stars.

Slowly, it was becoming evident that most stars may have some sort of material outflows. In the case of the sun, Parker (1958) showed that given the hot solar corona of $\sim 10^6$ K, it is not possible to have a static corona since the finite pressure

at infinity that one obtains from equations of hydrostatic equilibrium could not be matched by the small interstellar gas pressure we infer from measurements. Thus, the existence of hot solar corona leads naturally to its expansion through a gas pressure gradient. We describe Parker's elegant argument in chapter 2. Predictions were verified by *in situ* observations of the solar wind performed by the *Mariner 2* interplanetary probe (1962). Parker is also credited for the introduction of the terminologies of the solar and stellar winds.

The case of WR and other hot stars that are very luminous, was somehow different from the case of the relatively cool sun. If hot star winds were driven by gas pressure gradient, it would require extraordinarily high temperature stellar coronae for which there are no observational evidence. However, it was recognized by Milne (1924) that photons can in principle impart momentum onto the wind material. In the solar context, Milne showed that pure absorption of radiation flux can perhaps maintain a gravitationally bound atmosphere. This was one of the earliest attempts to provide a framework for radiation-driven winds.

Despite the lack of an elaborate theory of how hot-star winds are accelerated, a very compelling evidence for the existence of hot-star winds came with the discovery of P-Cygni type profiles in the UV resonance lines of NV, CIV and SiIV in the spectra of O and B supergiants (Morton 1967). By then it was clear that P-Cygni profiles can be formed only by an expanding envelope with a velocity that can be directly determined by the width of the profiles. Soon after, a more complete version of line-driven wind theory was developed by Lucy and Solomon (1970), and then extended by Castor, Abbott and Klein (1975; hereafter CAK). In particular, CAK showed that in an expanding atmosphere a large ensemble of lines can give rise to a line-force that is a function of the local velocity gradient. There have been further developments and extensions to the CAK theory since then, e.g. Pauldrach, Puls and Kudritzki (1986), Friend and Abbott (1986), Owocki, Castor and Rybicki

(1988). Most of the earlier works considered stars as point-like sources. It turns out that the finite size of the star does make a difference dynamically in driving the wind (Pauldrach, Puls and Kudritzki (1986); Friend and Abbott (1986)), and its effect can be included through so called *finite disk correction factor* . All of our work here follows the basic formalism of the CAK theory with this correction factor, and is discussed in Chapter 2.

1.2 The Impact of Winds on Stellar Evolution

The knowledge of the mass loss rates is essential to understanding the evolution of stars. The most luminous hot stars can lose up to half of their masses during their lifetimes. After going through different stages of evolution they expose their hot cores turning into the Wolf-Rayet stars. Finally they end their lives in a violent supernova explosion that disrupts the star enriching the interstellar medium with various elements. The shockwave resulting from this explosion can induce new star formation. Thus it is important for us to understand how these hot-stars lose mass through the stellar winds and how stellar wind properties are determined.

The basic formalism of the CAK theory, which assumes time-steady and spherically symmetric configuration, can explain the overall global properties of the winds of the main sequence O and B stars, the hottest two classes of stars. Unfortunately, this theory cannot account fully for the phases of the strongest mass loss, the LBV (Luminous Blue Variable) and the Wolf-Rayet phases. It is beyond the scope of this work to analyze these phases, instead we focus on the more common O and non-peculiar B stars. But even for these stars, a wealth of complex physics is involved in line-driven winds, and it is not possible for us to address all the aspects of this subject in the limited scope of a PhD dissertation. In this work we will mostly concern ourselves with the larger scale properties of the hot-star winds within the framework of an improved CAK theory.

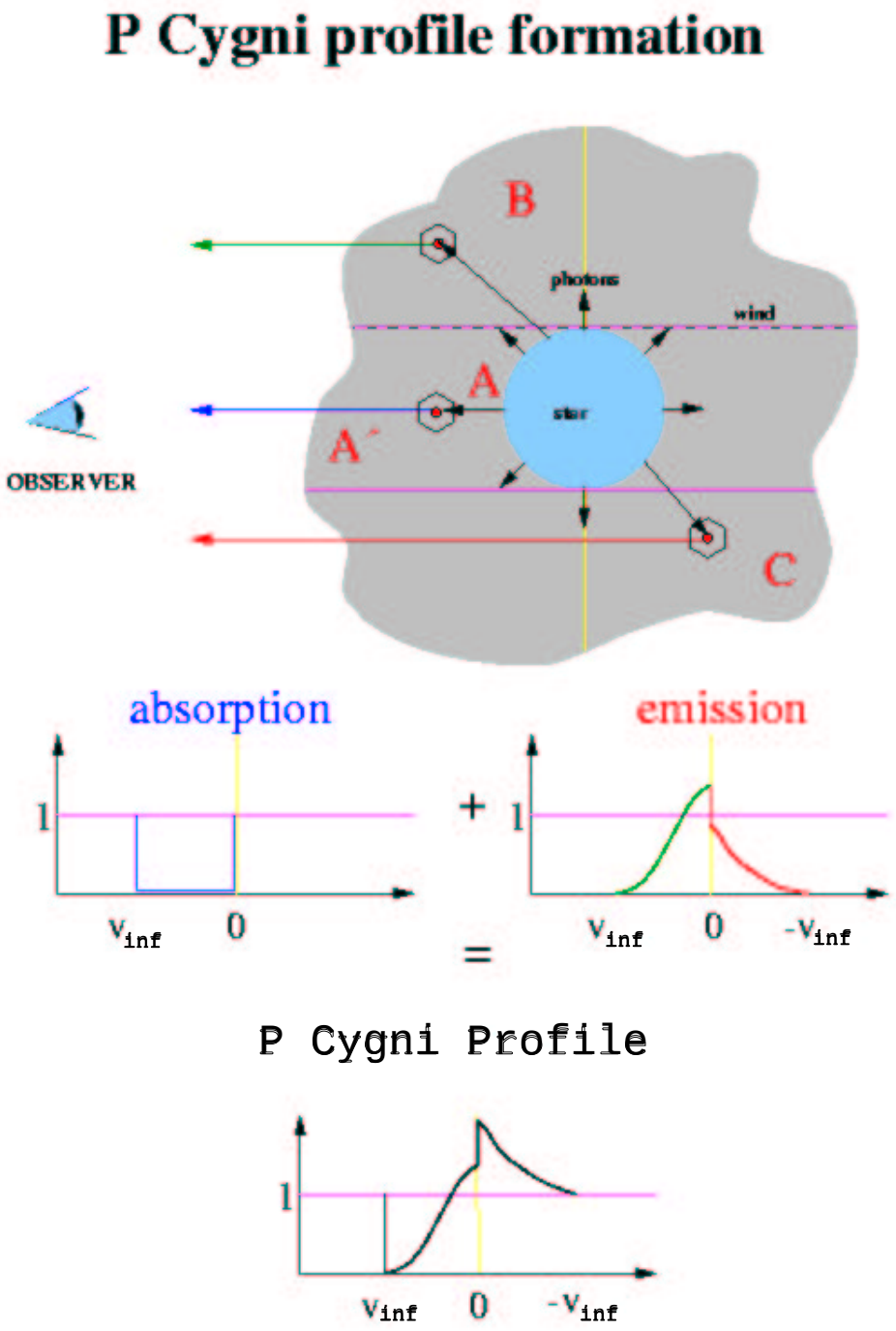

Figure 1.1: A sketch of formation of the P Cygni profile, adopted from J. Puls's website. Here v_{inf} is the terminal velocity of the wind.

1.3 Variability of Hot-Star Winds

Winds of OB-type stars are intrinsically variable. There is extensive evidence that these winds are not the steady, smooth outflows as it was classically assumed in the original CAK-type models, but instead manifest extensive structure and variability on both temporal and spatial scales. There are different physical mechanisms that can lead to such structures and variability, and it is convenient to classify them into two different categories: (1) *small-scale*, stochastic structure and (2) *large-scale* structure.

Small-scale variability is evidenced often by constant soft X-ray emission (Long & White 1980). UV lines with extended black troughs provide us with yet another indirect evidence. This suggests a nonmonotonic velocity field (Lucy & White 1980). Both of these can be caused by the strong intrinsic instability of the line-driving mechanism (Owocki 1994; Feldmeier 1995). On the other hand, large-scale changes seem to be the consequence of wind perturbation by processes occurring in the underlying star as evidenced by UV line profile variability. This can be attributed to several reasons: (i) dynamical effects of rotation, (ii) magnetic fields and (iii) non-radial pulsations.

Numerical analyses of small-scale structures require an extremely fine mesh, with grid size smaller than the so called 'Sobolev length' (to be discussed later). As such they are computationally expensive. They also involve more subtle physics that goes beyond the classical CAK treatment of the line-force, which we do not consider here. Our main goal is to provide a framework for better understanding some aspects of the large-scale structures. In particular, we examine the stellar rotation and the stellar global magnetic fields as possible mechanisms for the large-scale variability as evidenced by numerous observations.

1.4 Rotation of Hot Stars

The rotation of stars became detectable once the Doppler effect was understood. The wavelength of photons coming from the approaching side of the star is blue-shifted while the photons from the receding part become red-shifted. But because Doppler broadening is affected only by the projected component of the equatorial rotation speed, V_{rot} in the line of sight, we can measure, at the best, $V_{rot} \sin i$, where i is the inclination angle between the axis of rotation and the line of sight. OB-type stars are observed to have projected rotational speeds of 150 -250 km/s, but some of them rotate up to 400 km/s suggesting thus that hot stars are rapid rotators, in general. This is not surprising since hot stars are also young stellar objects, and as such they did not exist long enough to lose the initial angular momentum likely gained during the star formation from the original gas cloud.

Some hot stars rotate so rapidly that their rotation speeds are a significant fraction of the 'critical' value, which occurs when the apparent centrifugal force balances gravity, and any small outward force can launch material into orbit. These extreme rotational velocities deform the shape of a spherical star into an oblate configuration. In numerical computations, such an oblate star can be very difficult to model, especially if an effect known as *gravity darkening* (von Zeipel 1924) is considered. In the context of hydrodynamics, Cranmer (PhD Thesis, 1996) examined the effect of rotation that includes both gravity and *limb darkening*. In this work, we do not consider such extreme rotational velocities so that the approximation of a spherical star is well justified. Also, as an initial study, we ignore both gravity and limb darkening.

1.5 Magnetic Fields in Hot Stars

Magnetic fields among main sequence cool stars like the sun are generated through the dynamo mechanism for which convection zones, which are induced by the increased opacity associated with recombination, typically of hydrogen, but in

principle also of helium, are necessary. Hot stars are too hot to have such convective zones and thus classically have been thought not to have magnetic fields. But we know that non-convective Bp stars have strong surface magnetic fields of the order of many kG (Shore 1990). In addition, Henrichs et al (2001) reported a direct detection of magnetic field in a non-chemically peculiar early type star, β Cep. Donati et al (2001) estimated the polar strength of magnetic field for β Cep at about 400 G. There are also preliminary reports (Donati 2001) of a ca. 1000 G dipole field in the O-star θ^1 Ori C.

The source of these magnetic fields is not well understood. It could simply be the fossil field, or generated at the core, and then diffused out (Cassinelli and MacGregor 2001) to the surface. Both convective zones and rotation are the essential ingredients of the dynamo mechanism. So, in principle hot stars with weak convective zones but high rotation rate could produce macroscopic magnetic fields. But whatever the source might be, it seems plausible that hot stars can have magnetic fields.

1.6 Hot-star X-ray Emission

First detections of soft ($\sim$ 1 keV) x-ray emissions from hot, luminous OB stars by the *Einstein* satellite came as a surprise. Cool stars like the sun have x-ray emitting hot coronae, but hot stars do not have them due to lack of convection zones, which may be responsible for mechanical heating of the coronae. As such, hot stars were not expected to emit x-rays. However, even before these detections, xray emission from a narrow stellar corona was postulated to explain the superionization seen in the UV spectra of OB stars (Cassinelli & Olson 1979). Such a coronal model was extended further by Waldron (1984).

The surrounding cool wind of a hot star attenuates the emission from the hot corona at the base of the wind significantly (Lamers et al. 1984). A more favored scenario has been that the x-ray is emitted from wind shocks formed farther out

in the wind, which can arise from strong intrinsic instabilities in the line-driving mechanism (Lucy & Solomon 1970; Owocki & Rybicki 1984, 1985). Dynamical simulations of the evolution of this instability show that the x-ray emission from the resultant shocks are soft and low compared to observations (Owocki, Castor & Rybicki 1988; Feldmeier 1997). There is mounting evidence that the hard x-rays observed in some of the OB stars (e.g. τ Sco & θ^1 Ori C) require strong shocks with velocity jumps of order $\Delta V \sim v_\infty/2$. The standard instability induced wind-shocks cannot explain such hard x-ray; instead magnetically channeled wind shock models are invoked (Babel & Montmerle 1997a, 1997b).

Discriminating between these two models, the coronal and the wind-shock models, was difficult with low-resolution x-ray spectroscopy. But the recently launched x-ray satellites, *Chandra* and *XMM*, provide us with high-resolution and high signal to noise line profiles and line ratios that can help determine the velocity structures, density and spatial location of the x-ray emission. In particular, the He-like forbidden-to-intercombination (f/i) line strength ratio can potentially yield the radius of the x-ray emitting plasma (Waldron and Cassinelli 2001; Cohen et al. 2002). Traditionally, f/i ratio has been used as a density diagnostics in coronal sources. But in hot stars the presence of intense UV radiation can weaken the forbidden line altering the f/i ratio. As such, care must be taken when applying f/i ratio to diagnose densities in hot stars which in general yields very high values (Gabriel and Jordan 1969).

Recent high resolution *Chandra* x-ray spectra of OB stars are providing important clues about the mechanisms which produce x-rays from these young stars. For ζ Pup, the broad, blue-shifted line profiles, line ratios, and derived temperature distribution suggest that the x-rays are produced throughout the wind, perhaps via instability-driven wind shocks (Cassinelli et al. 2001). However, in τ Scorpii's *Chandra* HETGS spectrum, the hard, strong but narrow x-ray emission spectrum

suggests that x-ray emitting plasma is located near the stellar surface (Cohen et al. 2002, Cohen, Cassinelli & Waldron 1997), favoring magnetically channeled wind shock model. Similar mechanism is suggested for the very young O star θ^1 Ori C (Gagne et al. 1997). On the other hand, the very broad ($\Delta V \sim 1000$ km/s) and symmetric x-ray spectra observed for δ Ori and ζ Ori are difficult to explain (Miller et al. 2000; Waldron and Cassinelli 2001).

1.7 Overview of Research

Optical pictures of the sun during the eclipse or X-ray images of the sun provide us with a vivid example of how magnetic fields can influence the solar wind. The magnetic fields confine the gas within closed loops, while in the coronal hole region the gas is able to flow out with high-speeds. There is no simple way of studying this competition between the field and the wind, since this is usually a time-dependent problem. In this work we wish to investigate such an interaction between the wind and the fields for the case of hot stars.

The theory of the line-driven winds is highly non-linear, and inclusion of magnetic fields makes it even more complex. Thus analytical solutions are not easily available for most problems in the theory of hot-star winds. In the past, there have been some limited attempts to study the effects of surface magnetic fields on the line-driven winds. Notably, Shore and Brown (1990) proposed a model of a magnetically confined circumstellar matter in helium strong B stars. Babel and Montmerle (1997a) extended this by modeling the stellar wind within the framework of a *prescribed* magnetic field geometry limited to the region where the magnetic fields were strong enough to contain the wind. This is often cited in literature as the 'magnetically confined wind shock' (MCWS) model and used to explain hard x-ray emission from some of the hot stars, e.g. θ^1 Ori C. In this thesis we attempt to incorporate the full MHD equations *self-consistently* to study how magnetic fields affect the line-driven winds within and outside the magnetically confined region.

In chapter 3 we present numerical simulations of the effect of stellar dipole magnetic fields on such winds, using the publicly available numerical solver ZEUS-3D as a tool. We show that the overall degree to which the wind is influenced by the field depends largely on a single, dimensionless 'wind magnetic confinement parameter'. We conclude from the simulations that for weak confinement the field lines are ripped open into a radial configuration, but nonetheless some wind material is diverted towards the equator, enhancing the density and reducing the flow speed in the equatorial region. For strong confinement, the magnetic field remains closed over a limited range of latitude and height about the equatorial surface, but eventually is opened into a nearly radial configuration. The flow pattern within the closed loops is complex, and may involve some material falling back onto the stellar surface. Although we assume an isothermal gas, we estimate the amount of hard X-ray that can be produced within closed loops and open field flow where the equatorial channeling leads to oblique shocks.

Following this, in chapter 4, we discuss the polar flow that is characterized by a faster-than-radial expansion more gradual than anticipated by earlier 1D flow-tube studies. We show that relatively modest increase in terminal speed is consistent with observational constraints.

There is a longstanding problem in astrophysics in understanding the formation of transient disks in Be stars. It is difficult to understand how such a structure wherein the material is in a Keplerian orbit can be formed in a hot-star especially because while the line-force is an efficient mechanism to lift material off the stellar surface, it is not efficient in providing angular momentum necessary for the material to go into a Keplerian orbit. Bjorkman & Cassinelli (1993) proposed a Wind Compressed Disk (WCD) model wherein conservation of angular momentum tends to focus the wind material into a density enhanced disk-like equatorial region. However, dynamical simulations of Owocki et. al. (1994) showed that the material from

the rotating star lacks the necessary angular momentum to form a stable Keplerian orbit that would define a disk. Instead, the material flows through the WCD, with the inner portion falling back onto the star while the outer portion flows out as an equatorial outflow. This scenario is contrary to the observed dense, nearly stationary Keplerian disks (Hanuschik 1996; Hummel 1998; Rivinius et al. 2001). One obvious candidate for providing angular momentum is the moment arm of a stellar magnetic field. In chapter 5 we present numerical MHD simulations where starting from an initial condition at which a dipole field is imposed on an existing 1D spherically symmetric wind of a rigidly rotating star, then the model is evolved forward in time to an asymptotic solution. We show that although the magnetic field can indeed provide angular momentum to the wind, it does not form a Keplerian disk. Instead, for sufficiently strong magnetic confinement density enhanced equatorial outflow often accompanied by high density centrifugally-driven mass ejecta are formed.

One important issue we want to address in this thesis is whether our dynamical MHD models can help explain the detection of sometimes quite hard, and even cyclically variable x-ray emission from hot stars. The isothermal MHD models in chapter 3 do not include the detailed energy balance treatment necessary for quantitative modelling of shocked-gas x-ray emission. In chapter 6, we present adiabatic MHD models that do include energy balance equation, although, as our first attempt, we do not include any radiative cooling term. We show that the models with the magnetic confinement $\eta_* \geq 1$ are dramatically different from their isothermal counterparts with identical wind and stellar parameters.

Finally, we conclude the thesis with a brief summary and the plans for future work in chapter 7.

Chapter 2

THE THEORY OF STELLAR WINDS

The theory of line-driven winds is a complex subject. It involves a set of highly non-linear equations which are not usually solvable analytically. In particular, if the magnetic fields are involved in channeling such winds, the resultant system of equations is extremely difficult to analyze. We will use numerical simulations as an aid for our study of the magnetized hot-star winds. Our focus is to sort out the physics behind such complex winds.

Before we describe the theory of the line-driven winds in §2.5, let us briefly discuss much simpler gas-pressure-driven stellar wind, like the solar wind in §2.1. We introduce the general equations governing astrophysical fluids that are subject to the magnetic forces in section §2.2. We discuss Weber and Davis (1967) model of the solar wind in §2.3 followed by the Pneuman and Kopp (1971) model in §2.4.

2.1 Gas Pressure Driven Isothermal Winds: the Solar Wind

2.1.1 The Expansion of the Solar Corona

The first model of a solar corona that extends beyond the earth's orbit was proposed by Chapman (1957), who assumed a static atmosphere where the energy is transferred by thermal conduction alone. For a steady state, the heat flux across any Gaussian surface is constant, and if we assume spherical symmetry, then:

$$4\pi r^2 \kappa \frac{dT}{dr} = C \tag{2.1}$$

where C is a constant, r is the radius and $\kappa\, dT/dr$ is the the heat flux density with the thermal conduction $\kappa = \kappa_0 T^{5/2}$ (Spitzer 1956). The above equation can be readily integrated to yield:

$$T = T_0 \left(\frac{R_0}{r}\right)^{2/7} \tag{2.2}$$

under the assumption that $T = T_0$ at $r = R_0$ and temperature T goes to zero at large radii. Moreover, this corona is subject to the hydrostatic equilibrium condition,

$$\frac{1}{\rho}\frac{dP}{dr} = \frac{GM_\odot}{r^2}\,. \tag{2.3}$$

Using the ideal gas law, the pressure can be written as $P = \rho\, a^2$ where $a^2 = a_0^2\,(R_0/r)^{2/7}$ with the isothermal sound speed a_0 at the base of the corona. The hydrostatic equation can be now integrated,

$$P = P_0 \exp\left[\frac{7R_0}{5H_0}\,\left[\left(\frac{R_0}{r}\right)^{5/7} - 1\right]\right] \tag{2.4}$$

where P_0 is the pressure at the coronal base $r = R_0$, $H_0 = a_0^2 R_0^2/GM_\odot$ is the scale height. Clearly, as $r \to \infty$ the pressure approaches a finite value,

$$P(\infty) = P_0 \exp\left[-\frac{7R_0}{5H_0}\right]. \tag{2.5}$$

Here,

$$\begin{aligned} \frac{R_0}{H_0} &= R_0\,\frac{GM_\odot}{a_0^2 R_0^2} \\ &\approx \frac{14}{(T_0/10^6\,K)} \end{aligned} \tag{2.6}$$

for R_0 close to the solar surface. This leads to,

$$\log\left(\frac{P_0}{P_\infty}\right) \approx \frac{8.5}{(T_0/10^6)}\,. \tag{2.7}$$

In practice P_∞ is the pressure of the interstellar medium (ISM) that surrounds the heliosphere, and we observe this ratio $\log\,(P_0/P_{ISM}) \approx 12$. So, if we wish to have a

hydrostatic corona that is contained by the gas pressure of the ISM, the temperature of the corona must be,

$$T_0 < 0.7\,10^6 K\,. \tag{2.8}$$

But the observations show that the temperature of the solar corona is a few million degrees K. Clearly, P_∞ obtained from this model cannot be matched by the interstellar medium pressure. In addition to this shortcoming, in the limit of $r \to \infty$ the temperature approaches zero, and since the pressure is finite at large radii, the density becomes arbitrarily large. Because of these inconsistencies, the solar corona cannot remain static.

2.1.2 Parker's Solution to the Solar Wind

Parker (1958) resolved the above problem by suggesting that solar the corona is continuously expanding outwards simply because there is no 'lid' that can contain the corona. He called this outflow as the 'solar wind'.

Parker considered a spherically symmetric solar wind that is in a steady, time independent motion where all the properties vary with distance r only. Then the equation of conservation of momentum for a fluid parcel becomes:

$$v\frac{dv}{dr} = -\frac{1}{\rho}\,\frac{dP}{dr} - \frac{GM_\odot}{r^2}\,, \tag{2.9}$$

where $M_\odot$ is the mass of the sun. The equation of mass conservation is:

$$\frac{1}{r^2}\,\frac{d}{dr}\left(r^2\rho v\right) = 0\,. \tag{2.10}$$

If we assume the mass loss rate $\dot{M}$ is a constant, then

$$\dot{M} = 4\pi r^2 \rho(r) v(r)\,. \tag{2.11}$$

In principle, as the gas expands it will cool, and unlike the hot-star winds where intense radiation from the star keeps the wind nearly isothermal, the solar wind may not remain at constant temperature. But the hot solar coronal material has a very

high conductivity due to the mobile electrons, implying thus a small temperature gradient. As such, for simplicity it is assumed that the solar wind behaves like a perfect gas maintained at a constant temperature T, which is of the order of a few MK as mentioned above. Using the perfect gas law and the equation (2.11), we can now replace the pressure gradient term in the continuity equation (2.9) to obtain,

$$\begin{aligned} \frac{1}{\rho}\frac{dP}{dr} &= a^2\frac{1}{\rho}\frac{d\rho}{dr} \\ &= -\frac{a^2}{v}\frac{dv}{dr} - \frac{2a^2}{r}\,. \end{aligned} \tag{2.12}$$

Substituting this in the equation (2.9) yields:

$$\left[v^2 - a^2\right]\frac{1}{v}\frac{dv}{dr} = \frac{2a^2}{r} - \frac{GM_\odot}{r^2}\,. \tag{2.13}$$

When the right hand side (RHS) is zero then we obtain the critical solution at $r = r_c$, with

$$r_c = \frac{GM_\odot}{2a^2}\,. \tag{2.14}$$

This defines the 'critical radius' and can be obtained either when

$$v(r_c) = a \tag{2.15}$$

or

$$\frac{1}{v}\frac{dv}{dr}(r = r_c) = 0\,. \tag{2.16}$$

We are interested in continuous and single-valued solutions of $v(r)$ and dv/dr. If the condition (2.15) is satisfied then dv/dr has the same sign for all r or else (by mean value theorem) there would have been a radius r_c where dv/dr would attain zero. This implies that $v(r)$ is either monotonically increasing or monotonically decreasing function of radius. On the other hand, if the condition (2.16) is met, $(v^2 - a^2)$ has the same sign for all r, implying that at radius $r = r_c$ the speed $v(r_c)$ attains a maximum or a minimum.

The solution topology to this isothermal solar wind problem is sketched in figure 2.1. Each of the solution types fits a different set of boundary conditions. Mathematically, all these solutions are acceptable, but physically not all of them are plausible. For instance, the solution types 3 and 4 can be ruled out as acceptable on the basis of the fact that they all start off at the base of the corona at supersonic speeds. We have no physical or observational evidence to believe that the solar corona is expanding supersonically at the base. The remaining two types of solutions have small speeds at the base, but they differ at large radii. The wind in solution type 2 is supersonic at the outer radii, while in the solution type 1, often called "breeze" solution, the wind speed approaches zero asymptotically implying a finite pressure at $r = \infty$. But this finite pressure cannot be matched by the interstellar pressure. Thus the solutions of type 2 remain as the most plausible solutions.

To illustrate this point more clearly, let us first integrate the equation (2.13). The equation can be more easily integrated if we rewrite the momentum equation replacing the derivative term dv/dr by $(1/2v)(dv^2/dr)$:

$$\left[1 - \frac{a^2}{v^2}\right] \frac{1}{2} \frac{dv^2}{dr} = \frac{2a^2}{r} - \frac{GM_\odot}{r^2} \,. \tag{2.17}$$

This can be easily integrated to yield,

$$\frac{v^2}{2a^2} - \frac{1}{2} \ln \frac{v^2}{a^2} = 2 \ln \frac{r}{r_c} - \frac{GM_\odot}{a^2 r} + C \tag{2.18}$$

where C is a constant of integration. We can evaluate the above transcendental equation at $r = r_c$ where $v(r_c) = a$, and if we define $u \equiv v/a$ and $x \equiv r/r_c$ we obtain,

$$\frac{u^2}{2} - \ln u = 2 \ln x + \frac{2}{x} - \frac{3}{2} \,, \tag{2.19}$$

where the appropriate value for solution type 2, $C = 3/2$ was used. Now, for solutions type 1 as $r \to \infty$ the velocity u decreases to an arbitrarily small number, as such,

$$\ln u \approx 2 \ln x \tag{2.20}$$

implying

$$u \propto \frac{1}{r^2}\,. \tag{2.21}$$

Hence, the continuity equation (2.11) for a fixed mass flux implies a finite value of density ρ. This in consequence implies the finite pressure at large r.

On the other hand, for the solution type 2, the velocity u increases with radius, thus

$$u^2 \approx 4 \ln x\,. \tag{2.22}$$

In this case,

$$u \propto \sqrt{\ln x}\,. \tag{2.23}$$

This implies that the density at large distances goes to zero. Thus, the pressure goes to zero as well. Therefore, the solutions of type 2, match boundary conditions at the base of the corona and at large radii. Note that the solutions are independent of density.

2.1.3 Numerical Solution

In this section we reproduce the above isothermal solar wind solution for various base coronal temperatures using ZEUS-3D. The code is very versatile and allows the user to specify a variety of flow geometries (planar, cylindrical and spherical) in one, two or three dimensions. In all our simulations in this work we use spherical polar coordinates with radius r, co-latitude θ and azimuth ϕ. In defining this particular problem of the isothermal solar wind we use, naturally, spherical polar coordinates in one dimension. We switched on all the necessary *hydrodynamic* modules and switched off the full energy equation in favor of the isothermal equation of state.

The boundary conditions are very important in reaching a stable numerical solution to set of partial differential equations we deal with here. Thus we took particular care in defining our inner, r_{min} boundary. We specify the density ρ_{in}

at the base but allow the inflow velocity v_{in} to 'float' by extrapolating it linearly from the closest two zones in the interior of the computational domain. In order to make our solution independent of the initial conditions, we do not allow any supersonic outflow or inflow in the inner boundary by simply limiting the velocity v_{in} below the sound speed, $|v_{in}| \leq a$. We also specify the temperature of the wind to a fixed value T_0. The upper boundary, r_{max} which occurs at the maximum radius of our computational domain, meets the simple outflow condition where all the hydrodynamic quantities are linearly extrapolated.

Figure 2.2 shows the wind velocity $v(r)$ obtained by the numerical simulations for various temperatures of the solar corona as noted on the figure. All these solutions are in a very good agreement, within a fraction of percent, with the semi-analytical solution of the solar wind obtained by solving the transcendental equation 2.19. The observed solar wind speed at 1 AU is ca. 400-700 km/s which can be matched by our simulations with assumed solar corona temperatures of 2-4 MK. In reality, the solar wind is not isothermal, the temperature of the gas drops to about 100,000 K near the earth. These solutions show that even a simple approximation can yield fairly good results.

2.2 Magneto-hydrodynamic Equations

The hot-star winds we deal with in this work, are mainly composed of fully ionized hydrogen and helium, and trace amounts of partially ionized metals ($\sim 10^{-4}$). These winds are dense enough that the mean free paths between collisions are relatively small, and the plasma can be treated as a single fluid. The time-dependent MHD equations governing the system include the conservation of mass,

$$\frac{D\rho}{Dt} + \rho \nabla \cdot \mathbf{v} = 0, \tag{2.24}$$

and the equation of motion

$$\rho \frac{D\mathbf{v}}{Dt} = -\nabla p + \frac{1}{4\pi}(\nabla \times \mathbf{B}) \times \mathbf{B} - \frac{GM\hat{\mathbf{r}}}{r^2} + \mathbf{g}_{external}\,, \tag{2.25}$$

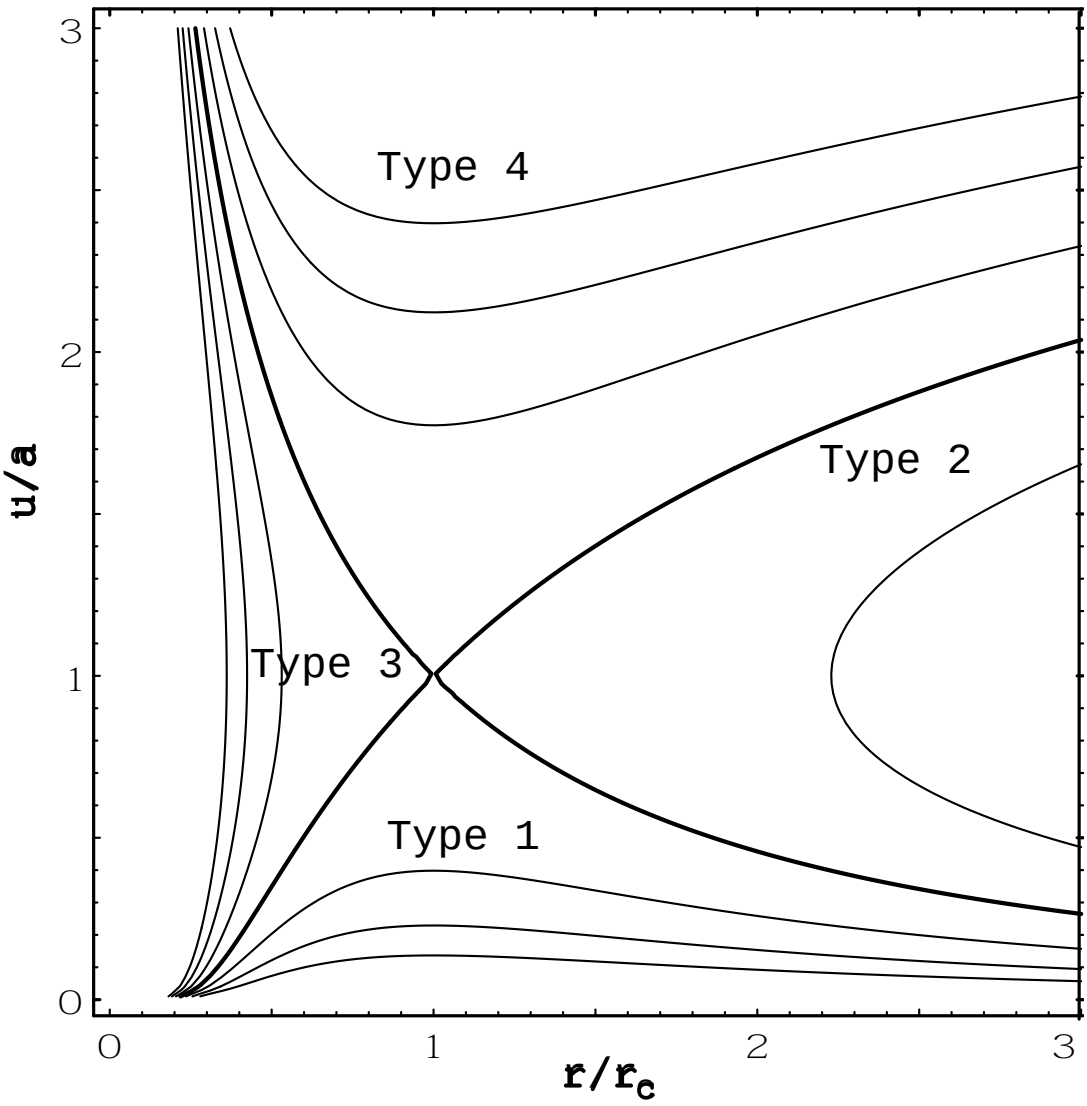

Figure 2.1: The solution topology for the isothermal solar wind equations. The Y-axis u/a represents velocity in the unit of sound speed, and the X-axis is the radius in the units of critical radius, r_c. Types 3 and 4 solutions are supersonic at the base of the corona, and thus are physically inadmissible. Type 1 represents the 'breeze' solutions that never reaches supersonic values, contrary to observations. The solution type 2 (bold line) is in agreement with observations.

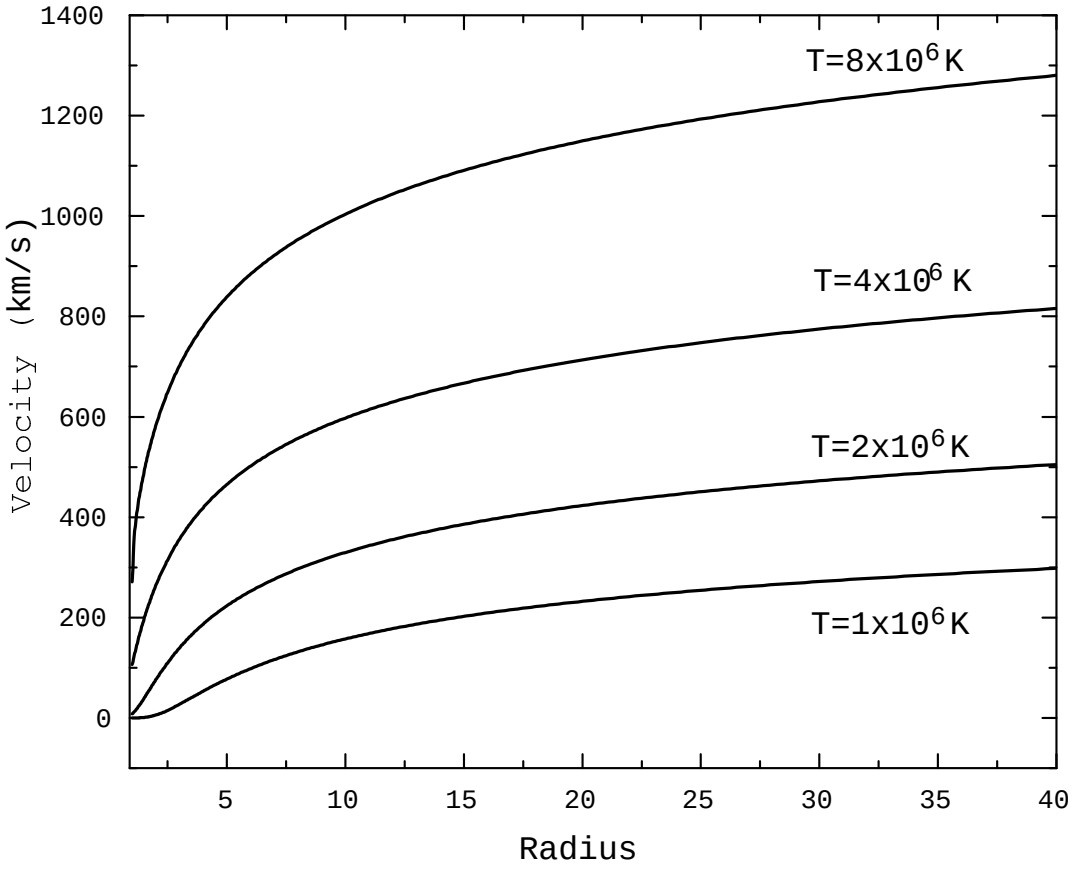

Figure 2.2: Velocity of the isothermal solar wind obtained numerically plotted against the radius for the assumed coronal temperatures T=1, 2, 4 and 8 MK. The agreement with the analytical solutions is very good, within a fraction of a percent.

where ρ, p, and $\mathbf{v}$ are the mass density, gas pressure, and velocity of the fluid flow, and $D/Dt = \partial/\partial t + \mathbf{v}\cdot\nabla$ is the advective time derivative. The gravitational constant G and stellar mass M set the radially directed ($\hat{\mathbf{r}}$) gravitational acceleration. The term $\mathbf{g}_{external}$ represents the total external force that may include the centrifugal force. In our case it is the line-force and the force due to scattering of the stellar luminosity L by the free electron opacity κ_e. The magnetic field $\mathbf{B}$ is constrained to be divergence free

$$\nabla \cdot \mathbf{B} = 0, \tag{2.26}$$

and, under our assumption of an idealized MHD flow with infinite conductivity (e.g. Priest & Hood 1991), its inductive generation is described by

$$\frac{\partial \mathbf{B}}{\partial t} = \nabla \times (\mathbf{v} \times \mathbf{B}). \tag{2.27}$$

The validity of such an assumption can be readily seen from the following. For a fluid at rest, the diffusion equation for the magnetic field can be written as,

$$\frac{\partial \mathbf{B}}{\partial t} = \frac{c^2}{4\pi\sigma}\nabla^2\mathbf{B}\,, \tag{2.28}$$

where σ is the conductivity for the fluid. This implies that an initial magnetic field will decay away in a diffusion time scale (Jackson 1967),

$$\tau_{diff} = \frac{4\pi\sigma L^2}{c^2}\,, \tag{2.29}$$

where L is a characteristic length of the spatial variation of $\mathbf{B}$. For ordinary metals, e.g. a copper sphere of 1 cm radius, the time τ_{diff} is of order 1 sec, but for astrophysical fluids (stellar winds) we deal with here this can be of order of 10^{10} years! This implies that the diffusion of the magnetic fields in stellar winds is unimportant and the ideal MHD approximation is valid.

A useful dimensionless parameter to characterize the relative importance of magnetic diffusion is the *magnetic Reynolds* number R_M defined as,

$$R_M = \frac{V\,\tau_{diff}}{L}\,, \tag{2.30}$$

where V is a typical advective flow velocity and with some macroscopic length scale L. For values of $R_M \lesssim 1$, the diffusion of field lines dominates over advective transport. But for stellar winds, where $V \sim 2000$ km/s and $L \sim 10^{12}$ cm, $R_M \sim 10^{13} \gg 1$. As such, resistive diffusion is irrelevant and the field lines are effective frozen in. Such a case is assumed in all the models we present in this dissertation. However, as in any finite difference method, effective diffusion by the numerical grid will allow reconnection of field at the grid scale. For our simulations with ca. 100 grid points in each dimension, this is typically on the order of effective numerical Reynolds number of order 100, much smaller than idealized value.

The one last equation that we should, in principle, consider solving is an explicit equation for conservation of energy, e.g. a purely adiabatic energy equation,

$$\rho \frac{D}{Dt}\left(\frac{e}{\rho}\right) = -p\nabla \cdot v\,. \tag{2.31}$$

But the stellar winds we consider in this work are relatively dense and the energy balance is primarily dominated by radiative processes that are rapid enough to keep the wind at nearly constant temperature. In all our simulations, except for the models in chapter 6, we will assume an explicitly isothermal flow with $T = T_{eff}$, where T_{eff} is the effective stellar temperature. In such a case, the sound speed $a = \sqrt{kT/\mu}$ with k Boltzmann's constant and μ the mean atomic weight of the gas is a constant. We use the perfect gas law to compute the pressure:

$$p = \rho a^2\,. \tag{2.32}$$

2.2.1 Numerical Solver: ZEUS-3D

Astrophysical processes that require simultaneous solution of all the above MHD equations, can be readily modeled using time-dependent numerical MHD codes, such as the Versatile Advection Code developed by Keppens and Goedbloed (1999), or the publicly available the ZEUS-3D code (Stone and Norman 1992). We chose to apply the latter for our research purposes.

ZEUS-3D is designed to solve astrophysical problems in 1-, 2- and 3-dimensions. It has a modular form which allows the user to select the appropriate parts of the code necessary for any specific problem. It also enables introduction of new physics through incorporation of additional subroutines. For instance, if we wish to study a spherically symmetric isothermal solar wind, the user is able to use spherical polar coordinates in 1-D, r dimension, shut off all the parts of the code that involves the magnetic fields and select an isothermal equation of state. But in order for us to study the line-driven winds, we had to include our own subroutines to account for the the radiative driving terms, and to specify the specialized boundary conditions. This kind of flexibility makes ZEUS-3D computationally efficient.

An important aspect of any numerical code is the interpolation scheme. ZEUS-3D implements three different schemes, the first order donor cell method, the second order van Leer method (van Leer 1977), and the third order piecewise parabolic advection (PPA) method introduced by Collela and Woodward (1984). In all our simulations, we use the second order van Leer method.

The van Leer method uses a piecewise linear function to represent the distribution of a zone centered scalar q within a zone. In this scheme, the face centered upwinded interpolated value q_i^* are,

$$q_i^* = \begin{cases} q_{i-1} + (\Delta x_{i-1} - v_i \Delta t)(dq_{i-1}/2) & \text{if } v_i < 0 \\ q_i - (\Delta x_i + v_i \Delta t)(dq_i/2) & \text{if } v_i > 0 \end{cases}$$

where v_i is the flow speed and dq_i are the monotonized van Leer slopes given by the following:

$$dq_i = \begin{cases} \dfrac{2(\Delta q_{i-1/2} \Delta q_{i+1/2})}{\Delta q_{i-1/2} + \Delta q_{i+1/2}} & \text{if } \Delta q_{i-1/2} \Delta q_{i+1/2} > 0 \\ 0 & \text{otherwise} \end{cases}$$

Here $\Delta q_{i+1/2} = (q_{i+1} - q_i)/\Delta x_i$. ZEUS-3D allows to have non-uniform grids, and the above definitions take this into account. For other aspects of the numerical

algorithms implemented in ZEUS-3D we refer the reader to Stone and Norman (1992).

2.3 Weber and Davis Model of Solar Wind

Let us next examine the more complex solar wind problem by including surface magnetic field and the rotation of the sun. The hot solar wind that we discussed above is expected to have an extremely high electrical conductivity implying that the surface magnetic field of the sun would be "frozen-in" and carried away by the plasma into the interplanetary space. If we ignored the rotation of the sun and assumed that the solar magnetic field is too weak to have any significant influence on the flow so that the coronal expansion is purely radial, then the resultant magnetic configuration would have been quite simple: field lines stretched out outward into a radial configuration.

But the sun rotates (although differentially) at the rate of about once in 27 days. The question is: how does the rotation change the magnetic field configuration under the same assumption of purely radial outflow? For simplicity let us consider the wind at the equatorial plane only, where $\theta = 90^o$. In a spherical polar coordinate system that is rotating with the sun, the velocity components of the solar wind can be written as follows:

$$\begin{aligned} U_r &= u \\ U_\phi &= -\omega r \sin\theta \\ U_\theta &= 0 \end{aligned} \tag{2.33}$$

with ω the angular velocity of the rotating sun, u the flow velocity that is constant at large radii from the sun. Because in the rotating frame of reference the source area remains fixed, the fluid parcel will follow the flow streamlines. The following is

the differential equation that governs such streamlines for a constant θ (Hundhausen 1972):

$$\frac{1}{r}\frac{dr}{d\phi} = \frac{U_r}{U_\phi} = \frac{u}{-\omega r \sin\theta} \,. \tag{2.34}$$

In our assumed 'frozen-in' field lines or equivalently ideal MHD approximation, these streamlines are also the field lines. Let us assume that the flow speed is constant, $u = u_s$. Then, the integration of the above equation yields:

$$r - R_\odot = \frac{-u_s}{\omega \sin\theta}(\phi - \phi_0) \tag{2.35}$$

where ϕ_0 is the initial position at $R_\odot$ which for simplicity can be assumed to be zero. From the condition for the divergence free magnetic fields, $\nabla \cdot \mathbf{B} = 0$ we can obtain the components of the fields:

$$\begin{aligned} B_r(r,\phi,\theta) &= B_*(R_\odot, 0, \theta)\Big(\frac{R_\odot}{r}\Big)^2 \\ B_\phi(r,\phi,\theta) &= -B_*(R_\odot, 0, \theta)\,\frac{\omega R_\odot}{u_s}\,\frac{R_\odot}{r}\,sin\theta \\ B_\theta &= 0\,. \end{aligned} \tag{2.36}$$

For a fixed colatitude θ, the magnetic field lines are wrapped into spirals by the solar rotation. In particular, for $\theta = 90^o$ we get a pattern of the magnetic field configuration similar to found by Weber and Davis (1967; WD thereafter) where they proposed a model of the solar wind in the equatorial plane in the presence of a monopole like magnetic fields.

The model of WD was somehow more complex than the picture we depicted above. In their more realistic model, WD assumed a polytropic gas with adiabatic index $\gamma = 1.22$ where the flow is influenced by the the fields as well. Based on the hydrodynamic and magnetic values of the solar wind near the Earth, they integrated the necessary MHD equations to find that the field lines naturally are drawn into spirals by solar rotation.

Here we do not wish to reproduce the exact WD model, but instead we want to show that even under the simplified assumption of an isothermal solar wind

with monopole-like magnetic fields at the solar surface and modest rotation, the numerical code ZEUS can basically reproduce self-consistently the essence of the WD model. The ZEUS code has been extensively tested for its accuracy (Stone and Norman 1992; Stone et al 1992) over the long period of time it has been public. In particular, Stone in his PhD dissertation(1990) tested for the correctness of the ZEUS code against the actual WD model.

2.3.1 Our Numerical Result

In this section, we present numerical results of our simplified version of WD models of the solar wind. The principle difference comes in the equation of state of the gas, where we adopt an isothermal gas with a fixed temperature, T. Like WD we limit ourselves to the equatorial plane of the sun with monopole like magnetic fields at the surface. We assume the rotation period of about 27 days at the equator resulting in the azimuthal speed $v_\phi \sim 1$ km/s. Although we assume azimuthal symmetry, the azimuthal velocity component v_ϕ is allowed to vary in radius and the problem can be considered as '1.5-dimensional'.

Earlier when we discussed the isothermal solar wind, we had to worry about only the hydrodynamic quantities at the lower and upper boundaries. Here, we have to account for the magnetic quantities as well. Thus in our definition of the lower boundary the conditions on most of the hydrodynamic quantities remain unchanged while the magnetic flux is introduced into the computational domain through the fixed radial component of the field, B_r. The azimuthal component of the flow, v_ϕ is fixed as we assume a rigidly rotating sun, and the azimuthal component of the magnetic field B_ϕ is extrapolated linearly from the two closest zones in the computational domain.

We evolve our version of the WD model from an initial condition at $t = 0$ sec when monopole-like magnetic field is introduced into a previously relaxed, 1D isothermal gas-pressure-driven solar wind. Figure 2.3 shows various MHD quantities

(as noted in the figure) at time $t = 350$ ksec of a run with assumed monopole-like surface stellar magnetic field of strength $B_0 = 1$G, and the rotation rate of 1.0 km/s. The temperature of the gas was set to $T = 2$ MK.

As expected from the WD model, the azimuthal velocity v_ϕ increases for a short radial distance, representing co-rotation, and then falls off as $\sim 1/r$ preserving the angular momentum gained up to the co-rotation radius. The radial velocity v_r profile is very similar to the one obtained for the isothermal 1- D solar wind case with the coronal temperature $T = 2$ MK. In agreement with equation 2.36 above, the radial component of the magnetic field B_r scales as $1/r^2$ while the azimuthal component as $1/r$. The net result is that the field lines are wrapped around into a spiral pattern.

If we increase the strength of the surface magnetic field, we expect the co-rotation radius to move further out. Figure 2.4 shows the results of another simulation of WD model now with $B_0 = 4$ G. Again, we see clearly that the fluid co-rotates further out to a larger radius, but the radial velocity remains virtually unchanged. The scaling of the the magnetic field components is the same as in the previous figure. It is interesting to note that even a modest magnetic field can force the wind to co-rotate to a relatively large radius. We shall see that the main reason for this is the relatively weak solar wind, and for the case of much denser hot-star winds significantly higher fields are required for co-rotation of the wind.

2.4 Pneuman and Kopp Model of the Solar Wind

Before we study MHD aspects of hot-star winds, let us describe the solar analogy of our research in this work. Numerous pictures in the optical and soft-Xray bands show that the solar corona is highly structured and the magnetic fields play an important role in it. Near the sun where the magnetic field is strong, the coronal gas is contained within the closed loops. But because the strength of the

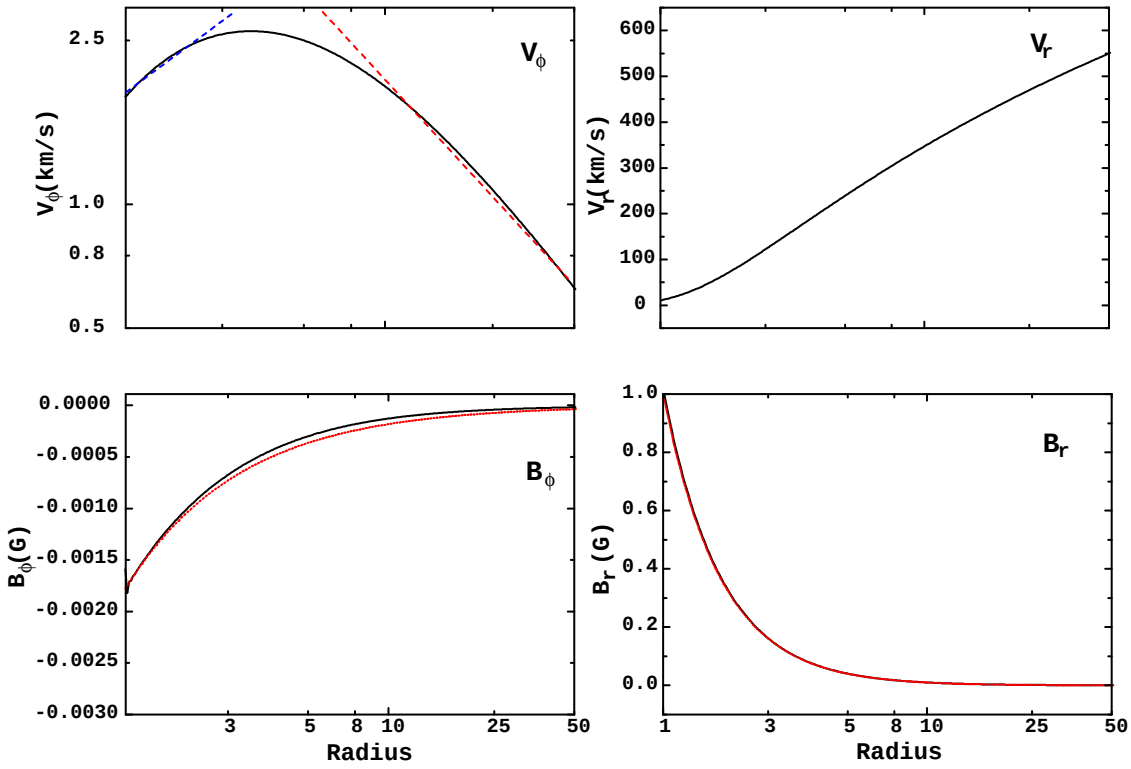

Figure 2.3: Sample solution of Weber and Davis model of the solar corona. Here the strength of the magnetic fields at the base, $B_0 = 1$ G. The rotation rate at the solar surface is about 1.0 km/s. The blue dashed line in the upper left panel represents co-rotation, the red line is the angular momentum preserving v_ϕ. The red line in the lower left panel is the $1/r$ fit for $B_\phi(r)$ while the red line in the lower right panel is the $1/r^2$ fit for $B_r(r)$. The aim here is to reproduce the results *qualitatively*. For *quantitative* analysis of this problem using the ZEUS code see Stone (PhD dissertation, 1990)

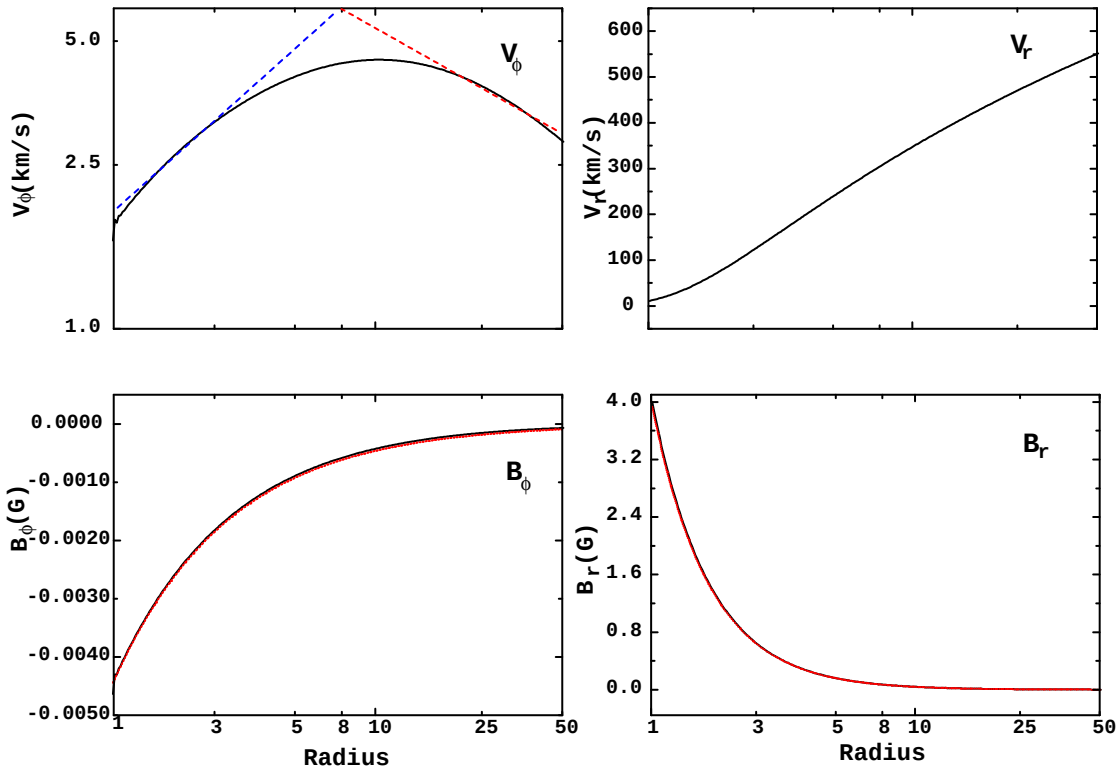

Figure 2.4: Another sample solution of modified Weber and Davis model of the solar corona. Here the strength of the magnetic fields at the base, $B_0 = 4$ G. The rotation rate at the solar surface is about 1.0 km/s. Note that the co-rotation radius here is significantly larger than in the case of $B_0 = 1$G

field decreases outward rapidly, the gas flow is able to dominate and stretch the field lines outward into a radial configuration.

Motivated by these, Pneuman and Kopp (1971, PK hereafter) proposed a model of a steady, axisymmetric, coronal expansion from the sun with the surface dipolar magnetic field and solved numerically the relevant MHD equations. The necessary equations for this model have already been introduced in §2.2 , equations 2.24 through 2.32 with no external force, $g_{external} = 0$.

They assumed constant density at the surface that is independent of the latitude with the coronal temperature $T = 1.56 \times 10^6$ K and prescribed the normal/radial component of the magnetic field at the coronal base to be that of a dipole, $B_r = B_0 \cos\theta$ with the polar magnetic field $B_0 = 1$ G. To solve this problem, PK used an iterative technique in three stages. First, they used Ampere's Law (eqn 2.27) to find the magnetic field generated by a given current density. Then, both the continuity and the equation of motion along magnetic field lines are solved to obtain the density and velocity everywhere in the computational domain. Finally, a new current distribution is computed from these. This process is repeated until the solution converges.

We, on the other hand, use the time-dependent MHD code ZEUS-3D to reproduce this model. We evolve our simulation from an initial condition a time $t = 0$, when a dipole magnetic field is inserted into a spherically symmetric isothermal solar wind that has been relaxed in an earlier separate 1D hydrodynamic simulation. We adopt all the MHD quantities like the strength of the magnetic field, the temperature and the density of the corona from the PK model. Like Pneuman and Kopp, we fix both the density and the radial component of the magnetic field at the lower boundary. We let the two components of the velocity and the latitudinal component of the magnetic field 'float' freely through simple linear extrapolation with constant gradient.

A time snapshot of density (logarithmic color-scale) and field lines (solid lines) at $t = 600$ ksec of our simulation is shown in right panel of figure 2.5. For convenience, a scanned figure of the original PK result is shown in the left panel. The dashed lines represent the initial dipolar field lines. Since we do not have the actual data of PK results, we were unable to make quantitative comparison, but the qualitative similarity between these two results obtained from two completely different techniques is quite good. The wind material is magnetically channeled towards the equator leading to a density enhancement in the equatorial region. The field lines at the higher latitudes are ripped open by the wind flow, but the magnetic field near the solar surface about the equator is strong enough to contain the wind. Within the closed loops, the gas is maintained in a hydrostatic equilibrium. This is possibly due to high sound speed of hot solar wind, and we shall see that this is quite different from the relatively cool winds of hot stars where the flow within the magnetically confined region is complex, with the wind supersonic from very near the stellar surface.

Many of our later results for line-driven winds are based on the solar analogy of this PK model. As we will see, there are some fundamental differences in the end results that are the consequence of the different physical nature of these winds.

2.5 Line-force in Stellar Winds

We showed in the first part of this chapter that the solar wind arises from pressure-expansion of the hot corona which is superheated to temperatures of a few million degrees by the mechanical energy dumped by the convection near the surface of the relatively cool sun. By contrast, the hot stars with surface temperatures 10,000-100,000 K are considered not to have convection zones, a necessary mechanism to have hot coronae. Their winds remain nearly at surface temperatures of the star. Thus they lack the very high-pressure needed to drive the wind against the

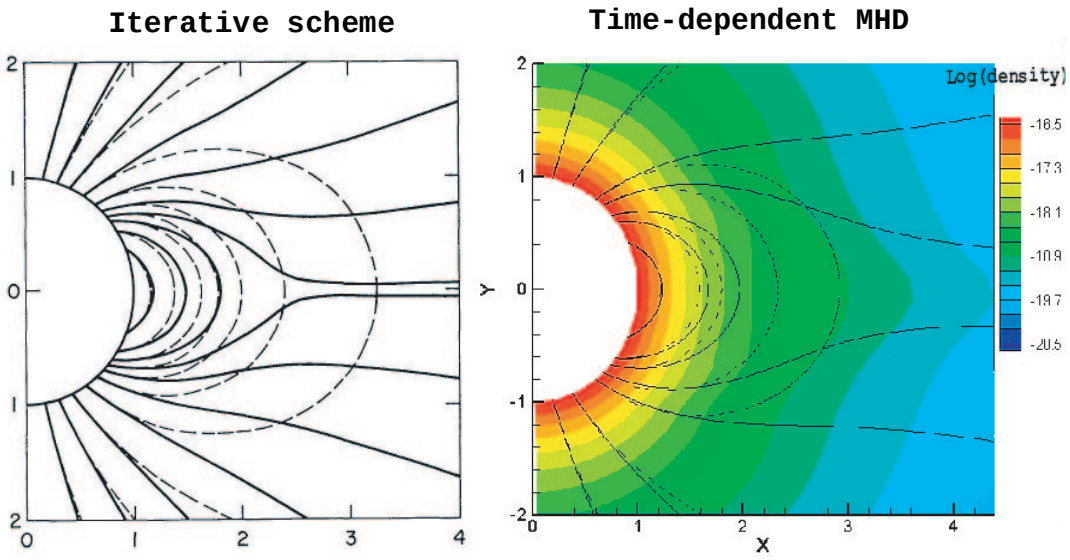

Figure 2.5: Left panel is the result of Pneuman and Kopp obtained by an iterative scheme. Right panel is our result that was obtained using time-dependent MHD code. Color scale represents logarithmic density scale, the solid lines are the magnetic field lines, the dashes lines are the initial dipolar field lines, just to show how much the field lines have evolved from the initial condition.

gravity in a similar fashion to the solar wind. But the hot stars are very luminous, and it is the pressure of radiation that drives their winds.

Intuitively light is not a good source for momentum transfer. This is mainly because the momentum of a photon is determined by division of its energy by the maximum possible speed, c, the speed of light. But the hot stars are no ordinary objects. They are very massive and very luminous. In their case, the photons become the dominating factor in controlling the physics of the continuous outflow of material from the stellar surface. The typical flow speeds of hot-star winds can reach as high as 3000 km/s, much faster than the 400-700 km/s speed of the solar wind. At the same time, typical mass loss rates for the hot stars can reach up to $\sim 10^{-6} M_{\odot}/yr$, which are up to a factor of a billion higher than that of the sun.

In this section we discuss the interesting question of how photons can drive hot-star winds. First, we present the theory of the line-driving, and then illustrate solutions with some numerical simulations.

2.5.1 Radiation Force for a Point-Source Star

The line force per unit mass (acceleration) due to radiation at a radius r, is given generally by:

$$\mathbf{g_{rad}} = \frac{1}{c} \oint \int_{\nu=0}^{\infty} \kappa_\nu I_\nu(r, \hat{n})\, \hat{\mathbf{n}}\, d\Omega\, d\nu \tag{2.37}$$

where the line strength has been characterized by isotropic κ_ν, the total mass extinction coefficient that includes both absorption and scattering. The monochromatic radiative intensity I_ν along the direction $\hat{n}$ is integrated over the solid angle Ω.

The total mass extinction coefficient can be separated into two parts:

$$\kappa_\nu = \kappa_e + \kappa_L \tag{2.38}$$

where κ_e is the mass absorption coefficient (sometimes called "opacity") due to scattering of continuum photons by free electrons, given by $\kappa_e = \sigma_e/\mu_e$. Here σ_e

$(= 0.66 \times 10^{-24} am^2)$ is the classical Thompson cross-section, and μ_e is the mean atomic mass per free electron defined as $\mu_e = 2m_H/(1+X)$, with m_H and X the mass and mass-fraction of hydrogen, and κ_L the absorption coefficient due to the bound electrons of a line. Thus the radiation force can be separated in two parts as well:

$$g_{rad} = g_e + g_L \,. \tag{2.39}$$

where g_e is the radiation force due scattering of continuum photons by free electrons and g_L is the line force.

2.5.2 Force due to Electron Scattering

The continuum processes in hot stars are presumed to be dominated by electron scattering. Now, we can write,

$$\mathbf{g_e} = \frac{\kappa_e}{c} \oint \int_{\nu=0}^{\infty} I_\nu(r, \hat{n})\, \hat{\mathbf{n}}\, d\Omega\, d\nu \,. \tag{2.40}$$

In the case of spherical symmetry and a point source star, the integrand gives just the total radiation flux. Thus,

$$g_e = \frac{\kappa_e}{c} \frac{L_*}{4\pi r^2} \tag{2.41}$$

where L_* is the total bolometric luminosity of the star. Here we assumed that the wind is optically thin to the continuum radiation.

Note that g_e is inversely proportional to r^2, just like the gravity. Therefore it is useful to compare g_e with gravity g by defining,

$$\Gamma \equiv \frac{g_e}{g} = \frac{\kappa_e L_*}{4\pi G M_* c} \tag{2.42}$$

where Γ is often referred as the Eddington parameter, G is the gravitational constant and M_* is the mass of the star. Clearly, if the value of Γ exceeds unity, the star cannot remain in hydrostatic equilibrium. For the OB-type stars we study here $\Gamma \approx 0.5$. Thus g_e essentially reduces the effective gravity by $1-\Gamma$, i.e. $g_{eff} = g(1-\Gamma)$.

2.5.3 Radiation Force due to a Single Line

In formulating the radiation force due to a single line, we will follow mostly Cranmer (PhD Thesis, 1996). In general,

$$\mathbf{g_L} = \frac{\kappa_L}{c} \oint \int_{\nu=0}^{\infty} \tilde{\phi}(\nu - \nu')\, I_\nu(r, \hat{n})\, \hat{\mathbf{n}}\, d\Omega\, d\nu, \tag{2.43}$$

where κ_L is the mass absorption coefficient for a single line, $\tilde{\phi}(\nu)$ is a normalized line profile function. Here ν' is the frequency of the line in the comoving frame of the gas, and can be related to the emitted frequency ν_0 by

$$\nu' = \nu_0 \left(1 + \frac{\hat{\mathbf{n}} \cdot \mathbf{v}(\mathbf{r})}{c}\right), \tag{2.44}$$

with $\mathbf{v}(\mathbf{r})$ the flow velocity, non-relativistic in the domain of our interest.

Now, for convenience, let us make a change of variables and define the frequency in the unit of Doppler widths,

$$x = \frac{\nu - \nu_0}{\Delta\nu_D} \tag{2.45}$$

where the Doppler width $\Delta\nu_D = \nu_0\, v_{th}/c$ with the ion thermal speed in the gas v_{th}. Thus the single line force can be rewritten as:

$$\mathbf{g_L} = \frac{\kappa_L \Delta\nu_D}{c} \oint \int_{x=-\infty}^{\infty} \phi\left(x - \frac{\hat{\mathbf{n}} \cdot \mathbf{v}(\mathbf{r})}{v_{th}}\right) I_\nu(r, \hat{n})\, \hat{\mathbf{n}}\, d\Omega\, dx\,. \tag{2.46}$$

Note that the lower limit for $x = -c/v_{th}$ has been extended to $x = -\infty$. We can do this because the line opacity is mostly concentrated around the line center and $-c/v_{th}$ is many Doppler widths away from it. The error introduced by this approximation is negligible, but it makes the further analysis much simpler.

The intensity $I_\nu(r, \hat{n})$, will, in general, have a contribution from the direct intensity from the core and a contribution from the diffuse component arising from the radiation scattered (or created) within the wind,

$$I_\nu = I_\nu^{dir} + I_\nu^{diff}\,. \tag{2.47}$$

In this work, the treatment of the line force is based on *pure absorption* model. In this model the force is computed by integration of the frequency-dependent attenuation of the direct radiation. The contribution to the line force from the diffuse radiation is ignored since in the smooth and supersonic wind we consider here, the line force arising from it is nearly fore-aft symmetric yielding net zero force. Now, the direct component of the intensity can be written as:

$$I_\nu^{dir}(r) = I_* e^{-\tau_\nu(r)} \tag{2.48}$$

where I_* is the core intensity, assumed to be constant throughout the stellar surface, and τ_ν is the frequency-dependent optical depth along a path of length s:

$$\tau_\nu(r) = \int_{R_*}^{r} \kappa\rho(r')\phi\left(x - \frac{\hat{\mathbf{n}}\cdot\mathbf{v}(\mathbf{r}')}{v_{th}}\right) dr' \,. \tag{2.49}$$

In general, the equation (2.48) involves *non-local* integration over space, but one can localize the radiation transport by invoking the *Sobolev approximation* (Sobolev 1957, 1960). The key idea of this approximation is to turn this spatial integral into an integral over comoving frame frequency. In order to do this, Sobolev assumed that the line profile function is very narrow, δ-function like, and over a length scale L_{Sob} which is small compared to hydrodynamic scale lengths, the density remains fairly constant. As such, the optical depth integral becomes a function of *local* variables only,

$$\tau_\nu(r) = \kappa\rho(r) \int_{R_*}^{r} \phi\left(x - \frac{\hat{\mathbf{n}}\cdot\mathbf{v}(\mathbf{r}')}{v_{th}}\right) dr' \,. \tag{2.50}$$

Here, let us transform the frequency variable into the comoving frame frequency,

$$x' = x - \frac{\hat{\mathbf{n}}\cdot\mathbf{v}(\mathbf{r}')}{v_{th}} \,, \tag{2.51}$$

$$dx' = -\frac{1}{v_{th}} (\hat{\mathbf{n}}\cdot\nabla)(\hat{\mathbf{n}}\cdot\mathbf{v}(\mathbf{r}))\, dr' \,. \tag{2.52}$$

With these changes, the integral for the optical depth becomes:

$$\tau_\nu(r) = \frac{\kappa_L v_{th}\rho(r)}{(\hat{\mathbf{n}}\cdot\nabla)(\hat{\mathbf{n}}\cdot\mathbf{v}(\mathbf{r}))} \int_{x-\frac{\hat{\mathbf{n}}\cdot\mathbf{v}(\mathbf{r})}{v_{th}}}^{\infty} \phi(x')\, dx' \tag{2.53}$$

Like before, the limit of integration is extended to infinity. We can define the constant part of the integral, the Sobolev optical depth,

$$\tau_S \equiv \frac{\kappa_L v_{th} \rho(r)}{(\hat{\mathbf{n}} \cdot \nabla)(\hat{\mathbf{n}} \cdot \mathbf{v}(\mathbf{r}))} \,, \tag{2.54}$$

and

$$\Phi \equiv \int_{x - \frac{\hat{\mathbf{n}} \cdot \mathbf{v}(\mathbf{r})}{v_{th}}}^{\infty} \phi(x')\, dx' \tag{2.55}$$

Now the equation for the single line force can be rewritten in a convenient form:

$$\begin{aligned} \mathbf{g_L} &= \frac{\kappa_L \Delta\nu_D}{c} \oint \int_{x=-\infty}^{\infty} \phi(x')\, I_* e^{-\tau_S \Phi(x,r)}\, \hat{\mathbf{n}}\, d\Omega\; dx' \\ &= \frac{\kappa_L \Delta\nu_D}{c} \oint \int_{x=-\infty}^{\infty} I_* e^{-\tau_S \Phi(x,r)}\, \hat{\mathbf{n}}\; d\Omega\; d\Phi(x,r) \end{aligned} \tag{2.56}$$

This can be easily integrated to give:

$$\mathbf{g_L} = \frac{\kappa_L \Delta\nu_D}{c} \left(\oint I_* \hat{\mathbf{n}}\, d\Omega \left[\frac{1 - e^{-\tau_S}}{\tau_S} \right] \right) . \tag{2.57}$$

The term in the open bracket is the total flux of radiation at frequency ν and distance r, and for point-like star model we have:

$$g_L = \frac{\kappa_L v_{th}}{c^2} \frac{\nu_0 L_\nu}{4\pi r^2} \left[\frac{1 - e^{-\tau_S}}{\tau_S} \right] . \tag{2.58}$$

In the approximation of a point-like star, the Sobolev optical depth collapses into a simpler form,

$$\tau_S = \frac{\kappa_L v_{th} \rho(r)}{\partial v_r / \partial r} \,. \tag{2.59}$$

For most hot stars, the lines in consideration are near the peak of the continuum spectrum, as such we can assume $\nu_0 L_\nu \approx L_*$. Thus,

$$g_L = \frac{\kappa_L v_{th}}{c^2} \frac{L_*}{4\pi r^2} \left[\frac{1 - e^{-\tau_S}}{\tau_S} \right] . \tag{2.60}$$

2.5.4 Force Due to an Ensemble of Lines

In the previous section we formulated the radiation force due to a single line in the stellar wind. In reality, the total radiative acceleration is produced by a large number of lines. In order to account for the contributions from all the lines one has to sum over all of them,

$$g_{lines} = \sum_{lines} \frac{\kappa_L v_{th}}{c^2} \frac{L_*}{4\pi r^2} \left[\frac{1 - e^{-\tau_S}}{\tau_S} \right] , \tag{2.61}$$

where g_{lines} is the cumulative force due to the ensemble of lines.

In practice, the number of lines is huge, and can be expressed as a statistical distribution. In its original formulation, CAK considered an extensive list of subordinate lines of C^{+3} and parameterized the line-force via a power law fit in tems of *force multiplier*, $M(t)$ as a function of the electron-scattering optical depth , t,

$$g_{lines} \propto M(t) \propto k\, t^{-\alpha} , \tag{2.62}$$

where $t = \kappa_e \rho v_{th}/(\partial v_r/\partial r)$, k defines the overall strength of the lines, and α determines the fraction of optically thick lines. Owocki, Castor, & Rybicki (1988, OCR hereafter) generalized this, and formulated a number distribution of lines as an exponentially-truncated power law,

$$\frac{dN(\kappa)}{d\kappa} = \frac{1}{\kappa_0} \left(\frac{\kappa_L}{\kappa_0} \right)^{\alpha-2} e^{-\kappa/\kappa_{max}} \tag{2.63}$$

where κ_0 is a normalization constant that is related to the CAK k parameter by $\kappa_0 = \Gamma(\alpha)(v_{th}/c)(\kappa_0/\kappa_e)^{1-\alpha}/(1-\alpha)$; the cutoff κ_{max} limits the the maximum line strength (OCR); κ_e is the electron scattering coefficient and $\Gamma(\alpha)$ is the complete Gamma function. With this distribution of lines, the summation in the above equation can be replaced by an integral over κ,

$$\begin{aligned} g_{lines} &= \sum_{lines} g_L \\ &= \int_0^\infty g_L \frac{dN}{d\kappa_L}\, d\kappa_L \end{aligned}$$

$$= \int_0^\infty \frac{\kappa_L v_{th}}{c^2} \frac{L_*}{4\pi r^2} \left[\frac{1-e^{-\tau_S}}{\tau_S}\right] \frac{1}{\kappa_0} \left(\frac{\kappa_L}{\kappa_0}\right)^{\alpha-2} e^{-\kappa/\kappa_{max}}\, d\kappa_L\,. \qquad (2.64)$$

This integral can be readily integrated using the definition of τ_S (eqn 2.59), yielding,

$$g_{lines} = \frac{\Gamma(\alpha)}{1-\alpha} \frac{\kappa_0 v_{th}}{c} \frac{L_*}{4\pi r^2 c} \left[\frac{\kappa_0\, v_{th}\rho(r)}{\partial v_r/\partial r}\right]^{-\alpha} \left(\frac{(\tau_{max}+1)^{1-\alpha}-1}{\tau_{max}^{1-\alpha}}\right), \qquad (2.65)$$

with $\tau_{max} \equiv \kappa_{max}\, v_{th}\, \rho(r)/(\partial v_r/\partial r)$. For $\tau_{max} \gg 1$ the term in the round bracket equals unity, and we retrieve the original CAK force. In this work, for the sake of simplicity we shall ignore this correction term in what follows since its contribution is negligible in any case. Note however that the expression above contains the thermal velocity of the ion, v_{th}. The quantity κ_0 which is related to the line strength, is dependent on v_{th}. As such, the appearance of the thermal speed is redundant.

Gayley (1995), in his excellent paper, recast the CAK line-force in terms of $\bar{Q}$ that is closely related to the classical oscillator strength and eliminates v_{th} from the line-force expression. He assumed the following identity:

$$\frac{\kappa_0 v_{th}}{c} \equiv \bar{Q}\ \kappa_e\, \Gamma(\alpha)^{-\frac{1}{1-\alpha}}\,. \qquad (2.66)$$

Here $\bar{Q}$ remains fairly constant at ~ 1000 for most O and B stars. With a little algebra, we can rewrite the line-force as:

$$g_{lines} = \frac{1}{(1-\alpha)}\ \frac{\bar{Q}\kappa_e L_*}{4\pi r^2 c} \left(\frac{\partial v/\partial r}{\rho c \bar{Q}\kappa_e}\right)^{\alpha} \qquad (2.67)$$

Throughout this work, we will follow Gayley's formalism of the CAK force.

2.6 Solution to the 1-D CAK Wind

In this section we outline the possible solutions to a wind that is subject to the CAK force as derived in equation 2.67. Since the line force is very dominant in hot-star winds, the gas pressure plays virtually no role, and one can ignore it altogether to a good approximation. Thus the momentum equation for 1-D time-steady radial flow of line-driven wind becomes:

$$v\frac{dv}{dr} \;=\; -(1-\Gamma)\frac{GM}{r^2} \;+\; \frac{\bar{Q}\kappa_e L}{4\pi r^2 c}\ \frac{1}{1-\alpha} \left[\frac{dv/dr}{\bar{Q}\kappa_e \rho c}\right]^{\alpha}$$

$$= -(1-\Gamma)\frac{GM}{r^2} + \frac{\bar{Q}\kappa_e L}{4\pi r^2 c}\,\frac{1}{1-\alpha}\left[\frac{4\pi r^2 v\,dv/dr}{\bar{Q}\kappa_e \dot{M} c}\right]^{\alpha} \tag{2.68}$$

In the second line in the above equation we used the mass continuity equation, $\dot{M} = 4\pi r^2 \rho v$. To simplify this equation let us divide both sides by the effective gravity $(1-\Gamma)GM/r^2$ and define inertial acceleration in this unit,

$$w \equiv \frac{r^2 v dv/dr}{(1-\Gamma)GM}\,. \tag{2.69}$$

Thus,

$$\begin{aligned} w &= -1 + \frac{L}{c^{1+\alpha}(1-\alpha)\dot{M}^{\alpha}}\left[\frac{4\pi GM(1-\Gamma)}{\bar{Q}\kappa_e}\right]^{\alpha-1} w^{\alpha} \\ &\equiv -1 + Cw^{\alpha} \end{aligned} \tag{2.70}$$

Here, the constant $C \sim 1/\dot{M}^{\alpha}$ determines the mass loss rate, and the solution to the above dimensionless equation will depend on this constant. To show this let us first rearrange the above equation:

$$Cw^{\alpha} = w + 1 \tag{2.71}$$

Figure 2.6 illustrates the graphical solution to the above equation for various values of C. The left hand side (LHS) of the equation represents the line force, and the right hand side (RHS) tells us how much of it goes into inertia (w) vs. gravity. For high $\dot{M}$ or small C there are no solutions, while for small $\dot{M}$ or high C there are two solutions. The intermediate of these two is the critical solution that corresponds to maximal CAK mass loss rate solution. It requires that Cw^{α} line intersect the $1+w$ line tangentially, i.e.

$$C_c \alpha w^{\alpha-1} = 1 \tag{2.72}$$

If we solve for w, we obtain,

$$w = \frac{\alpha}{1-\alpha} = constant\,. \tag{2.73}$$

Now the constant C_c becomes,

$$C_c = \frac{(1-\alpha)^{\alpha-1}}{\alpha^\alpha} \tag{2.74}$$

Using the definition for C and after some simple algebraic manipulations, one finds that:

$$\dot{M}_{CAK} = \frac{L}{c^2}\,\frac{\alpha}{1-\alpha}\left[\frac{\bar{Q}\Gamma}{1-\Gamma}\right]^{(1-\alpha)/\alpha} \tag{2.75}$$

Notice that the complete Gamma function, $\Gamma(\alpha)$ disappeared. This is due to the definition of $\bar{Q}$ in equation (2.66). If we assume $\alpha = 1/2$, we can integrate equation (2.73) to obtain the following velocity law for line-driven hot-star winds:

$$v(r) = \sqrt{\frac{\alpha}{1-\alpha}}\, v_{esc}\left(1 - \frac{R_*}{r}\right)^{1/2}, \tag{2.76}$$

where $v_{esc} = \sqrt{2GM(1-\Gamma)/R_*}$ is the escape speed from the stellar surface. Note that the terminal speed here is nearly equal to escape speed, $v_\infty = \sqrt{\alpha/(1-\alpha)}v_{esc}$. In fact, for $\alpha = 1/2$ they are exactly equal. This is the classical CAK solution of line-driven winds. For the general case with $0 < \alpha < 1$, one can fit the velocity solution with:

$$v(r) = v_\infty\left(1 - \frac{R_*}{r}\right)^{\beta}, \tag{2.77}$$

where the exponent β determines how steeply the velocity reaches the terminal speed. The solution we derived above (eqn. 2.76) is widely known in the literature as the $\beta = 1/2$ velocity law. It underestimates observed terminal velocities for most hot stars. In the next section we discuss an extension of this model that takes into account the finite size of the star.

2.7 Finite Disk Correction Factor

In the above analysis, we assumed that the star is a point like source. That enabled us to derive a relatively simple form of the line force. In reality, stars have finite size, and especially near the surface it has significant dynamical effects on the

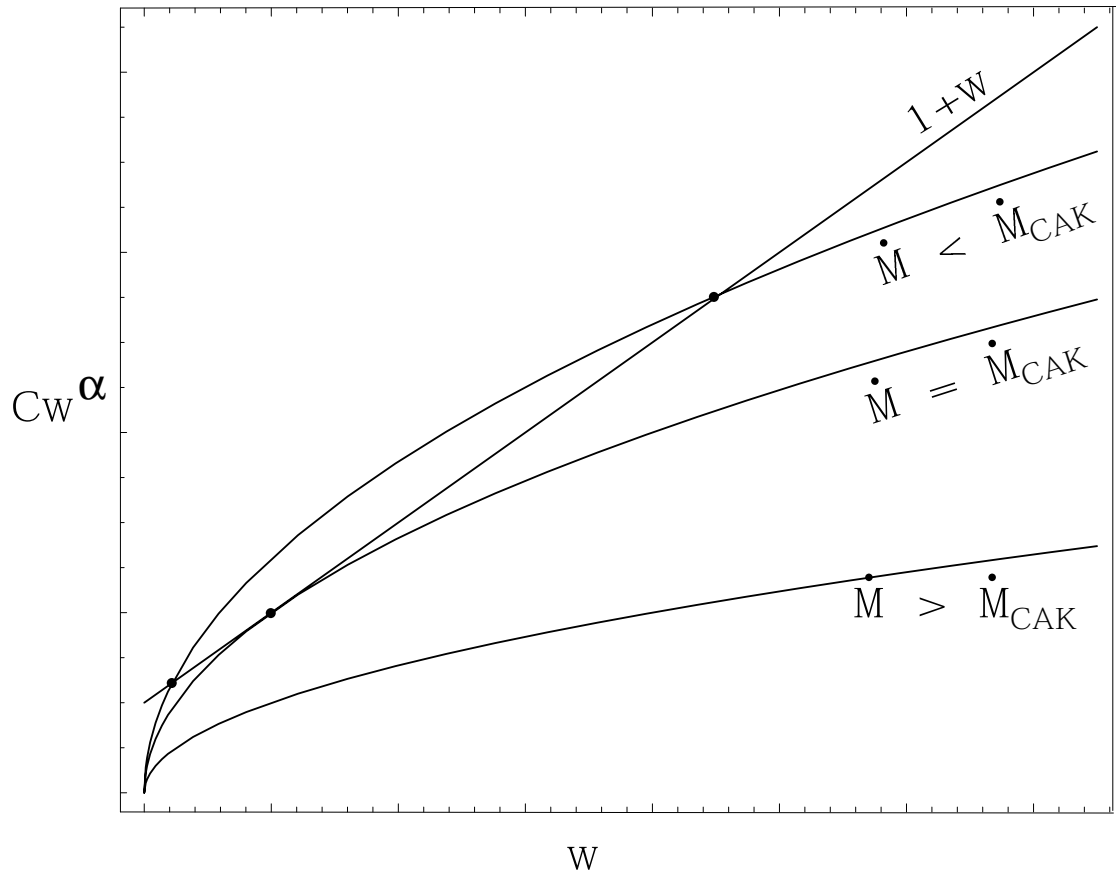

Figure 2.6: Graphical solutions of the dimensionless equation of motion () representing 1D CAK wind solutions. If $\dot{M}$ is big, there are no solution;if $\dot{M}$ is small there are two solutions; only the critical value of $\dot{M} = \dot{M}_{CAK}$ gives a single solution.

wind outflow. This arises due to the presence of non-radial rays from the stellar disk. In this section we will derive this effect of the finite size of the star on the line force. We assume spherical symmetry with $\hat{\mathbf{n}}$ along the z-axis and purely radial wind outflow,

$$\hat{\mathbf{n}} = \mu' \, \hat{\mathbf{r}} + \sqrt{1-\mu'^2} \; \hat{\theta}' \,, \tag{2.78}$$

$$\mathbf{v} = v_r \, \hat{\mathbf{r}} \tag{2.79}$$

where $\mu' = \cos\theta'$. The general velocity gradient can be derived as,

$$(\hat{\mathbf{n}} \cdot \nabla)(\hat{\mathbf{n}} \cdot \mathbf{v}(\mathbf{r})) = \mu'^2 \frac{\partial v_r}{\partial r} + \frac{v_r}{r}(1-\mu'^2) \tag{2.80}$$

$$= \frac{\partial v_r}{\partial r} \frac{\sigma\mu'^2 + 1}{\sigma + 1} \,, \tag{2.81}$$

where we have defined

$$\sigma \equiv \frac{\partial \ln v_r}{\partial \ln r} - 1 \,. \tag{2.82}$$

The bolometric intensity can be expressed as:

$$I_*(r, \theta', \phi') = \frac{L_*}{4\pi R_*^2} \, D(\mu', r) \tag{2.83}$$

with the limb darkening function $D(\mu', r)$. For simplicity, we will assume a uniformly bright disk,

$$D(\mu', r) = \begin{cases} 0 & \text{if } -1 \le \mu' < \mu_* \\ 1/\pi & \text{if } \mu_* < \mu' \le +1 \end{cases}$$

where

$$\mu_* \equiv \sqrt{1 - \frac{R_*^2}{r^2}} \tag{2.84}$$

defines the cosine of the angle subtended by the stellar disk. The radial line force we have derived in equation (2.67) now can be rewritten as,

$$g_{lines} = \frac{1}{(1-\alpha)} \; \frac{\bar{Q}\kappa_e L_*}{4\pi R_*^2 c} \left(\frac{1}{\rho c \bar{Q} \kappa_e} \right)^{\alpha} 2\pi \int_{-1}^{+1} D(\mu', r) \left[\frac{\partial v_r}{\partial r} \, \frac{\sigma\mu'^2 + 1}{\sigma + 1} \right]^{\alpha} d\mu' \,. \tag{2.85}$$

The integration is straightforward and yields,

$$g_{lines} = \frac{1}{(1-\alpha)} \frac{\bar{Q}\kappa_e L_*}{4\pi R_*^2 c} \left(\frac{\partial v_r/\partial r}{\rho c \bar{Q}\kappa_e} \right)^{\alpha} \frac{(\sigma+1)^{\alpha+1} - (\mu_*^2\sigma+1)^{\alpha+1}}{\sigma(\alpha+1)(\sigma+1)^{\alpha}} \,. \tag{2.86}$$

We can recast the above expression by rewriting R_*^2 as $r^2(1-\mu_*^2)$.

$$g_{lines} = \frac{1}{(1-\alpha)} \frac{\bar{Q}\kappa_e L_*}{4\pi r^2 c} \left(\frac{\partial v_r/\partial r}{\rho c \bar{Q}\kappa_e} \right)^{\alpha} \left[\frac{(\sigma+1)^{\alpha+1} - (\mu_*^2\sigma+1)^{\alpha+1}}{\sigma(1-\mu_*^2)(\alpha+1)(\sigma+1)^{\alpha}} \right] . \tag{2.87}$$

The term in the square bracket in the above equation is the only extra term compared to the expression of the line-force for the case of a point source (eqn 2.67). In the literature this is called as *finite disk correction* factor, f_d, and appears as equation (50) in CAK (1975),

$$f_d = \frac{(\sigma+1)^{\alpha+1} - (\mu_*^2\sigma+1)^{\alpha+1}}{\sigma(1-\mu_*^2)(\alpha+1)(\sigma+1)^{\alpha}} \tag{2.88}$$

Throughout this work we will assume this form of f_d. We will see in chapter 4, that it plays an important role in the dynamics of hot-star winds and the negligence of this factor may be rather misleading.

As a sample, figure 2.7 shows the finite disk correction factor f_d assuming a β-velocity law (eqn. 2.77) and $\alpha = 1/2$ for various values of *beta*, noted on the figure, against radius (logarithmic scale). Note that f_d starts at about ≈ 0.70, rises above unity around the isotropic expansion point, then finally approaches unity asymptotically.

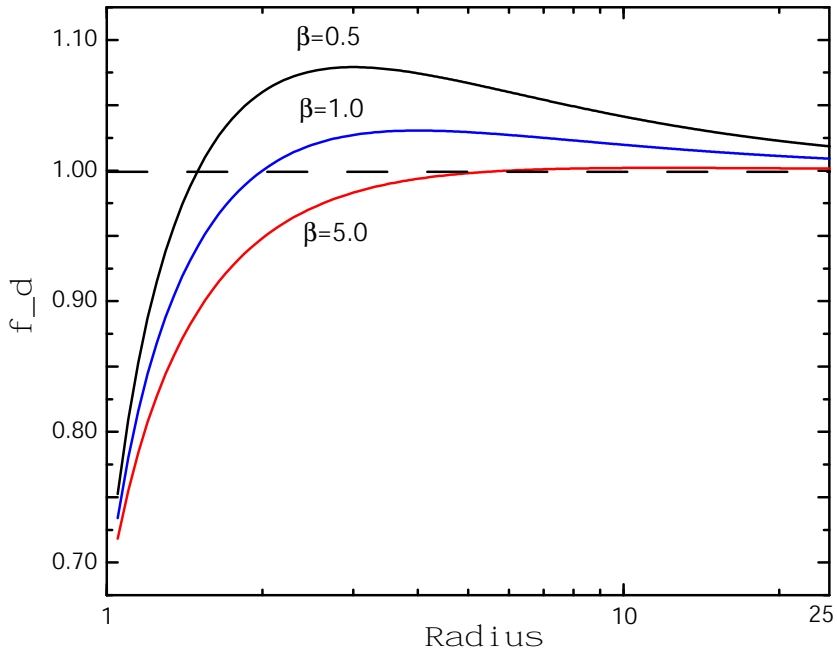

Figure 2.7: The finite disk correction factor plotted against radius for assumed β-velocity law and $\alpha = 1/2$. The three curves correspond to $\beta = 0.5, 1.0$ and 5.0 (top to bottom).

Chapter 3

MAGNETICALLY CHANNELED LINE-DRIVEN WINDS

3.1 Introduction

Hot[1], luminous, OB-type stars have strong stellar winds, with asymptotic flow speeds up to $v_\infty \sim 3000$ km/s and mass loss rates up to $\dot{M} \sim 10^{-5} M_\odot$ /yr. As was mentioned earlier, these general properties are well-explained by modern extensions (e.g. Pauldrach, Puls, and Kudritzki 1986) of the basic CAK formalism for wind driving by scattering of the star's continuum radiation in a large ensemble of spectral lines.

However there is also extensive evidence that such winds are not the steady, smooth outflows envisioned in these spherically symmetric, time-independent, CAK-type models, but instead have extensive structure and variability on a range of spatial and temporal scales. Relatively small-scale, stochastic structure – e.g. as evidenced by often quite constant soft x-ray emission (Long & White 1980), or by UV lines with extended black troughs understood to be a signature of a nonmonotonic velocity field (Lucy 1982) – seems most likely a natural result of the strong, intrinsic instability of the line-driving mechanism itself (Owocki 1994; Feldmeier 1995). But larger-scale structure – e.g. as evidenced by explicit UV line profile variability in even low signal-to-noise IUE spectra (Kaper et al. 1996; Howarth & Smith 1995) – seems instead likely to be the consequence of wind perturbation by processes

[1] A paper based on the material in this chapter has been accepted for publication in ApJ September 2002; Authors: ud-Doula, A. & Owocki, S.

occurring in the underlying star. For example, the photospheric spectra of many hot stars show evidence of radial and/or non-radial pulsation, and in a few cases there is evidence linking this with observed variability in UV wind lines (Telting, Aerts, & Mathias 1997; Mathias et al. 2001).

An alternate scenario – one explored through dynamical simulations in this chapter – is that, in at least some hot stars, surface magnetic fields could perturb, and perhaps even channel, the wind outflow, leading to rotational modulation of wind structure that is diagnosed in UV line profiles, and perhaps even to magnetically confined wind-shocks with velocities sufficient to produce the relatively hard x-ray emission seen in some hot-stars.

The sun provides a vivid example of how a stellar wind can be substantially influenced by a surface magnetic field. Both white-light and x-ray pictures show the solar corona to be highly structured, with dense loops where the magnetic field confines the coronal gas, and low-density coronal holes where the more radial magnetic field allows a high-speed, pressure-driven, coronal outflow (Zirker 1977). In a seminal paper, Pneuman and Kopp (1971) provided the first magnetohydrodynamical (MHD) model of this competition between magnetic confinement and coronal expansion. Using an iterative scheme to solve the relevant partial differential equations for field and flow, they showed that this competition leads naturally to the commonly observed 'helmet' streamer configuration, for which the field above closed magnetic loops is extended radially outward by the wind outflow. Nowadays such MHD processes can be readily modelled using time-dependent MHD simulation codes, such as the Versatile Advection Code (Keppens and Goedbloed 1999), or the publicly available ZEUS codes (Stone and Norman 1992). Here we apply the latter to study MHD processes within *line-driven* stellar winds that have many characteristics quite distinct from the *pressure-driven* solar wind.

For the solar wind, the acceleration to supersonic speeds can take several

solar radii; as such, magnetic loops that typically close within a solar radius or so can generally maintain the coronal gas in a nearly hydrostatic configuration. As we show below, in the more rapid line-acceleration of hot-stars winds, strong magnetic confinement typically channels an already supersonic outflow, often leading to strong shocks where material originating from different footpoints is forced to collide, with compressed material generally falling back to the star in quite complex and chaotic patterns. In the solar wind, the very low mass-loss-rate, and thus the low gas density and pressure, mean that only a modest magnetic field strength, of order of a Gauss, is sufficient to cause significant confinement and channeling of the coronal expansion. In hot-star winds, magnetic confinement or channeling generally requires a much stronger magnetic field, on the order of hundreds of Gauss. As such, a key issue underlying the study here regards the theoretical prospects and observational evidence for hot-star magnetic fields of this magnitude.

In the sun and other cool stars, magnetic fields are understood to be generated through a dynamo mechanism, in which coriolis forces associated with stellar rotation deflect convective motions in the hydrogen and helium recombination zones. In hot stars, hydrogen remains fully ionized even through the atmosphere, and so, lacking the strong convection zones associated with hydrogen recombination, such stars have traditionally been considered not to have strong, dynamo-generated magnetic fields. However, considering the generally quite rapid rotation of most hot stars, dynamo-generation may still be possible, e.g. within thin, weaker, near-surface convection zones associated with recombination of fully ionized helium.

Moreover, the interior, energy-generation cores of such massive stars are thought to have strong convection, and recently Cassinelli and Macgregor (2000; see also Charbonneau and MacGregor 2001) have proposed that dynamo-generated magnetic flux tubes from this interior could become buoyant, and thus drive an upward diffusion to the surface over a time-scale of a few million years. Such a model

would predict surface appearance of magnetic fields in hot-stars that have evolved somewhat from the zero-age-main sequence. Alternatively, magnetic fields could form from an early, convective phase during the star's initial formation, or perhaps even arise through compression of interstellar magnetic flux during the initial stellar collapse. Such primordial models would thus predict magnetic fields to be strongest in the youngest stars, with then some gradual decay as the star evolves.

In recent years there has been considerable effort to develop new techniques, e.g. based on the Hanle effect, to observationally detect stellar magnetic fields (Ignace, Nordsieck, & Cassinelli 1997; Ignace, Cassinelli, & Nordsieck 1999). The Hanle effect is related to the polarization arising from resonance-line scattering in the presence of relatively weak magnetic fields. It is applicable when the magnetic sublevels of a line transition are sufficiently close in frequency that the natural line widths of these sublevels overlap significantly. Consequently, the existence of quantum mechanical coherences leads to an interference between the polarized line components, resulting in changes of the polarization of the scattered light. With Hanle effect one can detect magnetic fields $1 \lesssim B \lesssim 1000$ G. When the magnetic field strength is larger than 1000 G, the sublevels of the line transition are distinctly separated and the Zeeman effect starts to dominate.

The Zeeman effect represents the most direct and well-demonstrated method to determine the magnetic field strength in stars through the separation of the sublevels and associated circular polarization of stellar photospheric absorption lines (Borra & Landstreet 1980). This technique has been used extensively in direct measurement of the quite strong magnetic fields that occur in the chemically peculiar Ap and Bp stars (Babcock 1960; Borra et al. 1980; Bohlender 1993; Mathys 1995; Mathys et al. 1997). For more 'normal' (i.e., chemically non-peculiar) hot stars, the generally strong rotational line-broadening severely hinders the direct spectropolarimetric detection of their generally much weaker fields, yielding instead mostly

only upper limits, typically of order a few hundred Gauss. This, coincidentally and quite tantalizingly, is similar to the level at which magnetic fields can be expected to become dynamically significant for channeling the wind outflow.

Recently, however, there have been first reports of positive field detections in a few normal hot stars. For the relatively slowly rotating star β Cephei, Henrichs et al. (2000) and Donati et al. (2001) report a 3-sigma detection of a ca. 400 G dipole field, with moreover a rotational modulation suggesting the magnetic axis is tilted to be nearly perpendicular to the stellar rotation. There are also initial reports (Donati 2001) of a ca. 1000 G dipole field in θ^1 Ori C, in this case with the magnetic axis tilted by about 45 degrees to the rotation. For Ap and Bp stars, the most generally favored explanation for their strong fields is that they may be primordial, and the relative youth of θ^1 Ori C also seems to suggest a primordial model. In contrast, the more evolved evolutionary status of β Cephei seems to favor the interior-eruption scenario.

The focus of the work in this chapter is to carry out magnetohydrodynamical simulations of how such magnetic fields on the surface of hot stars can influence their radiatively driven stellar wind. Our approach here represents a natural extension of the previous studies by Babel & Montmerle (1997a,b; hereafter BM97a,b), which effectively *prescribed* a fixed magnetic field geometry to channel the wind outflow. For large magnetic loops, wind material from opposite footpoints is accelerated to a substantial fraction of the wind terminal speed (i.e. $\sim$ 1000 km/s) before the channeling toward the loop tops forces a collision with very strong shocks, thereby heating the gas to temperatures ($10^7 - 10^8$ K) that are high enough to emit hard (few keV) x-rays. This 'magnetically confined wind shock' (MCWS) model was initially used to explain x-ray emission from the Ap-Bp star IQ Aur (BM97a), which has a quite strong magnetic field ($\sim$ 4kG) and a rather weak wind (mass loss rate $\sim 10^{-10} M_\odot$/ yr), and thus can indeed be reasonably modeled within the framework

of prescribed magnetic field geometry.[2] Later, BM97b applied this model to explain the periodic variation of x-ray emission of the O7 star θ^1 Ori C, which has a much lower magnetic field ($\lesssim$ 1000 G) and significantly stronger wind (mass loss rate $\sim 10^{-7} M_\odot$/ yr), raising now the possibility that the wind itself could influence the field geometry in a way that is not considered in the simple fixed-field approach.

The simulation models presented here are based on an isothermal approximation of the complex energy balance, and so can provide only a rough estimate of the level of shock heating and x-ray generation. But a key advantage over previous approaches is that these models do allow for such a fully dynamical competition between the field and flow. A central result is that the overall effectiveness of magnetic field in channeling the wind outflow can be well characterized in terms of single 'wind magnetic confinement parameter' η_*, defined in eqn. (3.7) below, and related to the relative energy densities of field and wind (§3.3). The specifics of our numerical MHD method are described in §3.2, while §3.4 details the results of a general parameter study of hot-star winds with various degrees of magnetic confinement. Following a discussion (§3.5) of the implications of these results for modeling hot-star wind structure and variability, we finally conclude (§3.6) with a summary and outlook for future work.

3.2 Numerical Method

3.2.1 Magnetohydrodynamic Equations

Our general approach is to use the ZEUS-3D (Stone and Norman 1992) numerical MHD code to evolve a consistent dynamical solution for a line-driven stellar

[2] However, note that even in this case the more-rapid radial decline in magnetic vs. wind energy density means that the wind outflow eventually wins, drawing out portions of the surface field into a radial, open configuration. Such open-field regions can only be heuristically accounted for in the fixed-field modeling approach.

wind from a star with a dipolar surface field. As described further below, the basic ZEUS-3D code was modified for the present study to include radiative driving terms, and to allow for specification of the lower boundary conditions. The code is designed to be easily adapted to run in a variety of flow geometries (planar, cylindrical, spherical) in one, two, or three dimensions. Our implementation here uses spherical polar coordinates with radius r, co-latitude θ, and azimuth ϕ in a 2D formulation, which assumes all quantities are constant in azimuthal angle ϕ, and that the azimuthal components of both field and flow vanish, $B_\phi = v_\phi = 0$.

The time-dependent equations to be numerically integrated thus include the conservation of mass,

$$\frac{D\rho}{Dt} + \rho \nabla \cdot \mathbf{v} = 0, \tag{3.1}$$

and the equation of motion

$$\rho \frac{D\mathbf{v}}{Dt} = -\nabla p + \frac{1}{4\pi}(\nabla \times \mathbf{B}) \times \mathbf{B} - \frac{GM(1-\Gamma)\hat{\mathbf{r}}}{r^2} + \mathbf{g}_{lines}, \tag{3.2}$$

where ρ, p, and $\mathbf{v}$ are the mass density, gas pressure, and velocity of the fluid flow, and $D/Dt = \partial/\partial t + \mathbf{v}\cdot\nabla$ is the advective time derivative. The gravitational constant G and stellar mass M set the radially directed ($\hat{\mathbf{r}}$) gravitational acceleration, and $\Gamma \equiv \kappa_e L/(4\pi GMc)$ is the Eddington parameter, which accounts for the acceleration due to scattering of the stellar luminosity L by free electron opacity κ_e, with c the speed of light. The additional radiative acceleration due to *line* scattering, $\mathbf{g}_{lines}$, is discussed further below. The magnetic field $\mathbf{B}$ is constrained to be divergence free

$$\nabla \cdot \mathbf{B} = 0, \tag{3.3}$$

and, under our assumption of an idealized MHD flow with infinite conductivity (e.g. Priest & Hood 1991), its inductive generation is described by

$$\frac{\partial \mathbf{B}}{\partial t} = \nabla \times (\mathbf{v} \times \mathbf{B}). \tag{3.4}$$

The ZEUS-3D code can also include an explicit equation for conservation of energy, but in the dense stellar winds considered here, the energy balance is dominated by radiative processes that tend to keep the wind near the stellar effective temperature T_{eff} (Drew 1989; Pauldrach 1987). In this initial study, we assume an explicitly isothermal flow with $T = T_{eff}$, which thus implies a constant sound speed $a = \sqrt{kT/m}$, with k Boltzmann's constant and m the mean atomic weight of the gas. The perfect gas law then gives the pressure as $p = \rho a^2$. In such an isothermal model, even the locally strong compressive heating that occurs near shocks is assumed to be radiated away within a narrow, unresolved cooling layer (Castor 1987; Feldmeier et al. 1997; Cooper 1994). We thus defer to future work the quantitative modeling of the possible EUV and x-ray emission of any such shocks, although below (§5.3.4) we do use computed velocity jumps to provide rough estimates of the expected intensity and hardness of such shock emissions. (See figure 3.9.)

3.2.2 Spherically Symmetric Approximation for Radial Line-Force

The radiative acceleration $\mathbf{g}_{lines}$ results from scattering of the stellar radiation in a large ensemble of spectral lines. In these highly supersonic winds this can be modeled within the framework of the Sobolev (1960) approximation as depending primarily on the *local* velocity gradient averaged over the directions of the source radiation from the stellar disk. For 1D nonrotating winds, the line-force-per-unit-mass can be written in the form (cf. Abbott 1982; Gayley 1995)

$$g_{lines} = \frac{f}{(1-\alpha)} \frac{\kappa_e L \bar{Q}}{4\pi r^2 c} \left(\frac{dv/dr}{\rho c \bar{Q} \kappa_e} \right)^{\alpha} \tag{3.5}$$

where α is the CAK exponent, and f is the (1D) finite disk correction factor, given by CAK eqn. (50) (See also Friend and Abbott 1986, and Pauldrach, Puls, and Kudritzki 1986). Here we choose to follow the Gayley (1995) line-distribution normalization $\bar{Q}$, which offers the advantages of being a dimensionless measure of line-opacity that is independent of the assumed ion thermal speed v_{th}, and with a nearly

constant characteristic value of order $\bar{Q} \sim 10^3$ for a wide range of ionization conditions (Gayley 1995). This normalization is related to the usual CAK parameter through $k = \bar{Q}^{1-\alpha} \ (v_{th}/c)^{\alpha} \ /(1-\alpha)$.

In the 2D wind models computed here, the line force (3.5) should in principle be modified to take account of gradients in other velocity components, such as might arise from, e.g., latitudinal flow along magnetic loops. Such latitudinal gradients can modify the form of the radial finite-disk correction factor f, and can even lead to a non-zero *latitudinal* component of the full vector line force. In a rotating stellar wind, asymmetries in the velocity gradient between the approaching and receding stellar hemisphere can even lead to a net *azimuthal* line force (Owocki, Cranmer, and Gayley 1996; Gayley and Owocki 2000). For simplicity, we defer study of such rotational and latitudinal affects to future work, and thus apply here just the radial, 1D form (3.5) for the line force, within a 2D, axisymmetric model of a non-rotating stellar wind.

3.2.3 Numerical Specifications

Let us next describe some specifics of our numerical discretization and boundary conditions. In our implementation of the ZEUS MHD code, flow variables are specified on a fixed 2D spatial mesh in radius and co-latitude, $\{r_i, \theta_j\}$. The mesh in radius is defined from an initial zone $i = 1$, which has a left interface at $r_1 = R_*$, the star's surface radius, out to a maximum zone ($i = n_r = 300$), which has a right interface at $r_{301} = 6R_*$. Near the stellar base, where the flow gradients are steepest, the radial grid has an initially fine spacing with $\Delta r_1 = 0.00026 R_*$, and then increases by 2% per zone out to a maximum of $\Delta r_{299} = 0.11 R_*$.

The mesh in co-latitude uses $n_\theta = 100$ zones to span the two hemispheres from one pole, where the $j = 1$ zone has a left interface at $\theta_1 = 0^o$, to the other pole, where the $j = n_\theta = 100$ zone has a right interface at $\theta_{101} = 180^o$. To facilitate resolution of compressed flow structure near the magnetic equator at $\theta = 90^o$, the

zone spacing has a minimum of $\Delta\theta_{50} = 0.29^o$ at the equator, and then increases by 5% per zone toward each pole, where $\Delta\theta_1 = \Delta\theta_{100} = 5.5^o$. Test runs with half the resolution in radius and/or latitude showed some correspondingly reduced detail in flow fine-structure, but overall the results were qualitatively similar to those for the standard resolution.

Our operation uses the piecewise-linear-advection option within ZEUS (van Leer 1977), with time steps set to a factor 0.30 of the minimum MHD Courant time computed within the code (Courant et al. 1953). Boundary conditions are implemented by specification of variables in two phantom zones. At both poles, these are set by simple *reflection* about the boundary interface. At the outer radius, the flow is invariably super-Alfvenic outward, and so outer boundary conditions for all variables (i.e. density, and the radial and latitudinal components of both the velocity and magnetic field) are set by simple *extrapolation* assuming constant gradients.

The boundary conditions at the stellar surface are specified as follows. In the two radial zones below $i = 1$, we set the radial velocity v_r by constant-slope extrapolation, and fix the density at a value ρ_o chosen to ensure subsonic base outflow for the characteristic mass flux of a 1D, nonmagnetic CAK model, i.e. $\rho_o \approx \dot{M}/(4\pi R_*^2 a/5)$. Detailed values for each model case are given in Table 1. In our 2D magnetic models, these conditions allow the mass flux and the radial velocity to adjust to whatever is appropriate for the local overlying flow (Owocki, Castor, and Rybicki 1988). In most zones, this corresponds to a subsonic wind outflow, although inflow at up to the sound speed is also allowed.

Magnetic flux is introduced through the radial boundary as the radial component of a dipole field $B_r(R_*) = B_o \cos(\theta)$, where the assumed polar field B_o is a fixed parameter for each model (see Table 1). The latitudinal component of magnetic field, B_θ, is set by constant slope extrapolation. The specification for the

latitudinal velocity, v_θ, differs for strong vs. weak field cases. For strong fields (defined by the magnetic confinement parameter $\eta_* > 1$; see §3.3), we again use linear extrapolation. (We also find similar results using $v_\theta = v_r B_\theta / B_r$.) For weak fields ($\eta_* \leq 1$), we simply set $v_\theta = 0$. Tests using each approach in the intermediate field strength case ($\eta_* = 1$) gave similar overall results.

This time-dependent calculation also requires us to specify an *initial condition* for each of these flow variables over the entire spatial mesh at some starting time $t = 0$. The hydrodynamical flow variables ρ and $\mathbf{v}$ are initialized to values for a spherically symmetric, steady, radial CAK wind, computed from relaxing a 1D, non-magnetic, wind simulation to an asymptotic steady state. The magnetic field is initialized to have a simple dipole form with components $B_r = B_o (R_*/r)^3 \cos\theta$, $B_\theta = (B_o/2)(R_*/r)^3 \sin\theta$, and $B_\phi = 0$, with B_o the polar field strength at the stellar surface. From this initial condition, the numerical model is then evolved forward in time to study the dynamical competition between the field and flow. The results of such dynamical simulations are described in §4.4.

3.3 Heuristic Scaling Analysis for Field vs. Flow Competition

3.3.1 The Wind Magnetic Confinement Parameter

To provide a conceptual framework for interpreting our MHD simulations, let us first carry out a heuristic scaling analysis of the competition between field and flow. To begin, let us define a characteristic parameter for the relative effectiveness of the magnetic fields in confining and/or channeling the wind outflow. Specifically, consider the ratio between the energy densities of field vs. flow,

$$\begin{aligned} \eta(r,\theta) &\equiv \frac{B^2/8\pi}{\rho v^2/2} \\ &\approx \frac{B^2 r^2}{\dot{M} v} \\ &= \left[\frac{B_*^2(\theta) {R_*}^2}{\dot{M} v_\infty}\right] \left[\frac{(r/R_*)^{2-2q}}{1 - R_*/r}\right], \end{aligned} \tag{3.6}$$

where the latitudinal variation of the surface field has the dipole form given by $B_*^2(\theta) = B_o^2(\cos^2\theta + \sin^2\theta/4)$. In general, a magnetically channeled outflow will have a complex flow geometry, but for convenience, the second equality in eqn. (3.6) simply characterizes the wind strength in terms of a spherically symmetric mass loss rate $\dot{M} = 4\pi r^2 \rho v$. The third equality likewise characterizes the radial variation of outflow velocity in terms of the phenomenological velocity law $v(r) = v_\infty(1 - R_*/r)$, with v_∞ the wind terminal speed; this equation furthermore models the magnetic field strength decline as a power-law in radius, $B(r) = B_*(R_*/r)^q$, where, e.g., for a simple dipole $q = 3$.

With the spatial variations of this energy ratio thus isolated within the right square bracket, we see that the left square bracket represents a dimensionless constant that characterizes the overall relative strength of field vs. wind. Evaluating this in the region of the magnetic equator ($\theta = 90^o$), where the tendency toward a radial wind outflow is in most direct competition with the tendency for a horizontal orientation of the field, we can thus define a equatorial 'wind magnetic confinement parameter',

$$\begin{aligned} \eta_* &\equiv \frac{B_*^2(90^o){R_*}^2}{\dot{M} v_\infty} \\ &= 0.4\,\frac{B_{100}^2\,R_{12}^2}{\dot{M}_{-6}\,v_8}, \end{aligned} \tag{3.7}$$

where $\dot{M}_{-6} \equiv \dot{M}/(10^{-6}\,M_\odot/\mathrm{yr})$, $B_{100} \equiv B_o/(100\ \mathrm{G})$, $R_{12} \equiv R_*/(10^{12}\ \mathrm{cm})$, and $v_8 \equiv v_\infty/(10^8\ \mathrm{cm/s})$. As these stellar and wind parameters are scaled to typical values for an OB supergiant, e.g. ζ Pup, the last equality in eqn. (3.7) immediately suggests that for such winds, significant magnetic confinement or channeling should require fields of order $\sim$ 100 G. By contrast, in the case of the sun, the much weaker mass loss ($\dot{M}_\odot \sim 10^{-14}\ M_\odot/\mathrm{yr}$) means that even a much weaker global field ($B_o \sim 1$ G) is sufficient to yield $\eta_* \simeq 40$, implying a substantial magnetic confinement of the solar coronal expansion. This is consistent with the observed

large extent of magnetic loops in optical, UV and x-ray images of the solar corona.

3.3.2 Alfven Radius and Magnetic Closure Latitude

The inverse of the energy density ratio defined in eqn. (3.6) also represents the square of an Alfvenic Mach number $M_A \equiv v/v_A$, where $v_A \equiv B/\sqrt{4\pi\rho}$ is the Alfven speed. We can thus estimate from eqns. (3.6) and (3.7) that the Alfven radius $R_A(\theta)$ (at which $M_A(R_A) \equiv 1$) satisfies

$$\left[\frac{R_A(\theta)}{R_*}\right]^{2q-2} - \left[\frac{R_A(\theta)}{R_*}\right]^{2q-3} = \eta_* \left[4 - 3\sin^2(\theta)\right] . \tag{3.8}$$

Figure 3.1 plots solutions of this estimate of the polar ($\theta = 0$; solid curve) and equatorial ($\theta = 90^o$; dashed curve) Alfven radius versus the confinement parameter η_* for various values of the magnetic exponent q. The circles compare the actual computed Alfven radii near the magnetic poles (filled) and equator (open) for our MHD simulations, as will be discussed further below (§§3.4, 3.5.1).

This heuristic solution for the Alfven radius can be used (cf. BM97a) to estimate the maximum radius of a closed loop.[3] For an assumed dipole field, this loop has surface footpoints at colatitudes θ_A satisfying

$$\theta_A = \arcsin\left[\sqrt{\frac{R_*}{R_A(\theta = 0)}}\right] , \tag{3.9}$$

which thus give the latitudes $\pm|90 - \theta_A|^o$ bounding the region of magnetic closure about the equator.

The discussion in §5.1 examines how well these heuristic scaling arguments match the results of the full MHD simulations that we now describe.

3.4 MHD Simulation Results

Let us now examine results of our MHD simulations for line-driven winds. Our general approach is to study the nature of the wind outflow for various assumed

[3] BM97a denote this as L_A, for the value of their 'magnetic shell parameter' L that intersects the Alfven radius.

values of the wind magnetic confinement parameter η_*. We first confirm that, for sufficiently weak confinement, i.e., $\eta_* \leq 0.01$, the wind is essentially unaffected by the magnetic field. But for models within the range $1/10 < \eta_* < 10$, the field has a significant influence on the wind. For our main parameter study, the variations in η_* are implemented solely through variations in the assumed magnetic field strength, with the stellar and wind parameters fixed at values appropriate to a typical OB supergiant, e.g. ζ Pup, as given in Table 1. Following this, we briefly (§4.4) compare flow configurations with identical confinement parameter, η_*, but obtained with different stellar and wind parameters.

3.4.1 Time Relaxation of Wind to a Dipole Field

As noted above, we study the dynamical competition between field and wind by evolving our MHD simulations from an initial condition at time $t = 0$, when a dipole magnetic field is suddenly introduced into a previously relaxed, 1D spherically symmetric CAK wind. For the case of moderately strong magnetic confinement, $\eta_* = \sqrt{10}$ ($B_o = 520$ G), figure 3.2 illustrates the evolution of magnetic field (lines) and density (gray scale) at fixed time snapshots, t =0, 10, 25, 50, 100, and 450 ksec. Note that the wind outflow quickly stretches the initial dipole field outward, opening up closed magnetic loops and eventually forcing the field in the outer wind into a nearly radial orientation. This outward field-line stretching implies a general enhancement of the magnetic field magnitude in the outer wind, as evidenced in figure 3.2 by the increased density of field lines at the later times. This global relaxation of field and flow is completed within the first $50-100$ ksec, corresponding to about 2-4 times the characteristic flow crossing time, $t_{flow} = 5R_*/v_\infty \simeq 25$ ksec.

To ascertain the asymptotic behavior of flows with various magnetic confinement parameters η_*, we typically run our simulations to a time, $t = 450$ ksec, that is much longer (by factor $\sim$18) than this characteristic flow time. Generally we find that, after the initial relaxation period of $\sim 50 - 100$ ksec, the outer wind

remains in a nearly stationary configuration, with nearly steady, smooth outflow along open field lines. However, for cases with sufficiently strong magnetic field $\eta_* > 1$, confinement by closed loops near the equatorial surface can lead to quite complex flows, with persistent, intrinsic variability. Before describing further this complex structure near the stellar surface, let us first examine the simpler, nearly steady flow configurations that result in the outer wind.

3.4.2 Global Wind Structure for Strong, Moderate, and Weak Fields

Figure 3.3 illustrates the global configurations of magnetic field, density, and radial and latitudinal components of velocity at the final time snapshot, $t = 450$ ksec after initial introduction of the dipole magnetic field. The top, middle, and bottom rows show respectively results for a weak, moderate, and strong field, characterized by confinement parameters of $\eta_* = 1/10$, 1, and 10.

For the weak magnetic case $\eta_* = 1/10$, note that the flow effectively extends the field to almost a purely radial configuration everywhere. Nonetheless, even in this case the field still has a noticeable influence, deflecting the flow slightly toward the magnetic equator (with peak latitudinal speed $\max(v_\theta) \simeq 70$ km/s) and thereby leading to an increased density and a decreased radial flow speed in the equatorial region.

For the moderate magnetic strength $\eta_* = 1$, this equatorward deflection becomes more pronounced, with a faster latitudinal velocity component ($\max(v_\theta) \simeq 300$ km/s), and a correspondingly stronger equatorial change in density and radial flow speed. The field geometry shows moreover a substantial nonradial tilt near the equatorial surface.

For the strong magnetic case $\eta_* = 10$, the near-surface fields now have a closed-loop configuration out to a substantial fraction of a stellar radius above the surface. Outside and well above the closed region, the flow is quasi-steady, though

now with substantial channeling of material from higher latitudes toward the magnetic equator, with $\max(v_\theta) > 500$ km/s, even outside the closed loop. This leads to a very strong flow compression, and thus to a quite narrow equatorial "disk" of dense, slow outflow.

This flow configuration is somewhat analogous to the "Wind Compressed Disk" model developed for non-magnetic, rotating winds (Bjorkman and Cassinelli 1993; Owocki, Cranmer, and Blondin 1994). Indeed, it was already anticipated as a likely outcome of magnetic channeling, e.g. by BM97b, and in the "WC-Fields" paradigm described by Ignace, Bjorkman and Cassinell (1998). It is also quite analogous to what is found for strong field channeling in other types of stellar wind (Matt et al. 2000), including even the solar wind (Keppens and Goedbloed 1999 2000).

3.4.3 Variability of Near-Surface Equatorial Flow

In contrast to this relatively steady, smooth nature of the outer wind, the flow near the star can be quite structured and variable in the equatorial regions. For the strong magnetic field case $\eta_* = 10$, the complex structure of the flow within the closed magnetic loops near the equatorial surface is already apparent even in the global contour plots in the bottom row of figure 3.3. To provide a clearer illustration of this variable flow structure, Figure 3.4 zooms in on the near-star equatorial region, comparing density (upper row, contours), mass flux (arrows), and field lines (lower row) at an arbitrary time snapshot long after the initial condition ($t > 400$ ksec), for three models with magnetic confinement numbers $\eta_* = 1$, $\sqrt{10}$, and 10.

For the case of moderate magnetic field with $\eta_* = 1$, note the appearance of the high-density knot at a height $\sim 0.3R_*$ above the equatorial surface. As is suggested from the bow-shaped front on the inward-facing side of this knot, it is flowing *inward*, the result of a general infall of material that had been magnetically channeled into an equatorial compression, and thereby became too dense for the

radiative line-driving to maintain a net outward acceleration against the inward pull of the stellar gravity. This again is quite analogous to the inner disk infall found in dynamical simulations of rotationally induced Wind Compressed Disks (Owocki, Cranmer, and Blondin 1994).

Animations of the time evolution for this case show that such dense knots form repeatedly at semi-regular intervals of about 200 ksec. A typical cycle begins with a general building of the equatorial density through the magnetic channeling and equatorial compression of wind outflow from higher latitudes. As the radiative driving weakens with the increasing density, the equatorial outflow first decelerates and then reverses into an inflow that collects into the dense knot. Once the equatorial density is emptied by the knot falling onto the surface, the build-up begins anew, initiating a new cycle.

For the case of somewhat stronger field with $\eta_* = \sqrt{10}$, the snapshot at the same fixed time $t = 400$ ksec again shows evidence for an infalling knot, except that now this has been forced by the magnetic tension of an underlying, closed, equatorial loop to slide to one hemisphere (in this case north), instead of falling directly upon the equatorial stellar surface. Animations of this case show a somewhat more irregular repetition, with knots again forming about every 200 ksec, but randomly sliding down one or the other of the footpoint legs of the closed equatorial loop. It is interesting that, even though our simulations are formally symmetric in the imposed conditions for the two hemispheres, this *symmetry is spontaneously broken* when material from the overlying dense equatorial flow falls onto, and eventually off of, the top of the closed magnetic loop.

The strongest field case with $\eta_* = 10$ shows a much more extensive magnetic confinement, and accordingly a much more elaborate configuration for material re-accretion onto the surface. Instead of forming a single knot, the equatorially compressed material now falls back as a complex "snake" of dense structure that

breaks up into a series of dense knots, draining down the magnetic loops toward both northern and southern footpoints. In the time animations for as long as we have run this case, there is no clear repetition time, as the formation and infall of knots and snake-segments are quite random, perhaps even chaotic.

It is worth noting here that in the two stronger magnetic cases, the closed loops include a region near the surface for which the field is so nearly horizontal that it apparently *inhibits* any net upflow. As a consequence, these loops tend to become quite low density. This has an unfortunate practical consequence for our numerical simulations, since the associated increase in the Alfven speed requires a much smaller numerical time step from the standard Courant condition. Thus far this has effectively limited our ability to run such strong field models for the very extended time interval needed for clearer definition of the statistical properties of the re-accretion process.

In contrast to this effective inhibition of radial outflow by the nearly horizontal field in the central regions of a closed loop, note that in the outer portion of the loop, where the field is more vertical, the radial line-driving is able to initiate a supersonic flow up along the loop. But when this occurs along a field line that is still closed, the inevitable result is that material from opposite footpoints is forced to collide near the top of the loop. This effectively halts the outflow for that field line, with the accumulating material near the top of the loop supported by both the magnetic tension from below and the ram pressure of incoming wind from each side.

As the density builds, maintaining this support against gravity becomes increasingly difficult. For the moderate field strength, the material from all such closed flow tubes accumulates into a knot whose weight forces the loop top to buckle inward, first nearly symmetrically but eventually off toward one side, allowing the material to re-accrete toward that footpoint at the surface. For the strongest field, the loops tend to remain nearly rigid, keeping the material from distinct closed flow

Table 3.1: Summary Table

	Model							
							$\eta_* = \sqrt{10}$	
Quantity	$\eta_* = 0$	$\frac{1}{10}$	$\frac{1}{\sqrt{10}}$	1	$\sqrt{10}$	10	low $\dot{M}$	θ^1 Ori C
α	0.6	0.6	0.6	0.6	0.6	0.6	0.6	0.5
$\bar{Q}$	500	500	500	500	500	500	20	700
δ	0.0	0.0	0.0	0.0	0.0	0.0	0.0	0.1
$R_*(10^{12}cm)$	1.3	1.3	1.3	1.3	1.3	1.3	1.3	0.5
B_{Pole}(G)	0	93	165	295	520	930	165	480
$\rho_0(10^{-11}gm\,cm^{-3})$	4.3	4.3	4.3	4.3	4.3	4.3	0.54	2.8
$\max(v_r)(km\ s^{-1})$	2300	2350	2470	2690	2830	3650	2950	2620
$\max(v_\theta)(km\ s^{-1})$	0	70	150	300	400	1200	400	450
$\dot{M}_{net}(10^{-6}M_\odot\ yr^{-1})$	2.6	3.0	2.8	2.5	2.2	1.8	0.22	0.3

tubes separate and suspended at loop tops with a range of heights, until this line of material finally breaks up into segments (the "snake") that fall to either side of the rigid re-accretion tubes.

It is interesting to contrast this inferred outflow and re-accretion in the magnetic equator of a line-driven wind with what occurs in the solar coronal expansion. For the solar wind, acceleration to supersonic speeds typically occurs at a height of several solar radii above the surface. As such, magnetic loops that typically close within such heights can generally maintain the gas in a completely *hydrostatic* stratification. By contrast, in line-driven winds supersonic speeds are typically achieved very near the stellar surface, within about $0.1R_*$. A closed loop that starts from a radially oriented footpoint thus simply guides this line-driven outflow along the loop, instead of confining a hydrostatic stratification. For a strong field with sufficiently high loop top, the eventual shock collision can have velocity jumps that are a substantial fraction of the wind terminal speed, e.g. ~ 1000 km/s. In the present isothermal simulations, the heating from such shocks is assumed to be radiated away over a narrow, unresolved cooling layer. In the discussion in §3.5.3.4, we estimate some general properties of the associated x-ray emission.

3.4.4 Comparing Models with Different Stellar Parameters but Fixed η_*

The models above use different magnetic field strengths to vary the magnetic confinement for a specific O supergiant star with fixed stellar and wind parameters. To complement that approach, let us briefly examine models with a fixed confinement parameter $\eta_* = \sqrt{10}$, but now manifest through different stellar and/or wind parameters. Specifically, figure 3.5 compares density contours (top) and field lines (bottom) for our standard ζPup model (center panels), with a model in which the mass loss rate is reduced by a factor 10 (left panels), and also with a model based on entirely different stellar and wind parameters, intended roughly to represent the O7 star θ^1 Ori C (right panels). (Detailed parameter values are given in Table 1.)

Note that all three models have very similar overall *form* in both their density contours and field lines, even though the associated magnitudes vary substantially from case to case. This similarity of structure for models with markedly different individual parameters, but configured to give roughly equal η_*, thus further reinforces the notion that this confinement parameter is the key determinant in fixing the overall competition between field and flow.

3.5 Analysis and Discussion

3.5.1 Comparison of MHD Simulations with Heuristic Scaling Estimates

The above results lend strong support to the general idea, outlined in §3.3.1, that the overall effect of a magnetic field in channeling and confining the wind outflow depends largely on the single magnetic confinement parameter η_*. Let us now consider how well these MHD simulation results correspond to the heuristic estimates for the Alfven radius R_A and magnetic closure colatitude θ_A defined in §3.3.2.

Figure 3.6 plots contours of the Alfven radius obtained in the numerical MHD simulations with various η_*. Reflecting the stronger field and so higher Alfven

speed, the models with larger confinement parameter have a higher Alfven radius. Note, moreover, that for all cases the Alfven radius generally decreases toward the equator. In part, this just reflects the Alfven speed associated with the dipole surface magnetic field, which has a lower strength near the magnetic equator.

But the comparison in figure 3.6 shows a systematic discrepancy between the curves showing the expected Alfven radius from this dipole model and the points showing the actual MHD results. Specifically, the dipole model underestimates the MHD Alfven radius over the pole, and overestimates it at the equator.

For the polar wind, this can be understood as a consequence of the radial stretching of the field. Figure 3.7 plots the radial variation of the polar field ratio

$$f_{pole}(r) \equiv \frac{R_*^2 B_o}{r^2 B(r,0)} \tag{3.10}$$

for the various magnetic confinement parameters η_*. For comparison, a dipole field (with $B \sim r^{-q}$ and $q = 3$) would just give a straight line of unit slope (dashed line), whereas a pure monopole, radial field (with $q = 2$) would give a horizontal line at value unity, $f_{pole} = 1$.

The results show that the MHD cases are intermediate between these two limits. For the weakest confinement $\eta_* = 1/10$, the curve bends toward the horizontal at quite small heights, reflecting how even the inner wind is strong enough to extend the polar field into a nearly radial orientation and divergence. For the strongest confinement $\eta_* = 10$, the field divergence initially nearly follows the dashed line for a dipole ($q = 3$), but then eventually also bends over as the wind ram pressure overwhelms the magnetic confinement and again stretches the field into a nearly radial divergence. The intermediate cases show appropriately intermediate trends, but in all cases it is significant that the radial decline in field strength is generally less steep than for a pure dipole, i.e. $q < 3$. The dotted line in figure 3.1 indeed shows that the MHD results for the polar Alfven radii of the various confinement cases are in much better agreement with a simple scaling that assumes a radial decline (power

index $q = 2.6$) that is intermediate between the dipole ($q = 3$) and monopole (i.e. radial divergence, $q = 2$) limits.

Overall then, at the poles the radial stretching of field by the outflowing wind has the net effect of reducing the radial decline of field, and thus increasing the Alfven radius over the value expected from the simple dipole estimate of eqn. (3.8).

By contrast, at the equator this radial stretching has a somewhat opposite effect, tending to *remove* the predominantly *horizontal* components of the equatorial dipole field, and thus leading to a lower equatorial field strength and so also a lower associated Alfven radius, relative to the simple dipole analysis of §3.4.2. For example, for the lowest confinement case $\eta_* = 1/10$, the field is extended into a nearly radial configuration almost right from the stellar surface, as shown by the top left panel of figure 3.3; the equatorial polarity switch of this radial field thus implies a vanishing equatorial Alfven speed, which thus means that contours of Alfven radius must bend sharply inward toward the surface near the equator. For the strongest confinement case $\eta_* = 10$, the near-surface horizontal field within closed magnetic loops about the equator remains strong enough to resist this radial stretching by wind outflow; but the faster radial fall-off in magnetic vs. flow energy means that the field above these closed loops is eventually stretched outward into a radial configuration, thus again leading to a vanishing equatorial field and an associated inward dip in the Alfven radius.

This overall dynamical lowering of the equatorial strength of magnetic field further means that the latitudinal extents of closed loops in full MHD models are generally below what is predicted by the simple dipole estimate of eqn. (3.9). Thus, in previous semi-analytic models of BM97b, which effectively assume this type of dipole scaling, a somewhat larger surface field is needed to give the assumed overall extent of magnetic confinement.

3.5.2 Effect of Magnetic Field on Mass Flux and Flow Speed

Two key general properties of spherical, non-magnetic stellar winds are the mass loss rate $\dot{M} \equiv 4\pi\rho v_r r^2$ and terminal flow speed v_∞. To illustrate how a stellar magnetic field can alter these properties for a line-driven wind, figure 3.8 shows the outer boundary ($r = R_{max}$) values of the radial velocity, $v_r(R_{max}, \theta)$, and radial mass flux density, $\rho(R_{max}, \theta)v_r(R_{max}, \theta)$, normalized by the values (given in Table 1) for the non-magnetic, spherically symmetric wind case, and plotted as a function of $\mu = \cos(\theta)$ for each of our simulation models with various confinement parameters η_*.

There are several noteworthy features of these plots. Focussing first on the mass flux, note that in all models the tendency of the field to divert flow toward the magnetic equator leads to a general increase in mass flux there, with this equatorial compression becoming narrower with increasing field strength, until, for the strongest field, it forms the spike associated with an equatorial disk. This higher equatorial mass flux is associated with a higher density, since the equatorial flow speeds are always lower, quite markedly so for the dense, slowly outflowing disk of the strong field case.

Table 1 lists the overall mass loss rates, obtained by integration of these curves over the full range $-1 < \mu < 1$. For the strong field case, the mass loss is reduced relative to the non-magnetic $\dot{M}$, generally because the magnetic confinement and tilt of the inner wind outflow has effectively inhibited some of the base mass flux. Curiously, for the weakest magnetic confinement case $\eta_* = 1/10$, there is actually a modest overall *increase* in the mass loss. The reasons for this are not apparent, and will require further investigation.

3.5.3 Observational Implications of these MHD Simulations

3.5.3.1 UV Line-Profile Variability

It is worth emphasizing here that these dynamical results for the radial flow speed have potentially important implications for interpreting the observational evidence for wind structure and variability commonly seen in UV line profiles of hot stars (e.g., the so-called Discrete Absorption Components; Henrichs et al. 1994; Prinja and Howarth 1986; Howarth and Prinja 1989). In particular, an increasingly favored paradigm is that the inferred wind structure may arise from Corotating Interaction Regions (CIRs) between fast and slow speed wind streams. This requires a base perturbation mechanism to induce latitudinal variations in wind outflow properties from the underlying, rotating star (Mullan 1984; Cranmer and Owocki 1996). Based largely on the analogy with solar wind CIRs – for which the azimuthal variations in speed are clearly associated with magnetic structure of the solar corona (Zirker 1977; Pizzo 1978) –, there has been a longstanding speculation that surface magnetic fields on hot stars could similarly provide the base perturbations for CIRs in line-driven stellar winds (Mullan 1984; Shore & Brown 1990, Donati 2001).

However, until now, one argument *against* this magnetic model for hot-star-wind structure was the expectation, based largely on the Macgregor (1988) analysis, that a sufficiently strong field would likely lead to anomalously high-speed streams, in excess of 5000 km/s, representing the predicted factor of two or more enhancement above the speed for a non-magnetic wind (Owocki 1994; BM97a). By comparison, the wind flow speeds inferred quite directly from the blue edges of strong, saturated P-Cygni absorption troughs of UV lines observed from hot stars show only a modest variation of a few hundred km/s, with essentially *no evidence* for such extremely fast speeds (Prinja et al. 1998).

The full MHD results here are much more in concert with this inferred speed variation, even for the strongest field model, for which the fastest streams are not

much in excess of ∼3000 km/s. Moreover, in conjunction with the reduced flow speeds toward the magnetic equator, there is still quite sufficient speed contrast to yield very strong CIRs, if applied in a rotating magnetic star with some substantial tilt between magnetic and rotation axes. Through extensions of the current 2D models to a full 3D configuration, we plan in the future to carry out detailed simulations of winds from rotating hot-stars with such a tilted dipole surface field, applying these specifically toward the interpretation of observed UV line profile variability.

3.5.3.2 Infall within Confined Loops and Red-Shifted Spectral Features

In addition to the slowly migrating discrete absorption components commonly seen in the blue absorption troughs of P-Cygni profiles of UV lines, there are also occasional occurrences of *redward* features in either absorption (e.g., in τ Sco; Howk et al. 2000) or emission (e.g., in λ Eri and other Be or B supergiant stars; Peters 1986; Smith, Peters, and Grady 1991; Smith 2000; Kaufer 2000). Within the usual context of circumstellar material that is either in an orbiting disk or an outflowing wind, such redshifted spectral features have been difficult to understand, since they require material flowing *away* from the observer, either in absorption against the stellar disk, or in emission from an excess of receding material radiating from a volume not occulted by the star. In general this thus seems to require material *infall* back toward the star and onto the surface. Indeed, there have been several heuristic models that have postulated such infall might result from a stagnation of the wind outflow, for example due to clumping (Howk et al. 2000), or decoupling of the driving ions (Porter and Skouza 1999).

In this context, the dynamical MHD models here seem to provide another, quite natural explanation, namely that such infall is an inevitable outcome of the trapping of wind material within close magnetic loops whenever there sufficiently strong wind magnetic confinement, $\eta_* \geq 1$. In principle, such interpretations of observed red-shifts in terms of infall within closed magnetic loops could offer the

possibility of a new, indirect diagnostic of stellar magnetic properties. For example, the observed redshift speed could be associated with a minimum required loop height to achieve such a speed by gravitational infall. In future studies, we thus intend to generate synthetic line absorption and emission diagnostics for these MHD confinement models, and compare these with the above cited cases exhibiting redshifted spectral features.

3.5.3.3 Effect on Density-Squared Emission

In addition to such effects on spectral line profiles from scattering, absorption, or emission lines, the extensive compression of material seen in these MHD models should also lead to an overall enhancement of those types of emission, both in lines and continuum, for which the volume emission rate scales with the square of the density. Specific examples include line emission from both collisional excitation or recombination, or free-free continuum emission in the infrared and radio. In principle, the former might even lead to a net emission above the continuum in the hydrogen Balmer lines, and thus to formal classification as a Be star, even without the usual association of an orbiting circumstellar disk. Such a mechanism may in fact be the origin for the occasional occurrence of hydrogen line emission in slowly rotating B stars, most notably β Ceph, for which there has indeed now been a positive detection of a tilted dipole field of polar magnetic around 300 G (Donati et al. 2001; Henrichs et al. 2000). Again, further work will be needed to apply the dynamical MHD models here toward interpretation of observations of density-square emissions from hot stars that seem likely candidates for substantial wind magnetic confinement.

3.5.3.4 Implications for x-ray Emission

Particularly noteworthy among the potential observational consequences of these MHD models are the clear implications for interpreting the detection of sometimes quite hard, and even cyclically variable, x-ray emission from some hot stars. As noted in the introduction, there have already been quite extensive efforts to model such x-ray emission within the context of a fixed magnetic field that channels wind flow into strong shock collisions (BM97a,b). In contrast, while the isothermal MHD models here do not yet include the detailed energy balance treatment necessary for quantitative modeling of such shocked-gas x-ray emission, they do provide a much more complete and dynamically consistent picture of the field and flow configuration associated with such magnetic channeling and shock compression.

Indeed, as a prelude to future quantitative models with explicit computations of the energy balance and x-ray emission, let us briefly apply here an approximate analysis of our model results that can yield rough estimates for the expected level of compressional heating and associated x-ray production. The central idea is to assume that, within the context of the present isothermal models, any compressive heating that occurs is quickly balanced by radiative losses within a narrow, unresolved cooling layer (Castor 1987; Feldmeier et al. 1997; Cooper 1994). For shock-type compressions with a sufficiently strong velocity jump, this radiative emission should include a substantial component in the x-ray bandpass.

Applying this perspective, we first identify within our simulation models locations of locally strong compressions, i.e. where there are substantial zone to zone decreases in flow speed along the direction of the flow itself. Taking into account that the quadratic viscosity within the Zeus code typically spreads any shocks over about 3 or 4 zones, we can use this to estimate an associated total shock jump in the specific kinetic energy $\Delta v^2/2$. We then apply the standard shock jump conditions

to obtain a corresponding estimate of post-shock temperatures (BM97b),

$$T_s \approx 2.7 \times 10^5\, K\, \frac{-\Delta v^2/2}{(100\, km/s)^2}\,. \tag{3.11}$$

Figure 3.9c shows contours of T_s computed in this way for the strong confinement case $\eta_* = 10$. Note that quite high temperatures, in excess of 10^7 K, occur in both closed loops near the surface, as well as for the open-field, equatorial disk outflow in the outer wind. For the closed loops, where the field forces material into particularly strong, nearly head-on, shock collisions, this is as expected from previous fixed-field models (BM97a,b).

But for the open-field, equatorial disk outflow, the high-temperature compression is quite unexpected. Since the flow impingent onto the disk has a quite oblique angle, dissipation of just the normal component of velocity would not give a very strong shock compression. But this point of view assumes a "free-slip" post-shock flow, i.e., that the fast radial flow speed would remain unchanged by the shock. However, our simulations show that the radial speed within the disk is much slower. Thus, under the more realistic assumption that incoming material becomes fully entrained with the disk material, i.e. follows instead a "no-slip" condition, then the reduction from the fast radial wind speed implies a strong dissipation of radial flow kinetic energy, and thus a quite high post-shock temperature.

To estimate the associated magnitude of expected x-ray emission, we first compute the local volume rate of compressive heating, obtained from the negative divergence of the local kinetic energy flux,

$$q \equiv -\nabla \cdot (\mathbf{v}\rho v^2/2) \approx -\rho \mathbf{v} \cdot \nabla v^2/2\,. \tag{3.12}$$

The contours of q plotted in figure 3.9d again show that strong compressions are concentrated toward the magnetic equator, with again substantial levels occurring in both the inner, closed loops, as well as in the equatorial disk outflow.

Let us next combine these results to estimate the x-ray emission above some minimum threshold energy E, weighting the emission by a "Boltzmann factor" that declines exponentially with the ratio of this energy to the shock energy kT_s,

$$q_E \equiv q\, e^{-E/kT_s}\,. \tag{3.13}$$

Using the conversion that a soft x-ray energy threshold of $E = 0.1$ keV corresponds roughly to a temperature of 1.1×10^6 K, the contours in figure 3.9e show that soft x-rays above this energy would again be produced in both the inner and outer regions of the equatorial disk.

Figures 3.9 d and e show that the *volume* for flow compression and associated x-ray emission is quite limited, confined to narrow disk about the magnetic equator. Nonetheless, the strength of this emission can be quite significant. For example, volume integration of the regions defined in figure 3.9d give a total rate of energy compression $L_c \sim 10^{36}$ erg/s, which represents about 25% of the total wind kinetic energy, $L_w \sim \dot{M} v_\infty^2/2 \sim 4 \times 10^{36}$ erg/s.

This is consistent with the fraction of mass loss in the slowly outflowing, equatorial disk, which has a value $\dot{M}_{eq} \sim 5 \times 10^{-7}\ M_\odot$/yr, or about the same 25% of the total wind mass loss rate $\dot{M} \sim 2 \times 10^{-6}\, M_\odot$/yr. The terminal speed within this disk, $v_{eq} \sim 1000$ km/s, is about a third of that in the wind, $v_\infty \sim 3000$ km/s, implying nearly an order magnitude lower specific kinetic energy. The 'missing' energy associated with this slow disk outflow thus represents roughly the total wind flow kinetic energy dissipated by the flow into this slow disk.

Finally, integration of the Boltzmann-weighted emission in figure 3.9e gives an estimate for the soft x-ray emission above 0.1 keV of $L_x \sim 10^{35}$ erg/s. This is substantially higher than the canonical x-ray emission associated with intrinsic wind instabilities, $L_x \sim 10^{-7} L_{bol} \sim 4 \times 10^{32}$ erg/s. This supports the general notion that hot-stars with anomalously large, observed x-ray luminosities might indeed be explained by flow compressions associated with wind-magnetic channeling.

While this analysis thus provides a rough estimate of the x-ray emission properties expected from such MHD models of wind magnetic confinement, we again emphasize that quantitative calculations of expected x-ray emission levels and spectra requires an explicit treatment of the wind energy balance. In chapter 6 we make our first attempt to include full energy equation to study adiabatic line-driven winds.

3.6 Chapter Summary

We have carried out 2D MHD simulations of the effect of stellar dipole magnetic fields on radiatively driven stellar winds. The simulations in this chapter are based on idealizations of isothermal flow driven outward from a non-rotating star by a strictly radial line-force. The principal results are summarized as follows:

1. The general effect of magnetic field in channeling the stellar wind depends on the overall ratio of magnetic to flow-kinetic-energy density, as characterized by the wind magnetic confinement parameter, η_*, defined here in eqn. (3.7). For typical stellar and wind parameters of hot, luminous supergiants like ζ Pup, moderate confinement with $\eta_* \sim 1$ requires magnetic fields of order 100 Gauss. The results of standard, spherically symmetric, non-magnetic wind models are recovered in the limit of very small magnetic confinement, $\eta_* \leq 0.01$.

2. For moderately small confinement, $\eta_* = 1/10$, the wind extends the surface magnetic field into an open, nearly radial configuration. But even at this level, the field still has a noticeable global influence on the wind, enhancing the density and decreasing the flow speed near the magnetic equator.

3. For intermediate confinement, $\eta_* = 1$, the fields are still opened by the wind outflow, but near the surface retain a significant non-radial tilt, channeling the flow toward the magnetic equator with a latitudinal velocity component as high as 300 km/s.

4. For strong confinement, $\eta_* = 10$, the field remains closed in loops near the equatorial surface. Wind outflows accelerated upward from opposite polarity footpoints are channeled near the loop tops into strong collision, with characteristic shock velocity jumps of up to about 1000 km/s, strong enough to lead to hard (> 1 keV) x-ray emission.

5. Even for strong surface fields, the more rapid radial decline of magnetic vs. wind-kinetic-energy density means the field eventually becomes dominated by the flow, and extended into an open configuration.

6. The compression of open-field outflow into a dense, slowly outflowing equatorial disk can lead to shocks that are strong enough to produce quite hard x-ray emission, a possibility that was completely unaccounted for in previous fixed-field analyses that focussed only on x-ray emission within closed loops (BM97a,b).

7. In contrast to these previous steady-state, fixed-field models, the time-dependent dynamical models here indicate that stellar gravity pulls the compressed, stagnated material within closed loops into an infall back onto the stellar surface, often through quite complex, intrinsically variable flows that follow magnetic channels randomly toward either the north or south loop footpoint.

8. Compared with expectations of previous semi-analytic, heuristic analyses, the dynamical simulations here show some distinct differences in the overall properties of field and flow, for example with a narrower region of equatorial confinement, and an Alfven radius that is lower at the pole and higher at the equator.

9. Finally, these MHD simulations have many properties relevant to interpreting various kinds of observational signatures of wind variability and structure, e.g.

UV line discrete absorption components; red-shifted absorption or emission features; enhanced density-square emission; and x-ray emission.

In the future, we plan to extend our simulations to include non-radial line-forces, an explicit energy balance with x-ray emission, and stellar rotation. We then intend to apply these simulations toward quantitative modeling of the various observational signatures of wind structure that might be associated with magnetic fields in hot stars.

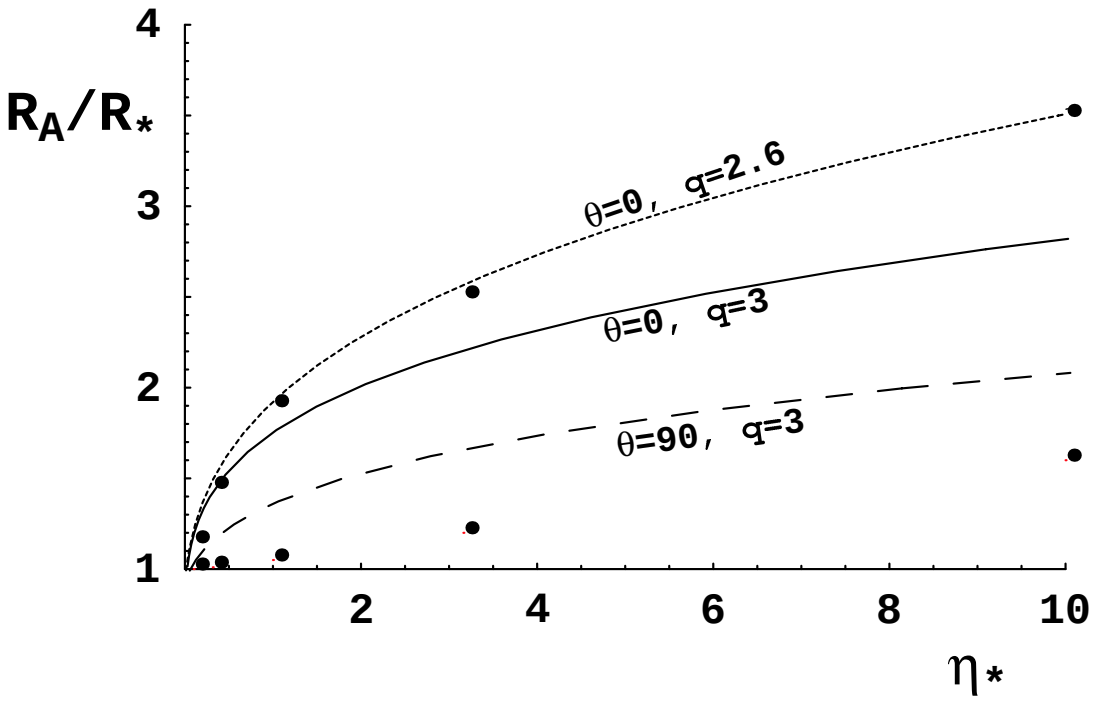

Figure 3.1: Variation Alfven radius R_A with magnetic confinement parameter η_*. The points indicate MHD simulation model results above the pole (upper set) or near the magnetic equator (lower set). The lines show estimates from the magnetic field approximation of eqn. (3.8), applied at the equator ($\theta = 90^o$; dashed line), or at the pole ($\theta = 0^o$), using radial decline power index for pure dipole ($q = 3$; solid line) or modified by wind radial expansion ($q = 2.6$; dotted line).

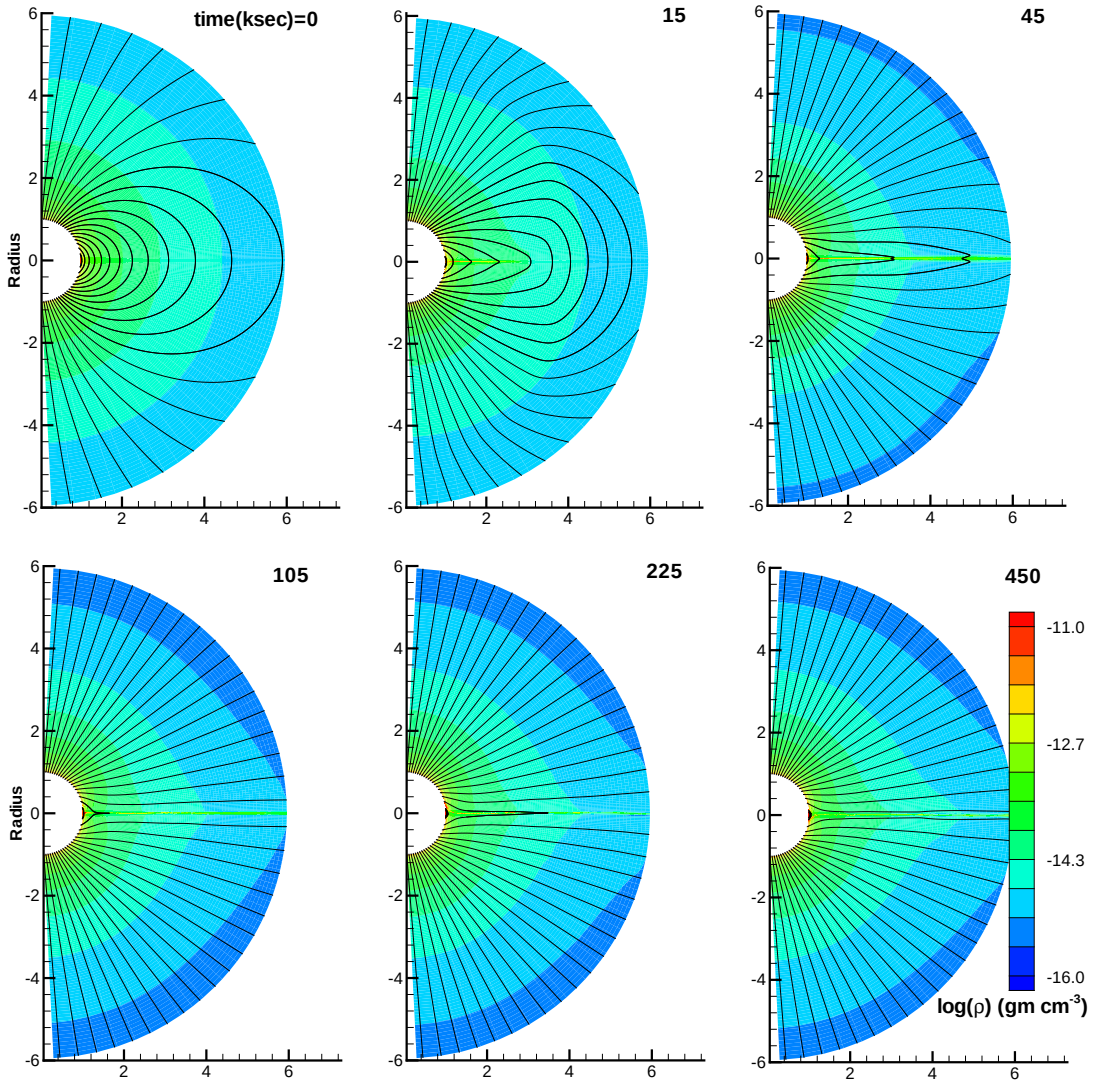

Figure 3.2: Snapshots of density (as logarithmic color-scale) and magnetic field (lines) at the labeled time intervals starting from the initial condition of a dipole field superposed upon a spherically symmetric outflow, for a case of moderate magnetic confinement $\eta_* = \sqrt{(10)}$ ($B_{Pole} = 520G$). The intervals of field lines emanating from the star are chosen to preserve the relationship of field-line density with the strength of magnetic field.

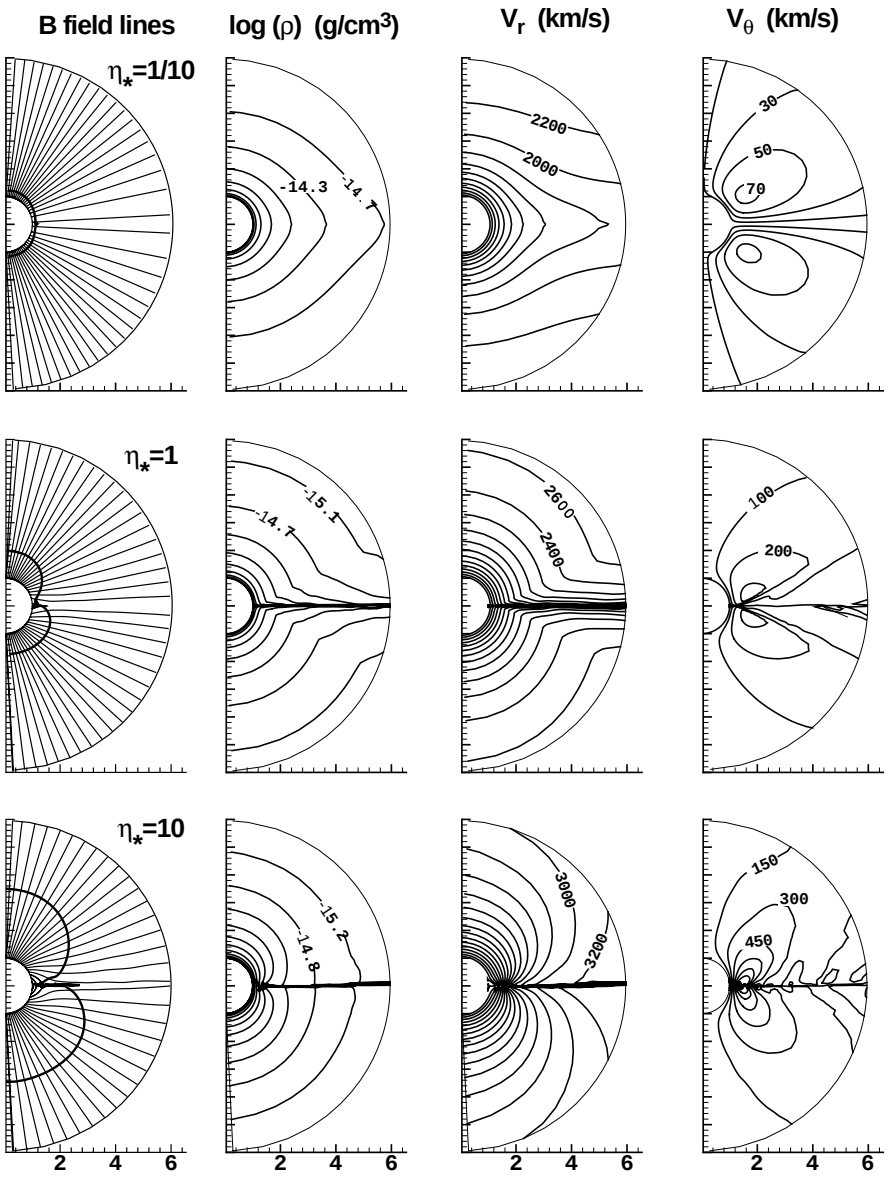

Figure 3.3: Comparison of overall properties at the final simulation time (t = 450 sec) for 3 MHD models, chosen to span a range of magnetic confinement from small (top row; $\eta_* = 1/10$), to medium (middle row; $\eta_* = 1$), to large (bottom row; $\eta_* = 10$). The leftmost panels show magnetic field lines, together with the location (bold contour) of the Alfven radius, where the radial flow speed equals the Alfven speed. From left to write, the remaining columns show contours of log(density), radial velocity, and latitudinal velocity.

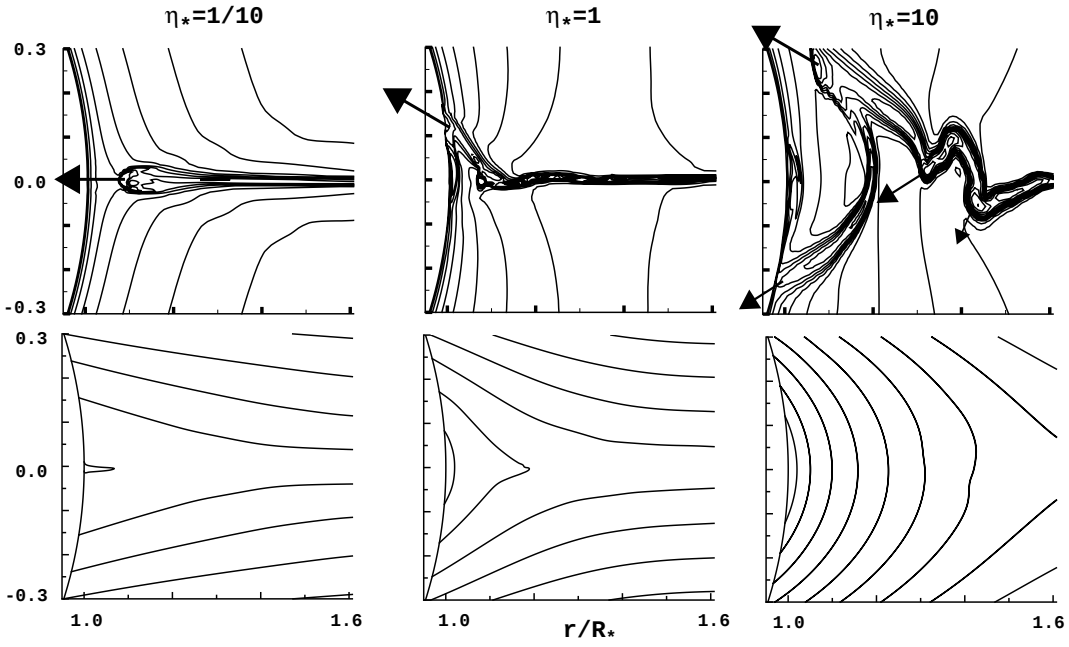

Figure 3.4: Contours of log(density) (upper row) and magnetic field lines (lower row) for the inner, magnetic-equator regions of MHD models with moderate ($\eta_* = 1$; left), strong ($\eta_* = \sqrt{10}$; middle), and strongest ($\eta_* = 10$; left) magnetic confinement, shown at a fixed, arbitrary time snapshot well after ($t \geq 400$ ksec) the initial condition. The arrows represent the direction and magnitude of the mass flux, and show clearly that the densest structures are undergoing an infall back onto the stellar surface. For the moderate magnetic confinement $\eta_* = 1$, this infall is directly along the equator, but for the higher confinements $\eta_* = \sqrt{10}$ and 10, the equatorial compressions that form at larger radii are deflected randomly toward the north or south as they fall in toward the closed field near the surface. The intent here is to illustrate how increasing magnetic confinement leads to an increasing complexity of flow and density structure within closed magnetic loops. This complexity is most vividly illustrated in the time animations available in the electronic version of the paper.

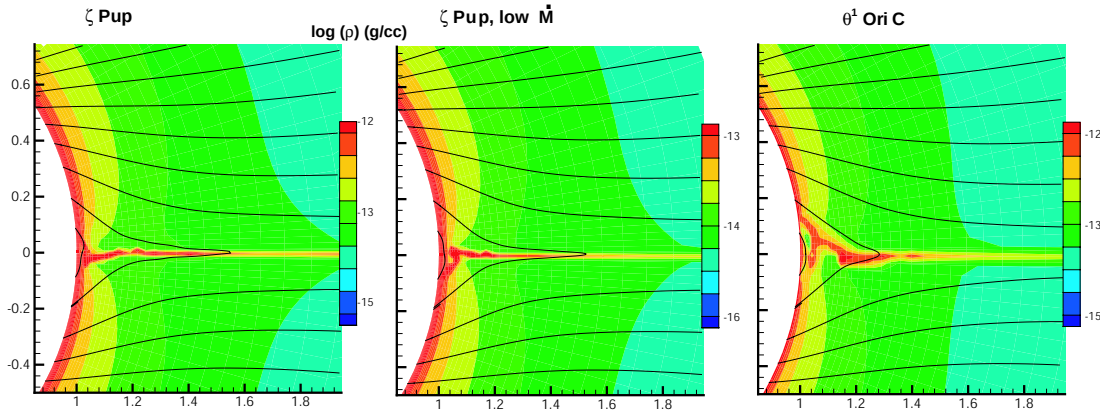

Figure 3.5: Contours for log of density (color-scale) and magnetic fields (lines) in the inner regions of 3 MHD models with a fixed magnetic confinement parameter $\eta_* = \sqrt{10}$, but obtained using different stellar and wind parameters, chosen to correspond to an O-type supergiant like ζ Pup with normal (left) or factor-ten lower mass loss rate (middle), or to a late-O giant like θ^1 Ori C (right). The overall similarity of the three models illustrates the degree to which the global configuration of field and flow depends mainly on just the combination of stellar, wind, and magnetic properties that define [via eqn. (3.7] the magnetic confinement parameter η_*.

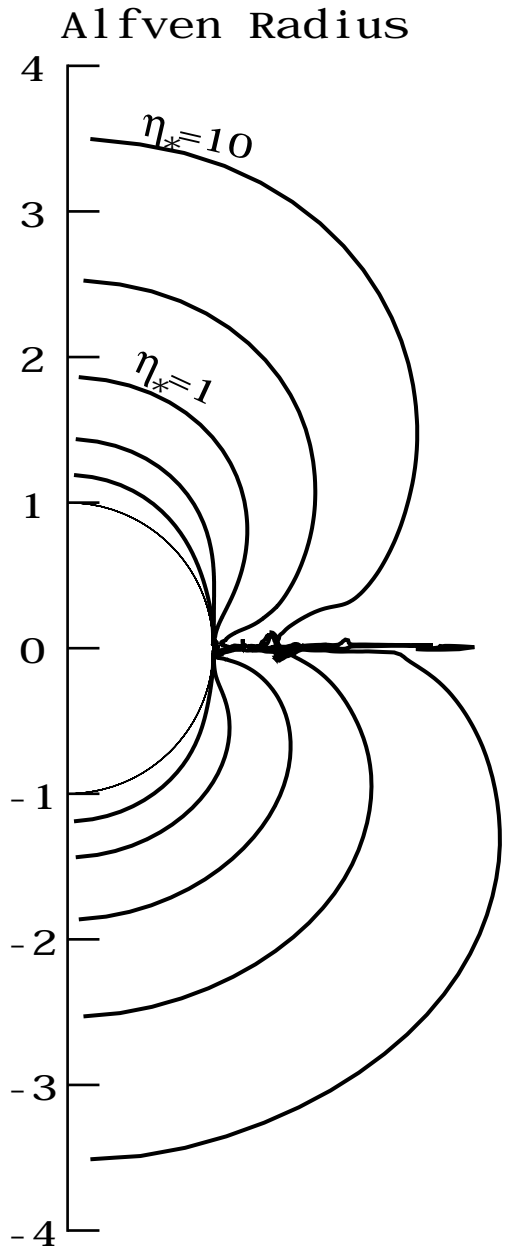

Figure 3.6: Contours of the Alfven radius in MHD models with confinement parameters (from inside-out) $\eta_* = 1/10$, $1/\sqrt{10}$, 1, $\sqrt{10}$, and 10.

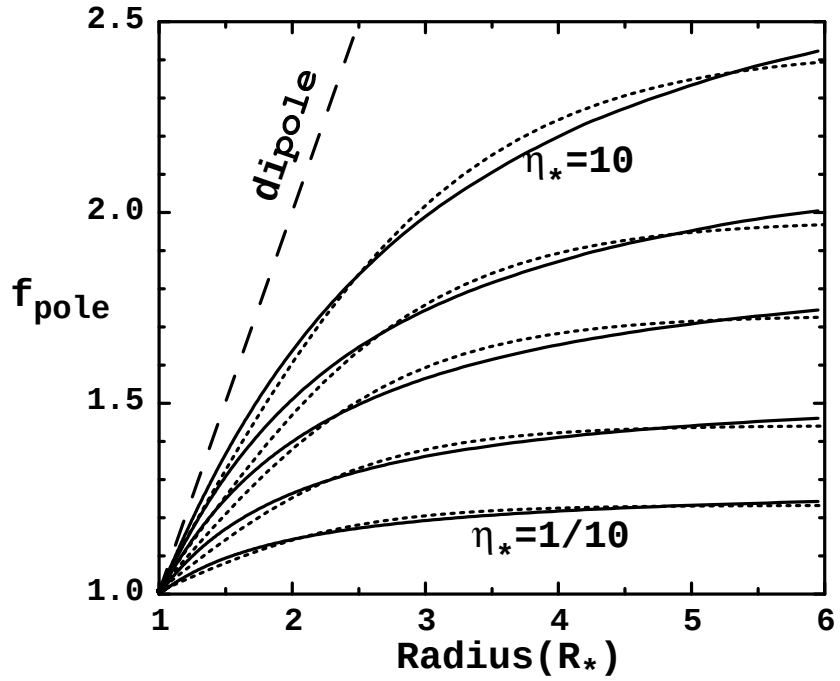

Figure 3.7: The measure of faster-than-r^2 decline of the polar magnetic field, as represented by the function f_{pole} defined in eqn. (3.10), and applied to the 5 MHD simulations with magnetic confinement ranging from strong ($\eta_* = 10$; uppermost curve) to weak ($\eta_* = 10$; lowermost curve). For the ideal MHD cases here of field-frozen flow, this also represents the degree of faster-than-r^2 expansion of flow tube area. The dotted curves plot the heuristic area-expansion function defined by Kopp and Holzer [discussed in chapter 4, eqn. (4.27)], with $R_1 = 1\ R_*$, and the parameters $f_{max} = 2.43$, 1.98, 1.73, 1.44 and 1.23, and $\sigma/R_* = 1.13$, 0.98, 0.89, 0.79, and 0.73, chosen to best fit to the five cases from η_* =10 to 1/10. The dashed curve shows the variation for a pure dipole field.

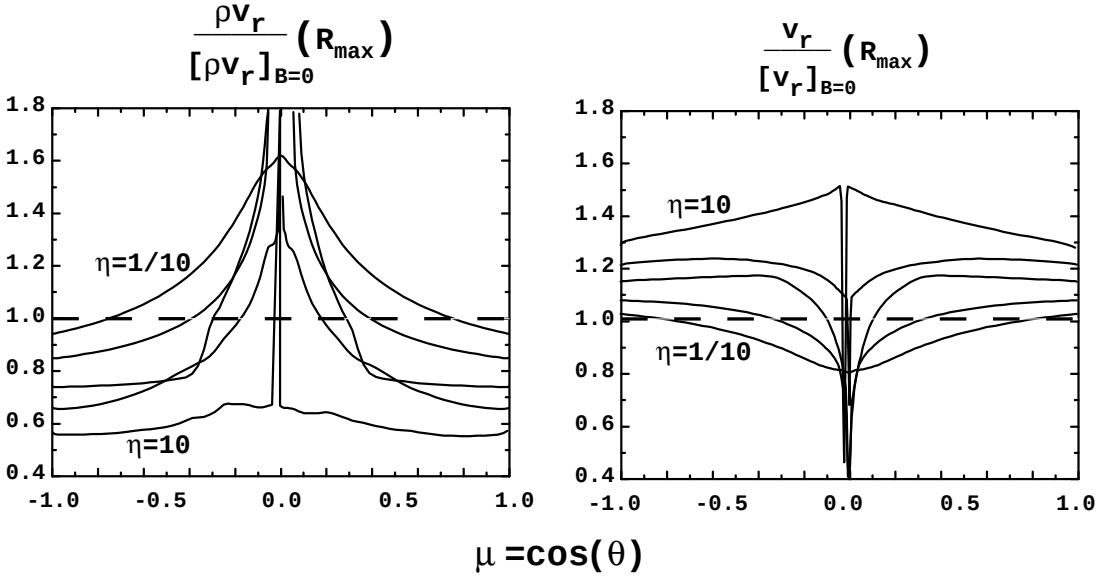

Figure 3.8: The radial mass flux density ρv_r (left) and radial flow speed v_r (right) at the maximum model radius $R_{max} = 6R_*$, normalized by values in the corresponding non-magnetic model, and plotted versus the cosine of the colatitude, $\cos(\theta)$, for the final time snaphsot ($t = 450$ ksec) in the 5 MHD models with magnetic confinement parmeters $\eta_* = 1/10$, $1/\sqrt{10}$, 1, $\sqrt{10}$, and 10. The horizontal dashed lines mark the unit values for the non-magnetic ($B = \eta_* = 0$) case.

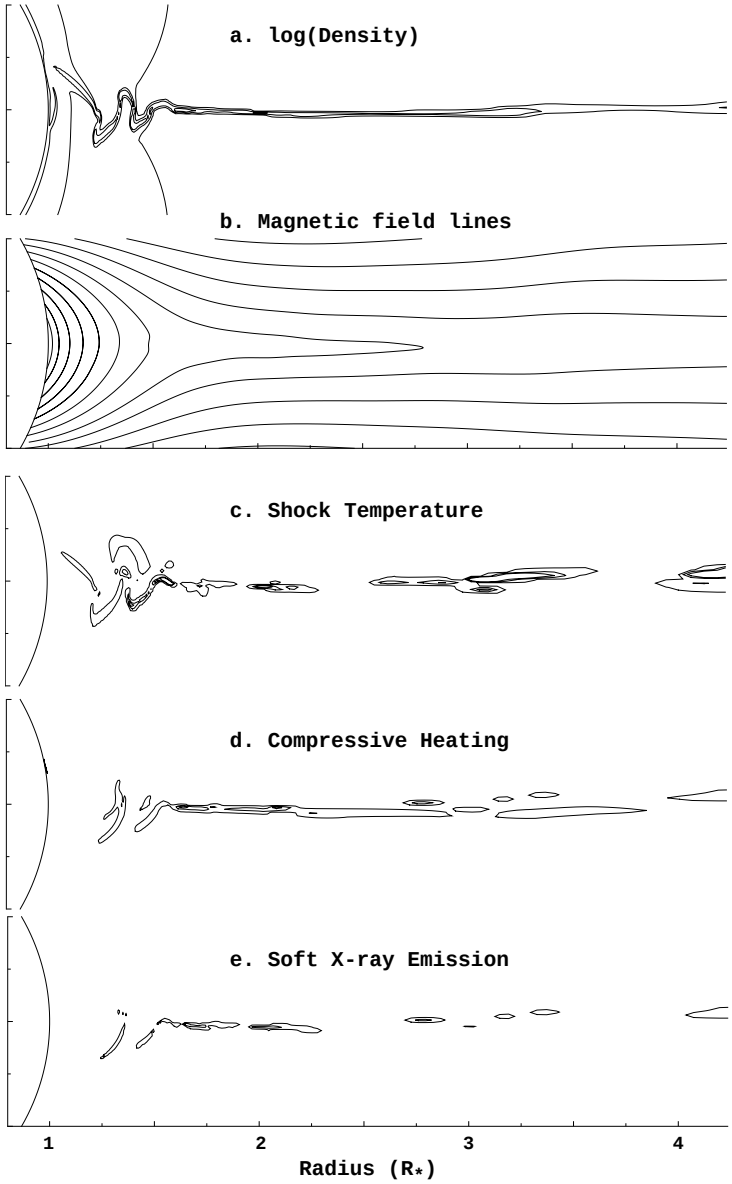

Figure 3.9: For the strong magnetic confinement case $\eta_* = 10$, contours of a. log(density), b. magnetic field lines, c. shock temperature [estimated from eqn. (3.11)], d. compressive heating [computed from eqn.(3.12)], and e. soft x-ray emission [estimated from eqn. (3.13), with $E =$ 0.1 keV]. The 3 contour levels correspond to $\log(\rho) =$ -12, -13, and -14 (g/cm^3) in panel a; to $T_s = 1$, 11, and 21 MK in panel (C); and to q (or q_E) of 0.15, 0.9, and 1.5 erg/cm^3/s in panels (d) and (e).

Chapter 4

THE EFFECT OF MAGNETIC FIELD TILT AND DIVERGENCE ON WIND MASS FLUX AND FLOW SPEEDS

4.1 Introduction

In chapter 3 we presented numerical magnetohydrodynamic (MHD) simulations of the effect of stellar dipole magnetic fields on line-driven wind outflows from hot, luminous stars. We showed that the overall degree of influence of the field on the the wind depends largely on a single, dimensionless, 'wind magnetic confinement parameter', η_* ($= B_{eq}^2 R_*^2/\dot{M}v_\infty$), which characterizes the ratio between magnetic field energy density and kinetic energy density of the wind. We showed that regardless of the strength of η_* the outer wind always wins over magnetic fields simply because the field energy declines faster than the wind kinetic energy. Thus, far away from the stellar surface the field lines are stretched out in a radial configuration. For weak confinement $\eta_* \leq 1$, the field is fully opened throughout the whole computational domain. But for stronger confinement $\eta_* > 1$, the magnetic field remains closed only over a limited range of latitude and height above the equatorial surface.

In this chapter we are concerned mostly with the open field region of the outer wind, far away from the stellar surface. We show that the wind flow is characterized by a faster-than-radial expansion that leads to a modest increase in terminal speeds

($< 30 - 40\%$ at the poles) compared to 1D non-magnetic case, consistent with observational constraints.

4.2 Motivation

This analysis has been motivated mainly by the work of MacGregor (1988) who argued that the faster-than-radial divergence of magnetic flux tubes can lead to substantial (3-4 fold) increase in terminal velocities of line-driven winds compared to that of the non-magnetic spherical case.

MacGregor's analysis extended previous studies of rapid areal divergence in the solar wind to the case of line-driven stellar winds. Notably, Kopp and Holzer (1976, hereafter KH) explored the case where the hydrodynamic properties of the expanding solar corona deviated significantly from spherically symmetric outflows in the sense that the geometrical cross-section of a magnetic flux tube increased with the distance r away from the sun faster-than-r^2 in the coronal hole region, which naturally lead to high speed and low density solar wind outflow from there. They chose a divergence function $f(r)$ such that $f(R_\odot) = 1$ and then increased smoothly to some maximum value f_{max}. The exact form of this function is given further below in §4.4.2.

MacGregor (1988) applied the KH model to line-driven hot-star winds and concluded that rapid divergence may lead to significantly higher speed winds. In this context, the lack of observational evidence of such high speed winds would imply absence of magnetic fields in hot stars in general. This would have been contrary to some recent positive detections of stellar magnetic fields in non-peculiar hot stars as we discussed in the previous chapter, (e.g. about 400 G dipole field in β *Cep* (Donati et al. 2001)).

On the other hand, our dynamical simulations of hot-star winds (chapter 3; ud-Doula and Owocki 2002) show that magnetic fields of order 1000 G in the prototypical O supergiant star ζ *Pup*, lead to a rather modest increase in stellar

wind speeds. To reconcile these seemingly contradictory results, we re-examine the MacGregor analysis, and find that omission of the so called *finite disk correction* factor in MacGregor's analysis was a key reason that lead to such high speed winds. In the analysis to follow, we show that the finite disk correction along with rapid divergence and mass flux as a function of latitude can explain the latitudinal modulation of hot-star winds found in our self-consistent MHD simulations. We also show that the mass flux along a flow tube tilted with respect to radial direction is reduced by the square of the cosine of the tilt angle.

4.3 1D CAK Wind

Let us first study the simple, radial 1D CAK wind, and how rapid divergence and finite disk correction affect such a flow. We then discuss what happens if the flow, guided by the magnetic flux tubes, is tilted by some angle with respect to the radial direction.

4.3.1 Simple, Radial Flow

We already discussed the simple, radial 1D CAK wind outflow in a point source approximation in §2.6. We showed that the equation of motion for a 1D CAK wind can be expressed as,

$$Cw^{\alpha} = w + 1 \tag{4.1}$$

where w is the acceleration in the unit of effective gravity and C is a constant that determines the mass loss rate. The solution of the above equation leads to the CAK maximal mass loss rate,

$$\dot{M}_{CAK} = \frac{L}{c^2}\,\frac{\alpha}{1-\alpha}\left[\frac{\bar{Q}\Gamma}{1-\Gamma}\right]^{(1-\alpha)/\alpha} \tag{4.2}$$

with the velocity law,

$$v(r) = v_{\infty}\left(1 - \frac{R_*}{r}\right)^{1/2}, \tag{4.3}$$

where, $v_\infty = \sqrt{\alpha/(1-\alpha)}v_{esc}$ is the terminal speed of the wind. This underestimates observed terminal velocities for most hot stars. In the next section we discuss an extension of this model that takes into account the finite size of the star for the calculation of the line-driving.

4.3.2 The Effect of Finite disk Correction Factor

A star cannot be treated as a point-like source in general, particularly near the surface. To account for the finite size of the star one has to include a *finite disk correction* factor (eqn 2.88; CAK eqn 50), f_d, which is a complicated function of radius, velocity and velocity gradient [see §2.7]. In 1D steady state CAK wind approximation, f_d enters the equation of motion through the line force term [see eqn 2.84]. Thus the eqn (4.1) can be rewritten as:

$$C f_d \, w^\alpha = w + 1. \tag{4.4}$$

This equation, in principle, can be solved for an arbitrary α. But for illustrative purposes in what follows we shall assume $\alpha = 1/2$ since this will allow us to obtain an analytical solution. Let us define $x \equiv \sqrt{w}$, then we have,

$$C f_d \, x = x^2 + 1. \tag{4.5}$$

This has two solutions:

$$x_\pm = \frac{C f_d \pm \sqrt{C^2 f_d^2 - 4}}{2} \tag{4.6}$$

Here the constant $C \sim 1/\dot{M}^\alpha$, still unknown, determines the mass loss rate. For high $\dot{M}$ or small C there are no solutions, while for small $\dot{M}$ or high C there are two solutions [see figure 2.6]. The critical solution lies in between these two, and corresponds to the maximal mass loss rate CAK solution. It requires that $C f_d \, w^\alpha$ curve intersect $1 + w$ line tangentially, i.e.,

$$C_c f_d^{critical} \, \alpha w^{\alpha - 1} = 1 \, . \tag{4.7}$$

In practice the value of f_d increases away from the stellar surface. It starts typically with $f_d \approx 1/(1+\alpha) \sim 2/3$ near the stellar surface, rises above unity around the isotropic expansion point, then finally approaches unity at large radii [see figure 2.7]. It is the minimum value of f_d that constrains the mass loss rate, so we can assume $f_d^{critical} = 1/(1+\alpha)$. Thus, using eqn (4.4) we get $C_c = (1+\alpha)/\left[\alpha^{\alpha}(1-\alpha)^{1-\alpha}\right]$. For $\alpha = 1/2$, we get $C_c = 3$ which now fixes the critical mass loss rate, $\dot{M}_{CAK}$. If we substitute the value of C_c in eqn (4.6), then we obtain

$$x_{\pm} = \frac{3f_d \pm \sqrt{9f_d^2 - 4}}{2}\,. \tag{4.8}$$

In order to find a unique solution to the above we have to resolve two key issues: the mass loss rate and the resultant terminal velocity. The maximal mass loss rate has already been assumed by requiring $C_c = 3$ for the special case of $\alpha = 1/2$ which implies a lower maximal mass loss rate than in the simpler wind flow case without the *finite disk correction* f_d.

Since the mass loss rate has been determined, the terminal velocity of the wind can be estimated. As mentioned earlier, f_d varies with the distance r. The wind at higher radii experiences more radial photons, and a higher value of f_d. This can lead to a stronger acceleration of the wind far away from the stellar surface. This can be easily demonstrated by setting the asymptotic value $f_d = 1$ in equation 4.8 which leads to the solution $w_+^c = x_+^2 = [(3+\sqrt{5})/2]^2 \approx 7$ and $w_-^c = x_-^2 \approx 0.75$. The value of $x_{\pm}$ above is a measure of how much acceleration is available to the outer wind compared to the effective gravity; it also represents two families of 'shallow' (x_-) and 'steep' (x_+) solutions available to the 1D CAK wind. None of these two families can provide a global solution for the wind (Feldmeier and Shlosman 2000). The shallow solution does not reach the infinity, while the steep solution fails to converge to low subsonic speeds at the stellar atmosphere. The critical CAK wind starts with the shallow solution at the subsonic part of the wind, and then switches to a steep one. Thus the wind adopts the steep x_+ solution in the outer region.

Since x_+^2 is directly proportional to acceleration, x_+ can be related directly to the terminal velocity obtained by the wind. For the CAK wind without the finite disk correction and with $\alpha = 1/2$, we get $x_+ = x_- = 1$ implying, as we showed in §2.6, a terminal velocity equal to the escape speed. In this case of the CAK wind with the finite disk correction, the outer wind gets an extra 'leveraging' (Gayley 2000) due to enhanced acceleration that can lead to terminal velocities ~ 3 times the escape speed, measured by x_+. So, the net result of the finite disk correction is to lower the mass loss rate and accelerate the wind to higher terminal speeds.

For the more general case with $0 < \alpha < 1$, f_d lowers the mass loss rate by typically a factor of about two and increases the terminal velocity by a factor of 2-3 compared to CAK wind solution without the finite disk correction (Pauldrach, Puls, & Kudritzki 1985; Friend & Abbott 1985).

4.3.3 The Effect of Rapid Divergence on Mass Loss

4.3.3.1 Definition

Let us first define an areal divergence factor, f. Suppose a magnetic flow tube has a cross-sectional area A_1 at radius R_*, and A_2 at another radius r. The flux tube is not necessarily radial, and the areal divergence factor can be a function of latitude and radius, $f = f(r, \theta)$. Taking into consideration that the area for a fixed solid angle increases as r^2, we can define

$$f(r, \theta) \equiv \frac{A_2}{A_1} \frac{R_*^2}{r^2} \tag{4.9}$$

Since the divergence of magnetic field is zero,

$$\nabla \cdot \mathbf{B} = 0, \tag{4.10}$$

the magnetic flux through A_1 and A_2 must be equal, i.e.

$$B_*(R_*, \theta_{min}) A_1 = B(r, \theta_{max}) A_2 \,, \tag{4.11}$$

where θ_{min} and θ_{max} are the latitudes of the flux tube at R_* and r respectively. Thus the definition of f becomes:

$$f(r,\theta) \equiv \frac{B_*(R_*,\theta_{min})R_*^2}{B(r,\theta_{max})\,r^2}\,. \tag{4.12}$$

4.3.3.2 The Role of Rapid Divergence in Wind Flow

The role of the rapid divergence factor, f, is to dilute the flow and increase its velocity. It can be incorporated into the momentum equation (2.68) through the conservation of mass:

$$\rho = \frac{\dot{M}}{4\pi r^2 f v}\,. \tag{4.13}$$

Thus eqn 4.1 becomes:

$$C f^{\alpha} w^{\alpha} = w + 1 \tag{4.14}$$

The form of the above equation is very similar to what was derived in §4.3.2 in the analysis of the finite disk correction (f_d) effects, but with f now raised to the α power. Since the critical solution occurs near the stellar surface where by definition $f = 1$, the solution, at the base, is similar to 1D CAK wind solution in the point-star approximation with $C_c = 2$ for the special case of $\alpha = 1/2$. This implies that the maximal mass loss rates are similar as well. However, because the rapid divergence factor f may vary with the distance r, this new wind solution will differ from the 1D CAK case far away from the stellar surface. The two possible solutions [see eqn (4.6)] are:

$$x_{\pm} = (f/2)^{1/2} \pm \sqrt{f-1} \tag{4.15}$$

Even for the modest value of $f = 2$, the '+' solution adopted by the wind, $w_+ = x^2$ is equal to 4. This implies that the acceleration of the outer wind is four times that of the effective gravity, which naturally may lead to high terminal speeds, a few times v_{esc}. We conclude from this analysis that rapid divergence, if acting independently, does not change the maximal mass loss rate, but increases the terminal velocities of the wind significantly.

This is essentially what MacGregor (1988) concluded in his analysis where he considered the effect of rapid divergence alone, ignoring the finite size of the star. As we shall see next, this is a key reason he obtained terminal speeds as high as three times that of CAK wind in the point-star approximation.

4.3.4 Combined Effect of Finite Disk and Rapid Divergence

In this section we examine the combined effects of the finite size of a star and the faster-than-radial divergence of the magnetic flux tubes on the wind flow. Taking into account these two factors, the eqn (4.1) becomes:

$$C f_d f^\alpha w^\alpha = w + 1\,. \tag{4.16}$$

Near the surface of the star $f \approx 1$ by definition, while, as we argued earlier, $f_d \approx 1/(1+\alpha)$. Therefore, the value of C_c remains unchanged compared to the CAK solution with finite disk correction alone implying the same maximal mass loss rate.

For our sample case with $\alpha = 1/2$, eqn (4.6) becomes:

$$x_\pm = \frac{3 f_d f^\alpha \pm \sqrt{9 f_d^2 f^{2\alpha} - 4}}{2} \tag{4.17}$$

$$= \frac{3 f_d f^{1/2} \pm \sqrt{9 f_d^2 f - 4}}{2}$$

$$= \frac{f_d \sqrt{f}}{2}\left(3 \pm \sqrt{9 - \frac{4}{f_d^2 f}}\right)\,. \tag{4.18}$$

This corresponds to the $x_+ = 4$ or $w_+ \approx 16$ solution in the outer wind for a modest value of $f = 2$! This kind of leveraging will naturally lead to high terminal speeds, as high as 4 times the escape speed.

Relative to the case *without* the finite disk correction factor, these terminal speeds are very high. On the other other hand, if we compare the very same terminal speeds with the case *with* the finite disk correction factor, the relative change is rather modest, of order only $(4-3)/3 = 33\%$. The reason for this is that the finite

disk correction alone makes the wind very fast, and although an additional rapid divergence factor f makes it even faster, the relative change is small.

4.3.5 Mass Loss for tilted flow

In this section we examine how the mass loss rate is affected if the flow is tilted with respect to the normal to the stellar surface. We assume that the magnetic flux tube that guides the wind flow is tilted by an angle θ with respect to the radial direction. For simplicity let us assume that the flow is planar and there is no horizontal dependence of the flow. We define vertical direction to be in the z-direction, with $\hat{\mathbf{z}}$ the unit vector. Because in the limit of infinite conductivity, a fluid parcel is tied to the field line, the velocity $\mathbf{v} = v_s\hat{\mathbf{s}}$, where $\hat{\mathbf{s}}$ is the unit vector along the field (flow) line. We also define $\hat{\mathbf{z}} \cdot \hat{\mathbf{s}} = \cos\theta \equiv \mu$. This implies that $\hat{\mathbf{s}} = \mu\,\hat{\mathbf{z}} + \sqrt{1-\mu^2}\,\hat{\mathbf{x}}$, with the horizontal unit vector $\hat{\mathbf{x}}$ perpendicular to the vertical direction.

In general, the advective derivative of velocity along an arbitrary direction $\hat{\mathbf{s}}$ can be expressed as:

$$\begin{aligned}(\mathbf{v}\cdot\nabla)(\mathbf{v}\cdot\hat{\mathbf{s}}) &= v_s(\hat{\mathbf{s}}\cdot\nabla)(\mathbf{v_s}) \\ &= \mu\, v_s\frac{\partial v_s}{\partial z} + \sqrt{1-\mu^2}\frac{\partial v_s}{\partial x} \\ &= \mu\, v_s\frac{\partial v_s}{\partial z}\,, \end{aligned} \tag{4.19}$$

where the last expression assumes that there is no variation in velocity in the horizontal direction, so that $\partial v_s/\partial x = 0$. The momentum equation (2.68) along **ds** becomes:

$$(\mathbf{v}\cdot\nabla)(\mathbf{v}\cdot\hat{\mathbf{s}}) = -(1-\Gamma)\frac{GM}{r^2}(\hat{\mathbf{z}}\cdot\hat{\mathbf{s}}) \;+\; \frac{\bar{Q}\kappa_e F}{c}\,(\hat{\mathbf{z}}\cdot\hat{\mathbf{s}})\frac{1}{1-\alpha}\left[\frac{\hat{\mathbf{z}}\cdot\nabla[\hat{\mathbf{z}}\cdot\mathbf{v}]}{\bar{Q}\kappa_e\rho c}\right]^{\alpha}, \tag{4.20}$$

with the radius $r = \sqrt{z^2+x^2}$. The LHS represents the inertia along **ds**, and the RHS represents *real* forces acting on the fluid parcel. Note that in the optical depth

part of the line force $\hat{\mathbf{z}}$ represents the direction of the incoming photon, which by our assumption is purely radial or vertical in this case.

Equation (4.20) can be rewritten as:

$$\mu\, v_s \frac{\partial v_s}{\partial r} = -(1-\Gamma)\frac{GM}{r^2}\mu \;+\; \frac{\bar{Q}\kappa_e L}{4\pi r^2 c}\,\mu \frac{1}{1-\alpha}\left[\frac{\mu \partial v_s/\partial z}{\bar{Q}\kappa_e \rho c}\right]^{\alpha}. \tag{4.21}$$

If we use the mass loss rate along the tilted direction, $\dot{M}_s = 4\pi r^2 \rho v_s$ to replace the density ρ in the above equation, we have:

$$\mu\, v_s \frac{\partial v_s}{\partial z} = -(1-\Gamma)\frac{GM}{r^2}\mu \;+\; \frac{\bar{Q}\kappa_e L}{4\pi r^2 c}\,\mu \frac{1}{1-\alpha}\left[\frac{4\pi r^2 \mu v_s \partial v_s/\partial z}{\bar{Q}\kappa_e \dot{M}_s c}\right]^{\alpha}. \tag{4.22}$$

Now let us divide this by μ and use the definition

$$w \equiv \frac{r^2 v_s dv_s/dz}{GM(1-\Gamma)}\,. \tag{4.23}$$

Then the momentum equation equation can be recast in the form

$$w = -1 + C\mu^{\alpha} w^{\alpha}\,, \tag{4.24}$$

where C has been defined earlier (eqn 2.70) and is related to the maximal CAK mass loss rate. The equation (4.24) becomes mathematically identical to eqn (2.68) under the substitution $C' = C\,\mu^{\alpha}$. As such, if we further assume $\dot{M}_s = 4\pi r^2 \dot{m}_s$ with $\dot{m}_s = \rho v_s$, we obtain:

$$\dot{m}_s = \frac{F\mu}{c^2}\,\frac{\alpha}{1-\alpha}\left[\frac{\bar{Q}\Gamma}{1-\Gamma}\right]^{(\alpha-1)/\alpha} \tag{4.25}$$

where F is the radiation flux along **dz**. Clearly, the mass flux has been reduced by factor μ compared to that of a purely radial spherically symmetric outflow (eqn 4.2). Moreover, in terms of *radial* mass flux for these tilted tubes, the projection of **ds** onto **dz** will yield another factor μ, i.e.

$$\dot{m}_r = \mu^2 \dot{m}_{spherical}\,. \tag{4.26}$$

This has the consequence that, if we have a flow tube that is initially (near the stellar surface) inclined by angle $\cos^{-1}\mu$, then the mass flux through the tube will be reduced by factor μ^2 compared to the spherical non-magnetic flow. Such reduction in mass flux can lead to higher terminal speeds, as our dynamical simulations show.

4.4 Results

The right panel of figure 3.8 in chapter 3 shows wind flow speeds as a function of the cosine of the co-latitude, $\mu = \cos(\theta)$ for various values of η_* at the outer boundary of our computational domain, $R_{max} = 6R_*$ normalized by the values for the corresponding non-magnetic model. Note the clear variation of the flow speed as a function of the latitude. The relatively low flow speeds at the magnetic equator are the consequence of the enhanced density due to magnetic channeling of the wind material and the reduced line-force. Here we attempt to explain the cause of this latitudinal modulation of the wind flow. We emphasize that this is only a qualitative analysis and we do not expect to obtain a precise numerical agreement with the MHD results.

4.4.1 Open Field Region

Figure 4.1 shows the cosine of co-latitude of a fluid parcel that is initiated at the stellar surface at the co-latitude θ_{min} and leaves the outer boundary at θ_{max}. We find θ_{min} by fixing θ_{max} and tracing the fluid parcel back to its origin at the stellar surface, e.g. for a purely radial outflow $\theta_{min} = \theta_{max}$. This figure gives an estimate of how much bending or deviation from radial flow any given flux tube undergoes. As a secondary result, one can also estimate the size of the magnetic closure latitude, as defined in §3.3.2, from the sharp transition near $\mu_{max} = \cos\theta_{max} = 0$.

A question may arise whether our outer boundary at $R_{max} = 6R_*$ is far enough to provide an asymptotic value for μ_{max}. For the line-driven winds we study here, at radial distance $r = 6R_*$, the wind reaches nearly the terminal speed. In addition, as we argued in chapter 3, the wind always wins over magnetic fields and stretches the field lines into a nearly radial configuration. Thus we do not believe that moving the outer boundary further will affect μ_{max} in a significant way. The advantage of using μ_{max} as our independent variable, as we do in the subsequent plots in this chapter, is that it gets rid of most of the chaotic behavior of the wind

associated with the magnetically confined or the "closed field lines" wind region. This allows us to focus on the flow within the range of the open field region.

4.4.2 Rapid Areal Divergence Factors

In ideal MHD cases the field and flow lines are closely tied together, and as such the non-radial divergence of magnetic field lines represents the divergence of the flow as well. Figure 4.2 shows maximum such divergence factor $f_{max} = f(R_{max}, \theta_{max})$ plotted as a function of $\mu_{max} = \cos(\theta_{max})$ for various cases of η_* as noted in the caption.

Higher η_* yields higher f_{max} at the poles. Note that f_{max} decreases towards the magnetic equator. In equation 4.15 we showed that the 'leveraging' factor that is responsible for an enhanced flow speed in the outer wind is directly proportional to f or f_{max}. As such this latitudinal variation of f could be the key reason behind the latitudinal variation of wind flow speed for low η_* cases, as shown in figure 3.8. But this assertion fails to account for the higher speeds at midlatitudes for the strongest magnetic confinement $\eta_* = 10$ case. To explain this, we need to consider the latitudinal variation of mass flux density in addition to the variation of f, as we do in §4.4.3.

But let us first examine how the rapid divergence factor f varies as a function of radius r. Specifically, we focus on the ray along the poles and compute $f_{pole} = f(r, \theta = 0)$ as a sample case for illustrative purposes. Figure 4.3 shows f_{pole} computed from our dynamical MHD simulations for all the five cases.

It is worthwhile to compare these dynamically obtained divergence factors to the divergence assumed by MacGregor (1988), which was based on a heuristic form introduced originally by Kopp and Holzer (1976) in the solar wind context

$$f(r) = \frac{f_{max} \exp[(r - R_1)/\sigma] + 1 - (f_{max} - 1) \exp[(R_* - R_1)/\sigma]}{\exp[(r - R_1)/\sigma] + 1} \,. \tag{4.27}$$

Specifically, this analysis assumed that the rapid divergence would be confined to a quite narrow range of radius ($\sigma = 0.1R_*$) centered on some radius ($R_1 = 1.25 - 2.5\,R_*$) distinctly above the stellar surface radius R_*. By comparison, our dynamical simulations indicate the divergence is generally most rapid right at the wind base near the stellar surface (implying $R_1 \approx R_*$), and extends over a quite large radial range (i.e., $\sigma > 1R_*$). MacGregor (1988) assumed values of the asymptotic net divergence, $f_{max} = 1.25 - 2.0$, that are quite comparable to the divergence factors found at the outer boundary of our MHD simulation models, $f_{pole}(R_{max}) = 1.25{-}2.5$.

4.4.3 Mass Flux at the Stellar Surface

In this section we study how the mass flux density, $\dot{m} = \rho v_r$ varies in our simulations as a function of colatitude at the stellar surface. Figure 4.4 shows $\dot{m}$ at R_{min} along the magnetic flux tubes plotted versus μ_{max} for the five MHD cases we presented in chapter 3. For all the cases, mass flux density declines from the poles towards the magnetic equator. This is a direct consequence of the tilt of the magnetic flux tubes at the base that the wind flow follows, as we show below. Note, however, that the polar value of mass flux is enhanced compared to the non-magnetic spherical wind. This enhancement is proportional to η_* or correspondingly to the magnetic field strength. The reason behind this polar enhancement of mass flux is not clear at this stage of our research, and will require further investigation. We recover the limit of a spherical wind for the model with the weak magnetic confinement $\eta_* = 0.01$.

Figure 4.5 shows the ratio $B_r/B = \mu$ which defines the tilt angle θ for the wind flow at the base, plotted again as a function of μ_{max}. For a pure dipolar field case, the initial state of our MHD models here, these curves are purely sinusoidal, but because we compute our models self-consistently, the wind modifies the field. The comparison between the overall shapes of these curves to those of the mass flux

densities reveals a clear similarity suggesting a close relationship between them; we show below that this indeed is the case.

In §4.3.5, we argued that the mass flux density $\dot{m}(R_*, \theta) \propto \mu^2$. This reflects the fact that although both gravity and photon flux are reduced along the tilted direction, **ds**, the nonlinear nature of the line force lowers the mass flux density. To verify this, in figure 4.6 we plot mass flux density scaled by μ^2. Unlike in figure 4.4 where the mass flux density varied by as much as 30-40 % from its polar value, $\dot{m}/\mu^2$ here varies by only a few percent at the most, with the maximum variation occurring near the equatorial region where the wind can behave rather chaotically, as was shown in chapter 3.

4.5 Discussion

Based on the solar analogy, MacGregor (1988) analyzed the effect of rapid divergence f, as defined in equation 4.27, on a line-driven stellar wind, assuming a simple 1D, radially oriented flow tube, as expected near the polar axis of an open magnetic field. He concluded that, because the line-driving acceleration scales inversely with density [$g_{lines} \sim 1/\rho^{\alpha}$; see eqn. (3.5)], the lower density associated with faster divergence would lead to substantially faster terminal speeds, up to a *factor three faster* than in a spherical wind, for quite reasonable values of the assumed flow divergence parameters. By comparison, the polar flow speed increases found in our full MHD models here are much more modest, about 30-40% in even the strongest field case, $\eta_* = 10$.

As was pointed out in §4.4.2, there are some differences between the assumed functional form and our calculated divergence function (along polar axes). These detailed differences in radial divergence do have some effect on the overall wind acceleration, and thus on the asymptotic flow speed. But it appears that a key reason behind the MacGregor (1988) prediction of a very strong speed enhancement was the neglect of the finite-disk correction factor for the line-force (Friend and

Abbott 1986; Pauldrach, Puls, and Kudritzki 1986). With this factor included, and using the MHD simulations to define both the divergence and radial tilt-angle of the field and flow, we show that a simple flow-tube analysis is able to explain fairly well our numerical simulation results for not only the polar speed, but also for the latitudinal scaling of both the speed and mass flux. In particular, we find that the even stronger increase in flow speed seen at mid-latitudes ($1/4 < |\mu| < 3/4$) in the strongest field model ($\eta_* = 10$) does not reflect any stronger divergence factor, but rather is largely a consequence of a *reduced* base mass flux associated with a non-radial tilt of the source flow near the stellar surface. As the flow becomes nearly radial somewhat above the wind base, the lower density associated with the lower mass flux implies a stronger line-acceleration and thus a faster terminal speed along these mid-latitude flow tubes.

4.5.1 Rapid Areal Divergence vs Finite Disk Correction in Enhancement of Flow Speed

In §4.3.2 we noted that the solution adopted by the wind $x_+ \propto v_\infty$. In this section, we compare the wind solution (x_+) with only finite disk correction included to the wind solution that includes the combined effect of both finite disk correction and rapid divergence, and show that the relative differences are comparatively small.

Let us first define a quantity ζ, that is an estimate of the relative change in terminal speeds for these two cases:

$$\zeta \equiv \frac{x_+^r(\theta_{max})}{x_+^{fd}} \tag{4.28}$$

where x_+^{fd} is the solution for the case with f_d alone, whereas x_+^r includes rapid divergence $f_{max}(\theta_{max})$ as well. For each value of μ_{max} we compute f_{max} then solve for x_+ using equation (4.18) under the assumption that far away the finite disk correction factor $f_d \approx 1$. Note that x_+^{fd} corresponds to the non-magnetic spherical wind, i.e. $f_{max} = 1$.

Figure 4.7 plots ζ versus μ_{max} representing the ratio between the modified flow speed to the non-magnetic spherical wind case. These plots overestimate the flow speed at the poles while underestimating it at the midlatitudes, which is the most apparent for the case with the highest magnetic confinement $\eta_* = 10$ case.

This can be explained by considering the mass flux density variation as a function of latitude at the base. As mentioned earlier, the polar mass flux density for magnetic cases is enhanced compared to the non-magnetic case, while it is reduced for tilted flows at the midlatitudes. This altered mass flux changes the effective f_{max}, and we can redefine a modified divergence factor:

$$f_{mod}(\theta_{max}) = f_{max}(\theta_{max}) \frac{\dot{m}_r^{spherical}}{\dot{m}_r(R_*, \theta_{min})} \tag{4.29}$$

where $\dot{m}_r^{spherical}$ is the mass flux for the non-magnetic case. With divergence factor thus modified, we recalculate ζ, and plot this in figure 4.8.

The agreement with the dynamical MHD results now is significantly better. The polar values of the wind flow agree within a few percent, and also, at least qualitatively, higher midlatitudinal flow speeds for the η_* case are accounted for. Here, we made a number of simple assumptions, e.g. we assumed f_{max} to be constant throughout the wind. In practice f varies with the distance r which may influence the flow speed in a way that we did not consider here.

4.6 Conclusion

In this chapter, we analyzed the role of *faster-than-r^2* divergence of field and finite disk correction factor in accelerating line-driven winds to high speeds. Our conclusions are summarized below:

1. The finite disk correction alone can increase the terminal speed of the line-driven wind by a factor 2-3.

2. The mass flux rate for a tilted flow is reduced by the square of the cosine of the tilt-angle (μ^2) with respect to the radial outflow.

3. The divergence function obtained from our numerical MHD models differ from the heuristic form used by Kopp and Holzer (1976). Our computed area functions are most-rapid right at the wind base and extend over a quite large radial distance. But the net divergence assumed by MacGregor ($f_{max} = 1.25 - 2.0$) is comparable to the divergence factors found at the outer boundary of our simulations ($f_{max} = 1.25 - 2.5$)

4. The high speed winds obtained by MacGregor's (1988) analysis of rapid areal divergence function applied to line-driven winds was mainly due to neglect of the finite disk correction. We showed that once this factor is included, the wind reaches high speeds, and the addition of rapid divergence makes *relatively* small impact. Our numerical results show a modest increase in flow speeds at the outer boundary, of only 30-40 %. This modest level of wind velocity modulation is much more in concert with observed blue edges of absorption troughs in UV wind lines from hot stars.

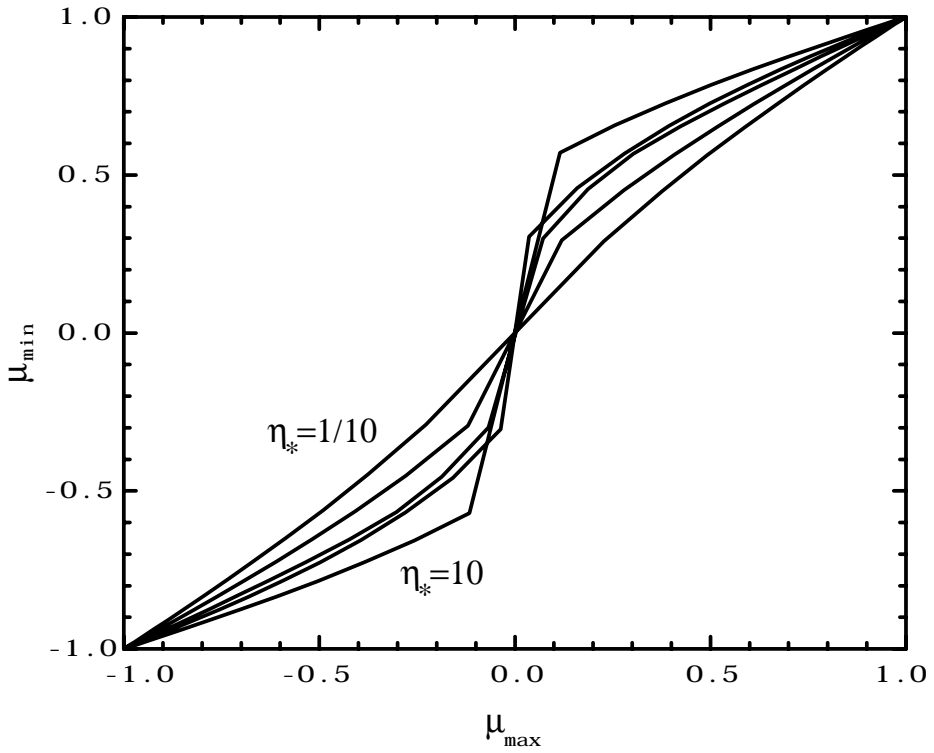

Figure 4.1: The measure of how much a magnetic flux tube diverges from radial configuration expressed through $\mu_{min} = \theta_{min}$ and $\mu_{max} = \theta_{max}$. For a given μ_{max} flow tube is traced back to the stellar surface, and μ_{min} is found. The five lines represent the five MHD models discussed in the text, $\eta_* = 10, \sqrt{10}, 1, 1/\sqrt{10}$ and $1/10$ with the uppermost curve corresponding to $\eta_* = 10$ and the lowermost to $\eta_* = 1/10$ cases, the intermediate cases are in between in the above order. For a purely radial configuration the corresponding curve is a diagonal.

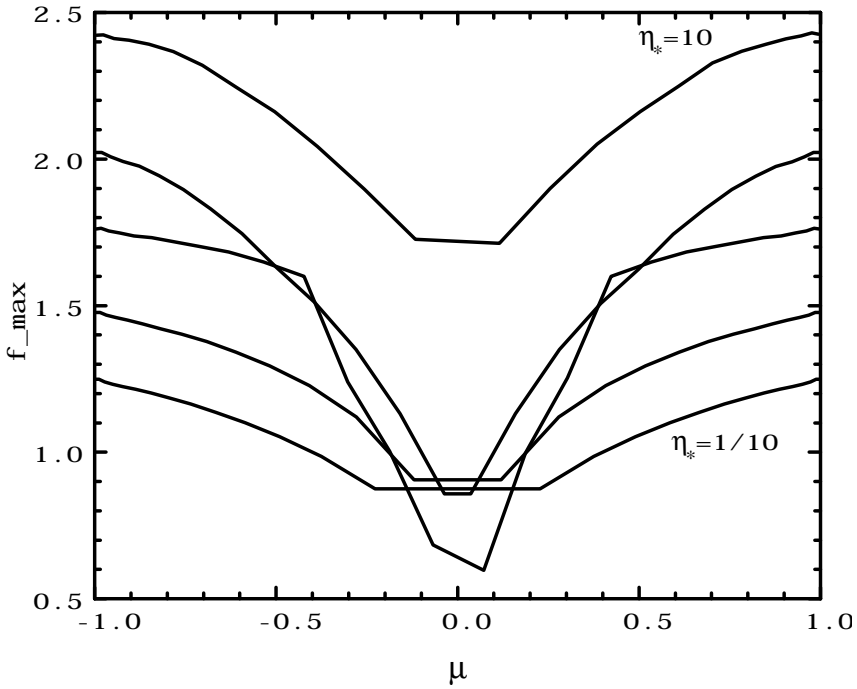

Figure 4.2: Rapid divergence f_{max} plotted vs μ_{max} for five MHD cases with, $\eta_* = 10, \sqrt{10}, 1, 1/\sqrt{10}, 1/10$ from top to bottom. Note that the highest values occur along the poles.

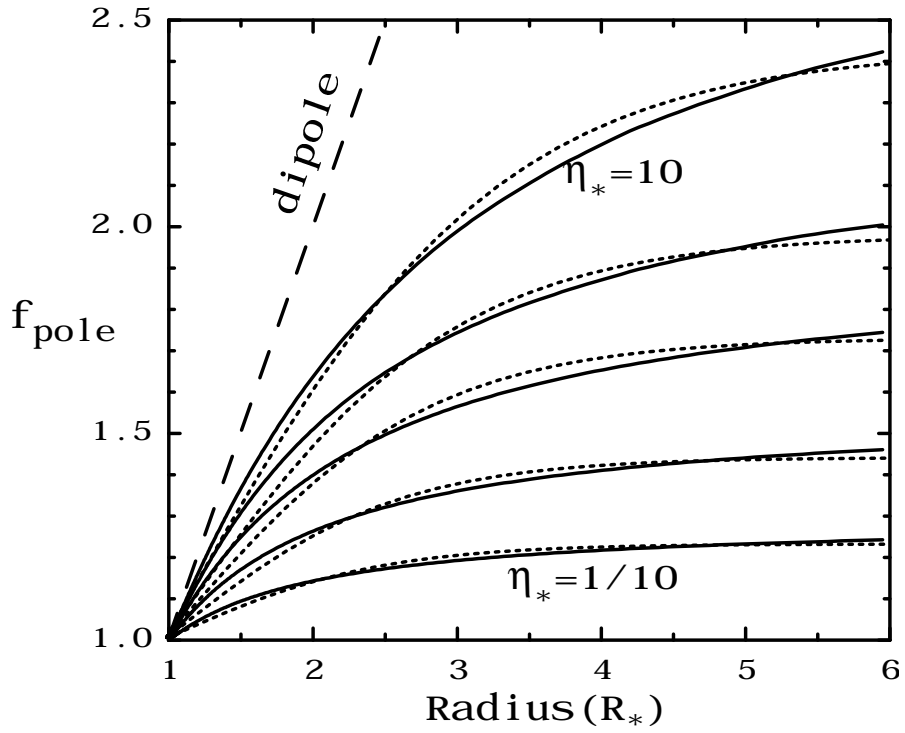

Figure 4.3: The measure of faster-than-r^2 decline of the polar magnetic field, as represented by the function f_{pole} defined in eqn. (3.10), and applied to the 5 MHD simulations with magnetic confinement ranging from strong ($\eta_* = 10$; uppermost curve) to weak ($\eta_* = 10$; lowermost curve). For the ideal MHD cases here of field-frozen flow, this also represents the degree of faster-than-r^2 expansion of flow tube area. The dotted curves plot the heuristic area-expansion function defined by Kopp and Holzer [eqn. (4.27) here], with $R_1 = 1\ R_*$, and the parameters $f_{max} = 2.43$, 1.98, 1.73, 1.44 and 1.23, and $\sigma/R_* = 1.13$, 0.98, 0.89, 0.79, and 0.73, chosen to best fit to the five cases from η_* =10 to 1/10. The dashed curve shows the variation for a pure dipole field.

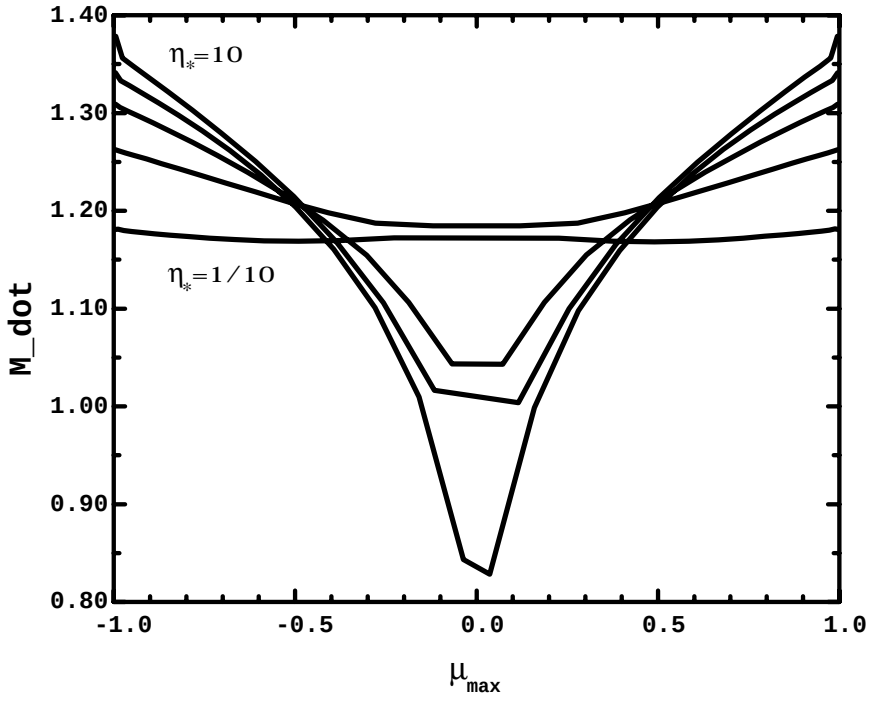

Figure 4.4: The mass flux density, $\dot{m} = \rho v_r$ normalized by the corresponding non-magnetic value at R_{min} plotted against μ_{max} for the five MHD models with magnetic confinement parameters $\eta_* = 1/10, 1/\sqrt{10}, 1, \sqrt{10}$ and 10. For the non-magnetic spherical wind case $\dot{m} = 1$.

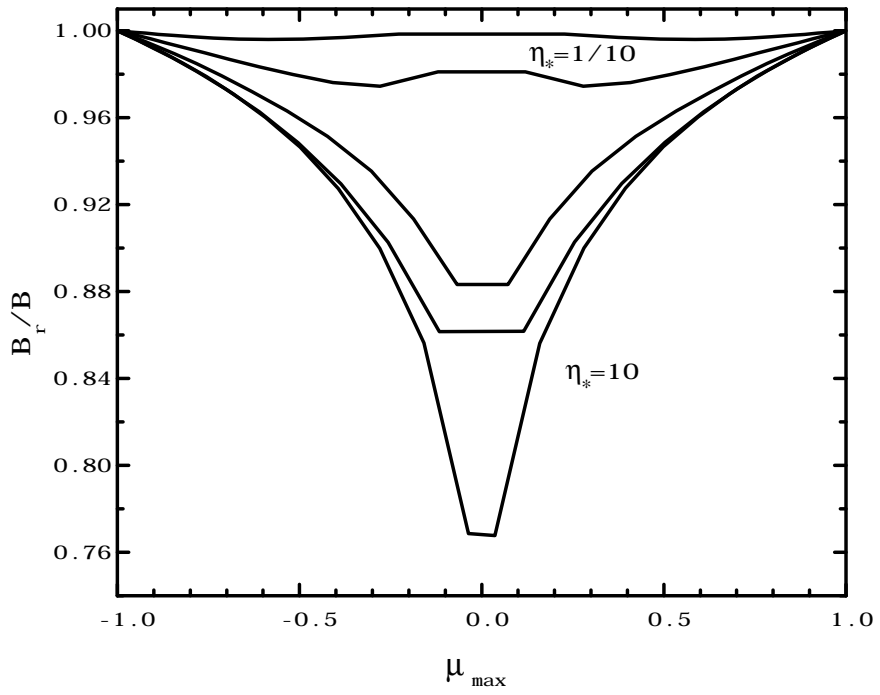

Figure 4.5: The ratio of B_r/B which represents the *cosine* of tilt angle, μ for a flow tube emanating from the stellar surface plotted as a function of μ_{max}. Five curves, starting from the uppermost, represent the five MHD models with magnetic confinement parameters $\eta_* = 1/10, 1/\sqrt{10}, 1, \sqrt{10}$ and 10 respectively.

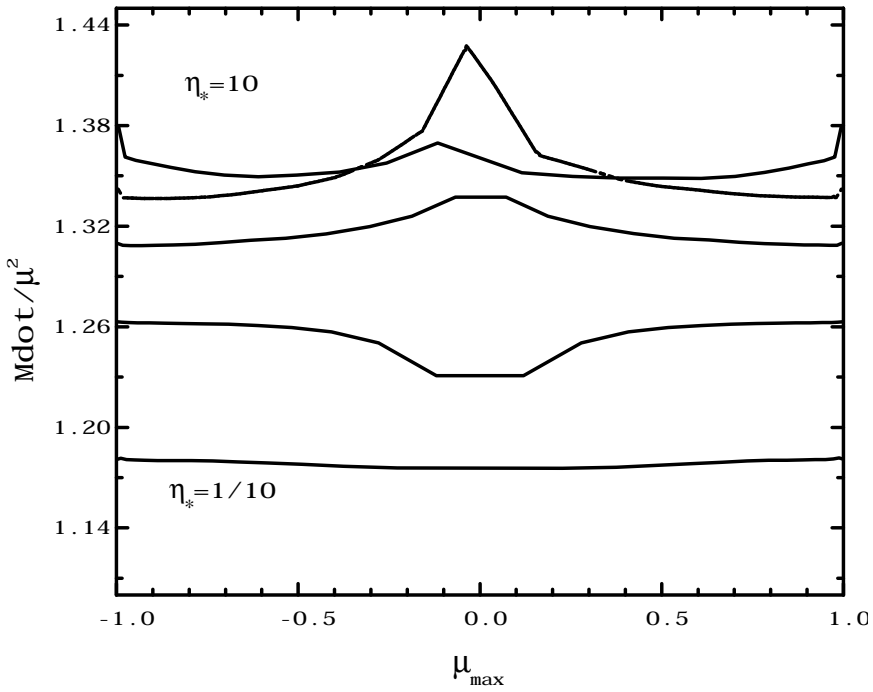

Figure 4.6: The mass flux density scaled by μ^2 for the five MHD models with magnetic confinement parameters $\eta_* = 1/10, 1/sqrt10, 1, \sqrt{10}$ and 10. Note that these are essentially constants, consistent with the claim that $\dot{m}_r \sim \mu^2$ for a flow tilted by angle $\cos^{-1}(\mu)$ from the radial flow.

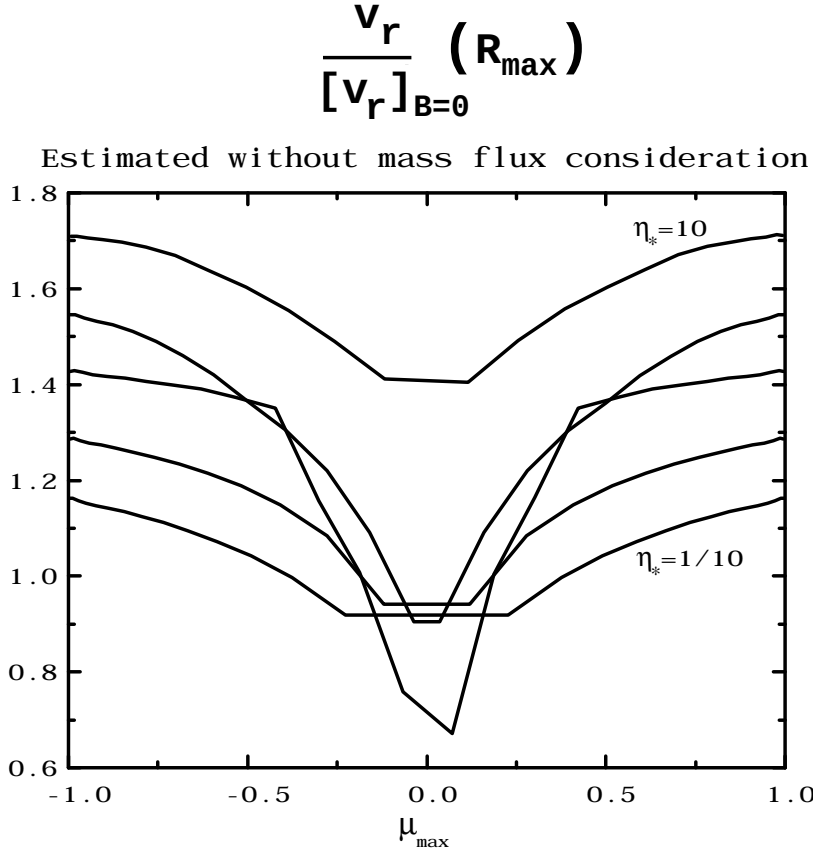

Figure 4.7: Predicted radial flow speed at $R_{max} = 6R_*$ scaled by the value for the non-magnetic spherical wind case based on simple consideration of only rapid divergence factor f_{max} for various cases of η_*. Note that because the mass flux density is higher at the poles compared to the spherical case, this prediction overestimates (since it is using lower mass flux than it should). Likewise, the midlatitudinal flow speeds are underestimated since they are using higher mass flux then they should. See figure 4.4.

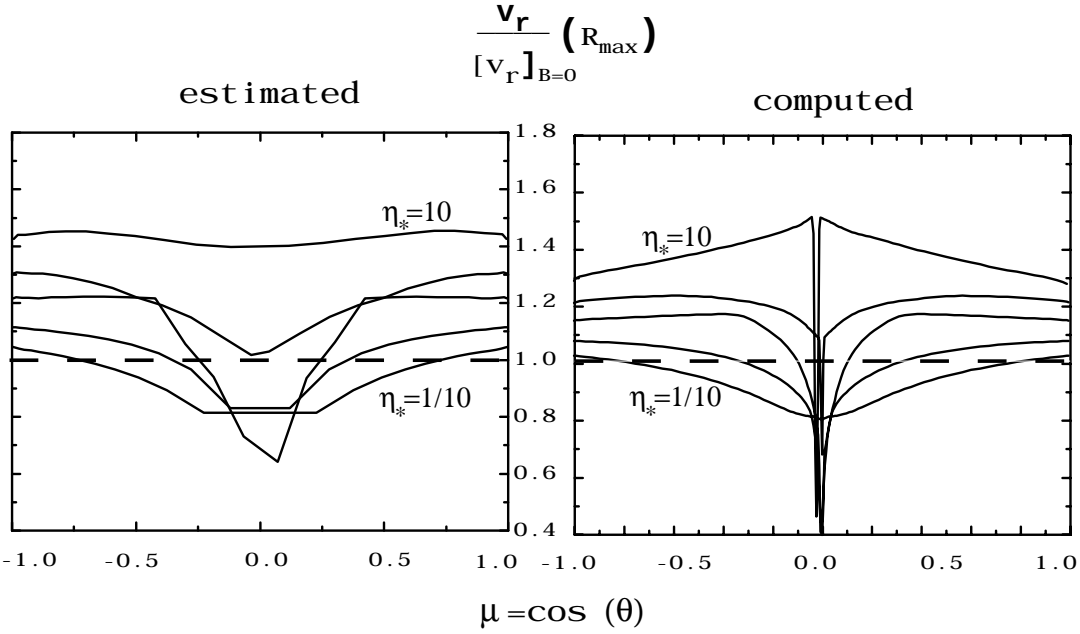

Figure 4.8: Predicted radial flow speed at $R_{max} = 6R_*$ scaled by the value for the non-magnetic spherical wind case based on consideration of *both* f_{max} and $\dot{m}(R_{min}, \mu_{max})$ for various η_* cases. Dashed line represents the non-magnetic model. Note that flow speeds are now in much better agreement.

Chapter 5

THE EFFECTS OF FIELD-ALIGNED ROTATION ON THE MAGNETICALLY CHANNELED LINE-DRIVEN WINDS

In the previous two chapters (3 & 4), we discussed how the surface magnetic fields can affect the line-driven winds of a star with no rotation. We showed that the degree to which the wind is influenced by the magnetic fields depends largely on a dimensionless, 'wind magnetic confinement parameter', η_*.

Here, we examine how the stellar rotation can affect such winds. As a first attempt, we assume that the rotation is aligned with the axis of the magnetic field. Rotation that is tilted with respect to the field axis, requires a full 3-D treatment, which is beyond the scope of this thesis and is left for future study.

5.1 Introduction

It is well known that the hot stars are rapid rotators. Numerous spectroscopic studies (e.g. Conti and Ebbets 1977; Fukuda 1982) indicate that normal OB-type stars are characterized by typical rotational velocities in excess of 100 km/s, and some are observed to have projected rotational speeds of upto 400 km/s.

Hydrodynamical calculations suggest that the terminal velocities of line-driven winds should decrease with the increase of rotational velocities (Castor 1979; Friend & Abbott 1986). The centrifugal force reduces the effective gravity, which

increases the mass loss rate; since the same luminosity drives the denser wind, the terminal velocity is reduced.

The radiation force is an efficient mechanism to lift the stellar material off the surface, but it is not efficient in providing angular momentum to that material. In the context Be stars, defined as very rapidly rotating (possibly close to critical rotation) main-sequence B stars which have shown Hα emission at least once in their lifetimes, Bjorkman & Cassinelli (1993) proposed a Wind Compressed Disk (WCD) model, wherein conservation of angular momentum tends to focus the wind material into a density enhanced disk-like equatorial region. However, dynamical simulations of Owocki et. al. (1994) showed that the material from the rotating star lacks the necessary angular momentum to form a stable Keplerian orbit that would define a disk. Instead, the material flows through the WCD, with the inner portion falling back onto the star while the outer portion flows out as an equatorial wind. This scenario is contrary to the observed dense, nearly stationary Keplerian disks (Hanuschik 1996; Hummel 1998; Rivinius et al. 2001) inferred from the optical and IR emission lines as well as the IR continuum excess of Be stars due to gaseous cool disk (Waters & Marlborough 1994).

An efficient mechanism to impart angular momentum to outflowing material is the moment arm of a stellar magnetic field. There have previously been attempts to model magnetic field effects on line-driven winds of rotating hot-stars. Friend and MacGregor (1984) extended the model of Weber and Davis (1967, discussed in chapter 2) to line-driven CAK winds to study how a monopolar base magnetic field at the surface of a rotating star can affect the rotational properties of the equatorial material outflow. Just as in the solar wind case, they found that the magnetic fields can spin up the hot-star wind, but they did not discuss this in the context of formation of a disk.

Recently, Cassinelli et al. (2002, in press) proposed a magnetically torqued

disk model for Be stars wherein they prescribe an azimuthal velocity of the flow as a function of radius, $v_\phi(r)$ and from that they estimate the strength of the stellar surface magnetic field necessary to create a disk. In our models we calculate the azimuthal velocity self-consistently, but fix the surface magnetic field. As discussed earlier in chapter 3, our 2D dynamical simulations of line-driven winds from hot-stars with a dipolar surface magnetic fields, showed that if the field is strong enough (measured by η_*), magnetic field lines channel the wind outflow toward a collision at the top of a closed loop, leading to a density-enhanced equatorial region. Now we wish to investigate what happens to these regions when stellar rotation is taken into account.

5.2 Method

5.2.1 Oblateness due to Rotation

Let us first examine the effects of rotation on the shape of the star itself, and show that, for the range of rotation rates used for our models here, stellar deformation is relatively unimportant.

For a uniformly rotating star, the gravitational potential can be approximated by,

$$\Phi(r,\theta) = -\frac{GM_*}{r} - \frac{1}{2}\Omega^2 r^2 \sin^2\theta\,, \tag{5.1}$$

where Ω is the angular speed of the star. In particular, for the polar radius, $r = R_p$, we can write,

$$-\frac{GM_*}{R_p} = -\frac{GM_*}{R_*} - \frac{1}{2}\Omega^2 R_*^2 \sin^2\theta\,, \tag{5.2}$$

with $R_* = R_*(\theta)$ defining the stellar surface. This can be solved once R_p and the stellar angular speed Ω are specified.

Let us now compare R_p with $R_*(90^o) = R_e$ as a function of Ω. After dividing both sides by $-GM_*/R_*$ the above equation (5.2) can be rewritten as,

$$\frac{R_e}{R_p} = 1 + \left(\frac{1}{2}\Omega^2 R_*^2\right) / \left(\frac{GM_*}{R_*}\right)\,. \tag{5.3}$$

This can be simplified if we define a "critical" (or "break-up"- a misnomer but often used in the literature), angular velocity Ω_c at the equator such that the centrifugal force balances the gravity, i.e. $\Omega_c = \sqrt{(2GM_*/R_e)}$,

$$\frac{R_e}{R_p} = 1 + \frac{1}{2}\frac{\Omega^2}{\Omega_c^2}\,. \tag{5.4}$$

For a star that is rotating with half of the critical rotation, the equatorial radius is only 12.5 % larger than the polar radius, i.e. if $\Omega = 0.5\ \Omega_c$ then $R_e/R_p = 1.125$. Throughout this work we will assume $\Omega \leq 0.5\ \Omega_c$ and ignore the modest effect of this oblateness.

In addition, for simplicity we ignore any effect of gravity darkening (von Zeipel 1924) which would reduce the radiation flux at the equator relative to the pole.

5.2.2 Equations of Magnetohydrodynamics

Our approach here is to increase the level of complexity of physics from that of the previous chapter by adding rotation in the formulation of our problem. We, again, use the numerical code ZEUS-3D to evolve a self-consistent dynamical solution for a line-driven wind from a hot star with a dipolar surface field, but now include rotation that is aligned with the axis of the magnetic field. We run our code in spherical polar coordinates with radius, r, co-latitude θ, and azimuth ϕ. We assume all the quantities are constant in azimuthal angle ϕ, but within a 2.5-D formulation include the rotational velocity v_ϕ and the azimuthal magnetic field B_ϕ.

As in the previous chapters, the time-dependent equations to integrate include the conservation of mass,

$$\frac{D\rho}{Dt} + \rho\nabla\cdot\mathbf{v} = 0\,, \tag{5.5}$$

where ρ, and $\mathbf{v}$ are the usual mass density, and velocity of the fluid flow, and $D/Dt = \partial/\partial t + \mathbf{v}\cdot\nabla$ is the advective time derivative. The equation of motion

now includes the centrifugal and Coriolis forces that arise essentially from geometric considerations,

$$\rho\left[\frac{D\mathbf{v}}{Dt}+2\mathbf{\Omega}\times\mathbf{v}+\mathbf{\Omega}\times(\mathbf{\Omega}\times\mathbf{r})\right]=-\nabla p+\frac{1}{4\pi}(\nabla\times\mathbf{B})\times\mathbf{B}-\frac{GM(1-\Gamma)\hat{\mathbf{r}}}{r^2}+\mathbf{g}_{lines}, \tag{5.6}$$

where $\mathbf{\Omega}$ is the angular velocity of the stellar rotation (assumed to be independent of the latitude). The meanings of the other symbols have already been given in section 3.2, but they are repeated here for convenience. The gravitational constant G and stellar mass M set the radially directed ($\hat{\mathbf{r}}$) gravitational acceleration, and $\Gamma\equiv\kappa_e L/(4\pi GMc)$ is the Eddington parameter, which accounts for the acceleration due to scattering of the stellar luminosity L by free electron opacity κ_e, with c the speed of light. The additional radiative acceleration due to *line* scattering, $\mathbf{g}_{lines}$, derived in chapter 2, has the form,

$$g_{lines}=\frac{f_d}{(1-\alpha)}\,\frac{\bar{Q}\kappa_e L_*}{4\pi r^2 c}\left(\frac{\partial v_r/\partial r}{\rho c\bar{Q}\kappa_e}\right)^{\alpha}, \tag{5.7}$$

where $\bar{Q}$ is a constant of the order ~ 1000 and f_d is the finite disk correction given by equation (2.88). The magnetic field $\mathbf{B}$ is constrained to be divergence free

$$\nabla\cdot\mathbf{B}=0, \tag{5.8}$$

and, under our assumption of an idealized MHD flow with infinite conductivity (e.g. Priest & Hood 1991), its inductive generation is described by

$$\frac{\partial\mathbf{B}}{\partial t}=\nabla\times(\mathbf{v}\times\mathbf{B}). \tag{5.9}$$

In principle, we should also include an equation for the energy balance, but as was argued earlier, hot-star winds can often be well approximated as an isothermal flow with the temperature $T=T_{eff}$ and the perfect gas equation of state,

$$P=\rho a^2, \tag{5.10}$$

where $a=\sqrt{kT/m}$ is the sound speed. In the next chapter we will consider hot-star winds that are adiabatic with polytropic index, $\gamma=5/3$.

5.2.3 Numerical Specifications

The specifics of our numerical discretizations and boundary conditions are essentially identical to the ones presented in chapter 3, with only two additional quantities, the rotational velocity, v_ϕ and azimuthal component of the magnetic field, B_ϕ to be considered at the boundary. As such, instead of repeating what has already been described in full detail, here we merely summarize the numerical specifications of our simulations.

The mesh is similar to that used in the non-rotating case (§3.2.3). In the radial direction it has $n_r = 300$ zones that spans from $r_1 = r_{min} = R_*$, the surface of the star, to the maximum radius of our computational domain at $r_{301} = r_{max} = 6R_*$. The radial mesh has a finer spacing near the surface with $\Delta r_1 \approx 0.0003R_*$ and then increases by 2% per zone. The mesh in co-latitude, on the other hand, uses n_θ zones that spans from $\theta = 0^o$ to $\theta = 180^o$ covering the two hemispheres from pole to pole. The resolution of the grid is increased near the magnetic equator at $\theta = 90^o$ by assigning minimum zone spacing of $\Delta\theta_{eq} = 0.3^o$ and then increasing it by 5% per zone towards each pole.

Our implementation of ZEUS-3D code uses the piecewise-linear-advection option (van Leer 1977) with time steps set to a factor 0.30 of the minimum MHD Courant time determined by the code itself. The boundary conditions at the two poles are set by simple *reflection* criterion. At the outer radius of our computational domain, all the MHD quantities are set by linear *extrapolation* assuming constant gradients.

At the stellar surface the density is fixed at a value $\rho_0 \approx \dot{M}/(4\pi R_*^2 a/5)$ where $\dot{M}$ is the characteristic mass loss rate of a 1D, nonmagnetic CAK model, and a is the isothermal sound speed. The radial velocity, v_r, is set by constant slope extrapolation. This allows the mass flux into the computational domain to adjust self-consistently. The radial flow in most zones is usually subsonic, although inflow

or outflow of up to the sound speed is permitted. We introduce the magnetic flux through the radial boundary as the radial component component of a dipole field $B_r(R_* = B_0 \cos(\theta)$ where B_0 is the fixed polar field strength different for each model as specified in Table 5.1. The latitudinal component of magnetic field, B_θ is set by constant slope extrapolation. For strong field cases, characterized by magnetic confinement parameter $\eta_* > 1$, the latitudinal velocity component is likewise linearly extrapolated, while for weak field cases, i.e. for $\eta_* \leq 1$ we set $v_\theta = 0$.

The main difference here from the boundary conditions for non-rotating magnetic models discussed in chapter 3 lies in the explicit inclusion now of the azimuthal components of the velocity and the magnetic fields. For non-rotating models, we set, naturally, $v_\phi = 0$ and $B_\phi = 0$. Here, v_ϕ at the surface is fixed to a value of the stellar rotation assuming a rigid body rotation. On the other hand, B_ϕ is set by a constant slope extrapolation.

The hydrodynamical flow variables, ρ and v_r are initialized to values for a spherically symmetric, steady, radial CAK wind, obtained from relaxing a 1D, non-magnetic wind simulation. The latitudinal component of the velocity, v_θ is set to zero everywhere, and the azimuthal component, v_ϕ is set to zero everywhere except at the stellar surface where $v_\phi = v_{rot}$, the rotation speed of the star. Detailed values for this are listed in table 5.1. The magnetic field is initialized to have a simple dipole form with $B_r = B_0(R_*/r)^3 \cos\theta$, $B_\theta = (B_0/2)(R_*/r)^3 \sin\theta$, and $B_\phi = 0$, with B_0 the polar field strength at the stellar surface. From this initial condition, the numerical model is then evolved forward in time.

5.3 Rotation Parameter

In chapter 3, we showed that a single dimensionless wind magnetic confinement parameter, $\eta_* \equiv 0.4\,(B_{100}^2\, R_{12}^2/\dot{M}_{-6}\, v_8)$ (eqn 3.7), which characterizes the ratio between the magnetic field energy density and the kinetic energy density, controls how much the magnetic field influences the wind. In this chapter we show that

rotational effects can be characterized with an additional parameter, expressed as the stellar rotation in the units of 'critical' rotation (defined below).

The increase of the stellar rotational speed increases the centrifugal force. Given a fixed rate of rotation of the star, Ω and under the assumption of a rigid body rotation, let us compute a critical radius r_c where the centrifugal force balances the effective force of gravity,

$$\begin{aligned} \frac{v_\phi^2}{r_c} = \frac{\Omega^2 r_c^2}{r_c} &= g_{eff} \\ &= \frac{GM_*(1-\Gamma)}{r_c^2}\,. \end{aligned} \tag{5.11}$$

Simple algebraic manipulation yields,

$$\Omega = \sqrt{GM_*(1-\Gamma)}\, r_c^{-3/2}\,. \tag{5.12}$$

In particular, if we assume that the critical radius occurs at the stellar surface, this will yield the critical rotational angular speed,

$$\Omega_c = \sqrt{GM_*(1-\Gamma)}\, R_*^{-3/2}\,. \tag{5.13}$$

Defining the stellar rotation rate in terms of Ω_c,

$$\omega \equiv \frac{\Omega}{\Omega_c}\,, \tag{5.14}$$

we can now write,

$$\omega = \left(\frac{r_c}{R_*}\right)^{-3/2} \tag{5.15}$$

or

$$\frac{r_c}{R_*} = \omega^{-2/3}\,. \tag{5.16}$$

From chapter 3 equation 3.6 we find that at the equator where $\theta = 90^0$ the ratio between the magnetic field and kinetic energy densities can be written as

$$\eta(r, 90^o) = \eta_* \frac{(r/R_*)^{2-2q}}{(1 - R_*/r)}\,, \tag{5.17}$$

where q is the exponent in the magnetic field strength power-law decline, e.g. $q = 3$ for a pure dipole field. Let us ignore the $(1 - R_*/r)$ term in the above equation and define the Alfven radius r_A such that $\eta(r_A) = 1$. Then,

$$1 = \eta_* \left(r_A/R_*\right)^{2-2q}, \tag{5.18}$$

or

$$\frac{r_A}{R_*} = \eta_*^{\frac{1}{2q-2}}. \tag{5.19}$$

Physically, r_A represents the maximum radius where the magnetic fields still dominate over the wind and can be directly related to the co-rotation radius. On the other hand, r_c is the maximum radius of co-rotation beyond which a rigidly-rotating fluid parcel is flung away by the centrifugal force.

Let us imagine a stellar model where $r_c = r_A$. Then the equations 5.16 and 5.19 yield,

$$\omega = \eta_*^{\frac{-3}{4(q-1)}}. \tag{5.20}$$

For a dipole magnetic field this reduces to $\omega = \eta_*^{-3/8}$ $(q = 3)$, and for a monopole-like field $\omega = \eta_*^{-3/4}$ $(q = 2)$.

Figure 5.1 shows these two curves (red and blue respectively) plotted against $\log \eta_*$, superimposed with the values of ω and η_* (dots) for all our isothermal MHD simulations. This curves serve us as a guiding lines for the simulations to be presented in this chapter. We shall see that the models that are below the red curve will be similar to the zero-rotation models discussed in chapter 3 & 4. On the other hand, the models that lie about the blue curve will be noticeably different in nature, and, as we will show, the extent of the last closed loop for those models will be limited by the co-rotation radius r_c. The models that lie in between the red and blue curves are the intermediate cases.

5.4 Simulation Results and Discussion

Our approach is to study the nature of the line-driven wind for various assumed values of η_* in combination with the rotation speed ω. For small values of $\omega \leq 1/20$ the rotation has no dynamical effect on the wind. But for larger values, $\omega > 1/4$ the wind is affected significantly. We do not consider rotation $\omega > 1/2$ since that requires consideration of oblateness and gravity darkening. The models with $1/20 < \omega < 1/4$, differ little from their zero-rotation counterparts discussed in chapter 3 & 4.

For our parameter study, we vary η_* solely through the variations in the assumed field strength. All the wind and stellar parameters are fixed to that of a typical OB supergiant, e.g. ζ Pup, in accordance with the previous chapters (see Table 3.4.3).

We evolve our models forward in time from an initial condition $t = 0$ when a dipole magnetic field is suddenly introduced into a spherically symmetric 1D CAK wind. To ensure asymptotic behavior of the flow, we run most of our models for about 900 ksec, which is very large compared to a characteristic flow crossing time, $t_{flow} = 5R_*/v_\infty \approx 25$ ksec. The rotation of the star is implemented by fixing the boundary value of the azimuthal velocity to that of a rigidly and uniformly rotating sphere. As noted earlier, we ignore the stellar deformation due to rotation itself.

For all the cases with different magnetic confinement parameter, η_*, just as in the non-rotational models discussed in chapter 3, the wind outflow quickly stretches the initial dipole field outward, opening up the closed magnetic loops in the outer wind into a nearly radial configuration. For modest values of ω the rotation has very little dynamical effect on the wind, but for $\omega \sim 1/2$ even for models with the lowest values of $\eta_* = 1/10$ the rotation can change the global structure of the wind compared to the equivalent model with no rotation. This is reflected in the increase of the net mass loss rates and the decrease of the terminal speeds.

The behavior of the wind in the inner part, near the surface, is more complex and depends largely on the value of η_* and the rotation speed ω. For the models with small values of $\eta_* < 1$ the field lines are stretched almost radially outward by the wind even in the inner part. But the finite departure from the radial configuration forces finite diversion of the wind material towards the equator leading to an enhancement of the density. The rotation and the associated Coriolis forces increase the equatorward deflection of the wind material. Thus, in general, in the equatorial region is denser for the rotational models compared to the zero-rotation cases. This is similar to the WCD model of Bjorkman and Cassinelli.

For the models with sufficiently strong values of $\eta_* > 1$, confinement of the wind by the magnetic closed loops near the stellar surface in combination with the high rotation speed can lead to quite complex flow pattern and interaction of the wind with the field lines. Before we describe this complex interaction near the surface of the star, let us discuss the effect of rotation on the global properties of the wind next.

5.4.1 Global Wind Structure of the Wind

5.4.1.1 The Models with Fixed Rotation but Different Magnetic Confinement Parameter

For the final time snapshot of the simulations, figure 5.2 compares the global wind structure of density (logarithmic color-scale) and the radial outflow for models without and with rotation ($\omega = 1/2$ or $V_{rot} = 250$ km/s at the equator) for the values of magnetic confinement η_* =1/10, 1 and 10 at . For all the models magnetic field lines (solid lines) are stretched outward into a radial configuration which reaches an asymptotic state within about 100 ksec of simulation time. To ensure that our simulations do not depend on the initial condition, these models were run for about $t = 900$ ksec.

For the weak magnetic field case ($\eta_* = 1/10$) with no rotation, the deflection of the wind material towards the magnetic equator leads to an enhanced density and decreased radial flow speed in the equatorial region. The inclusion of rotation ($\omega = 1/2$) makes these even more pronounced since the conservation of the angular momentum leads to an increased deflection of the flow towards the equator. Thus, compared to the polar value the equatorial density is enhanced by factor six, as opposed to factor two in the zero-rotation case. The radial velocity at the equatorial region for the rotational case, is lower as well, about 1400 km/s vs 1900 km/s for the non-rotational case. These differences are mainly consequences of the enhanced mass loss rate since the rotation reduces the effective gravity leading to higher mass loss rates.

Similarly, for the moderate and strong magnetic confinement cases, $\eta_* = 1, 10$, the rotation enhances the density in the equatorial region while decreasing the radial outflow velocity. This difference in the density enhancement vanishes as we increase the magnetic confinement parameter, η_*. The reason is that the higher η_* confines larger region of the wind outflow near the surface at the equator where the rotation is the most effective. The wind outflow emanating from higher latitudes has little azimuthal velocity, and as such the effect of rotation is inhibited.

We already discussed the latitudinal flows of the wind for the non-rotational case in chapter 3, and we find that the inclusion of rotation does not change the latitudinal flow pattern significantly. Figure 5.3, which compares latitudinal velocities v_ϕ of the rotational models ($\eta_* = 1/10, 1$ and 10) with zero-rotation cases as a color-scale demonstrates this fact. Note, however, the tendency is for the rotation to lower the latitudinal velocity. This is consistent with the generalized 2D Weber and Davis models calculated by Sakurai (1985), who shows that there is a poleward deflection of the wind due to buildup of the toroidal magnetic fields. The direct comparison is not an easy task since Sakurai used split-monopole magnetic field,

while we use a dipole field.

5.4.1.2 The Models with Fixed Magnetic Confinement but Different Rotations

Figure 5.4 shows the hydrodynamic quantities ρ, v_r, v_θ and v_ϕ as color-scale plots for the models with magnetic confinement $\eta_* = \sqrt{10}$ ($B_{Pole} = 520$G) and rotation $\omega = 0, 1/4$ and $1/2$. The left column shows the global structure of density as a logarithmic color-scale superimposed with the magnetic field lines (solid lines) projected onto $r-\theta$ plane. The global configuration of the field and wind structures are very similar. For the model with the highest rotational speed ($\omega = 1/2$ or $V_{rot} = 250$km/s) the equatorial density is enhanced compared to the two other models. This leads to the lower outflow velocities in that region (the second column). There is hardly any difference in the latitudinal flow velocities for these three models since they all have very similar magnetic field configurations. In the ideal MHD approximation the fluid follows the field lines, thus the net deflections towards the equator are also comparable. In the open field regions the azimuthal velocities for the two rotational models are nearly angular momentum conserving. In the magnetically closed region near the surface about the magnetic equator, the wind material co-rotates with the star, but eventually the wind dominates over the field and the fluid flows out conserving angular momentum.

5.4.2 Co-rotation and Variability of the Near-Surface Wind Flow

For the cases with the magnetic confinement $\eta_* > 1$ the flow near the surface of the star is quite structured and variable. Figure 5.5 shows snapshots of magnetic field lines (solid lines) and density (as logarithmic color-scale) for the case of moderately strong magnetic confinement parameter, $\eta_* = 6.4$ ($B_{Pole} = 800$G), zoomed in on the near-star equatorial region at time intervals long after the initial condition ($t > 500$ ksec). The dashed line represents the maximum radius of co-rotation

($r = 1.6R_*$) beyond which a fluid parcel is gravitationally unbound. The magnetic fields channel the wind material towards the equator where a dense disk-like structure is formed. Since the line-force is inefficient for dense plasma, this structure eventually falls down due the gravitational pull. The material *below* the dashed line falls *inward* (as suggested by arrows for clarity) forming knots.

Note, however, that the knots formed *above* the dashed line are flung *outward*. The reason is that these knots are spun up by the magnetic fields up to critical rotation speed, so that the resultant outward centrifugal force is larger than the inward pull of gravity. Thus these centrifugally driven dense knots tear through the field lines and get ejected. This can be seen more clearly from the figure 5.6, where the azimuthal velocity of the wind material is shown as a color-scale plot in the unit of co-rotation velocity, $\chi \equiv v_\phi^{simulation}/\Omega r \sin\theta$. Thus the material flowing with $\chi = 1$ is rigidly rotating with the star. Clearly, the material above the dashed line reaches the maximum co-rotation velocity and thereby is flung away.

Note, also, that there is some rarefied material above the dense equatorial region that spins counter to the direction of stellar rotation. Perhaps this is a numerical artifact, but very little mass is involved. Therefore, we just ignore it for now. The precise reasons for this will require further investigation.

The animations of time sequences of the models with magnetic confinement $\eta_* = \sqrt{10}$ ($B_{Pole} = 520$G) and rotation $\omega = 1/4$ and $\omega = 1/2$ show that for the model with the higher rotational speed, the inner wind behaves much as the model described above ($B_{Pole} = 800$G case), i.e the dense knots are formed, and the material below the co-rotation radius falls back onto the star while the material above it is flung away. The case with the lower rotation speed is somewhat different; the knots do not tear through the field lines, but instead all fall back onto the stellar surface, just as in the zero-rotation case discussed in earlier chapters. The reason is that, here, the magnetic confinement is not high enough to keep material co-rotating

up to the co-rotation radius, which occurs for the $\omega = 1/4$ case at $r \approx 2.5R_*$. In the case of $\omega = 1/2$ the co-rotation radius is only $r \approx 1.6R_*$, and the field is strong enough to co-rotate the material up to that radius. This can be well illustrated by animations, but is difficult to illustrate on paper.

In the somewhat different case of x-ray pulsars binary systems powered by mass exchange accretion onto a neutron star, Illarionov & Sunyaev (1975) and Stella, White & Rosner (1986) show that for strong enough surface magnetic field of a rotating star, the centrifugal force can inhibit or even quench the accretion via the "propeller" mechanism. Despite the different contexts, the physical mechanisms involved is actually somewhat analogous to the results for our rotating magnetized winds. In our simulations, the wind material is collected from the star itself, and then is spun up by the magnetic field to super-Keplerian velocities, leading to episodic mass ejecta and preventing the formation of a steady disk. In the case of the "propeller" model of Stella, White & Rosner, the material is collected from the companion star (usually O or B star) via accretion which then is spun up by the field. Sufficiently strong magnetic field reverses the direction of the accretion flow by spinning accreting material to high enough velocities so that it is flung away outward (from the neutron star).

5.4.3 Azimuthal Components of the Flow and Field

The top row of the figure 5.9 shows azimuthal velocity recast in the unit of co-rotation ($\chi \equiv v_\phi/\Omega r$) plotted as color-scale for the models with magnetic confinement $\eta_* = 1/10, \sqrt{10}$ and 10 and the rotation $\omega = 1/2$ ($V_{rot} = 250$ km/s). For the lowest magnetic confinement case, there is no co-rotation anywhere in the computational domain since the field is too weak to force the wind to co-rotate.

For the highest magnetic confinement case, the region within the closed loop co-rotates with the star. However, because the outward centrifugal force beyond the co-rotation radius is larger than the inward pull of the gravity, the co-rotation

radius limits the last closed magnetic loop. This is apparent in figures 5.5 and 5.7 where solid lines represent the co-rotation radius, and clearly the closed magnetic loops do not cross this distance.

The magnetic fields here act as a moment arm and provide significant amount of momentum to the wind. One may ask if the field could launch the wind material into a Keplerian orbit. The results above demonstrate that the wind obtains large angular momentum while being driven radially outward by the stellar radiation. Thus the radial outflow velocity prevents the spun up material to settle into a Keplerian orbit. Consequently, our simulations show a dense equatorial outflow in lieu of a Keplerian disk.

For all the rotational models, far away from the star azimuthal velocity falls off as $\sim 1/r$ asymptotically, conserving the angular momentum. This is not surprising since we already argued in chapter 3 that wind always wins over the field simply because the field strength declines significantly faster than the wind ram pressure.

On the other hand, the azimuthal component of the magnetic field along a given radial ray (i.e. fixed θ) also falls off as $\sim 1/r$. Because the radial component declines as $\sim 1/r^2$ (radial configuration), this implies that far away from the star the field lines are wrapped in spiral patterns. This is analogous to the generalized Weber and Davis model (Sakurai 1985) for split-monopole surface magnetic field.

5.4.4 Radial Outflow and Mass Loss Rates

Figure 5.10 shows the radial outflow velocity (top panel) and the mass flux density (bottom panel) at the maximum radius of our computational domain, $r = 6R_*$ for models with fixed rotational velocity ($\omega = 1/2$) and the magnetic confinement ranging from $\eta_* = 1/10$ to 10 in increment of $\sqrt{10}$ as a function of $\mu = \cos\theta$. For all the cases the flow velocity decreases and the mass flux density increases towards the equator.

This can be explained qualitatively by figure 5.11, where the mass flux density near the stellar surface ($r = R_*$) is plotted against $\mu = \cos\theta$. The pole in this figure corresponds to $\mu = 1$. We note that the model with the lowest confinement $\eta_* = 1/10$ has the lowest mass flux rate at the pole (blue curve) but the highest near the equator. It is hardly surprising since for such a low confinement the wind dominates over the wind right from the surface and stretches the field lines into a radial configuration. Therefore the only effect that increases the mass flux is the reduced effective gravity due to increased rotation towards the equator. The higher mass flux at the equator leads to lower outflow velocity.

The cases with higher confinement parameters are somewhat more complex. The field lines are nearly radial only near the pole, but near the surface about the equator the magnetic field is able to control the wind, and force the flow at a tilted angle. We already have shown in chapter 4 that the mass flux for the tilted flow is reduced by factor of the square of the cosine of the angle. As such, for these cases the effect of the rotation competes with the effect of the tilted flow.

Figure 5.12 shows total integrated mass loss rates for the same models as a function of the magnetic confinement parameter for different rotational models. The top curve shows the mass loss rates in the unit of $10^{-6} M_\odot/yr$ for the models with $V_{rot} = 250 km/s$, and the bottom one for $V_{rot} = 125 km/s$. There is a clear trend of decrease of the mass loss rate with the increase of the strength of the magnetic field. This seems contrary to what Friend and MacGregor (1984) concluded in their analysis of rotating magnetic wind models that combined the Weber and Davis (1967) description of a rotating magnetic solar wind with the CAK theory of line-driven winds in a point source approximation. They found that the mass loss rate increases with the increase of the field strength. Poe and Friend (1986) extended these models to include the finite disk correction factor, and arrived essentially to the same conclusion.

These rotating magnetic wind models were limited to the equatorial plane and were essentially 1D in nature. When the mass loss rates were computed, it was assumed that mass flux was spherically symmetric. In our dynamical 2D rotating magnetic wind models, higher surface dipole-like magnetic fields confines larger area around the equatorial region, as was shown in chapter 3. The effective gravity is the lowest at the equator due to the highest effect of the centrifugal force there, thus the mass loss rate would have been the highest at the equatorial region if the wind were not confined by the fields.

5.4.5 Angular Momentum Loss

The wind from a rotating star carries away angular momentum. In this section, we attempt to estimate how much angular momentum is lost from the star, and what the characteristic spin-down time scale is.

In the Weber and Davis (1967) model, where the wind is limited to the equatorial plane, the angular momentum loss rate is approximately,

$$\frac{dJ}{dt} \approx \frac{2}{3}\,\dot{M}\Omega r_A^2\,, \tag{5.21}$$

where r_A is the Alfven radius. The characteristic braking time thus is,

$$\tau = \frac{J}{dJ/dt} \approx \frac{3I\Omega}{2\dot{M}\Omega r_A^2} \approx \frac{3\iota M R_*^2}{2\dot{M} r_A^2}\,, \tag{5.22}$$

with the moment of inertia of the star, I assumed to be,

$$I = \iota M R_*^2\,. \tag{5.23}$$

Here, ι is a constant that depends on the density distribution of the star, e.g. for a uniform sphere with mass, M, $\iota = 2/5$ and $I = (2/5) * MR^2$. Realistically, $\iota \approx 1/10$ for most stars which usually have dense cores.

In our numerical 2D simulations, we can directly compute the rate of angular momentum loss first by defining j, the flux of angular momentum loss rate,

$$j(r) \equiv \dot{m}(r) v_\phi(r) r \tag{5.24}$$

where $\dot{m}(r) \equiv \rho v_r$, and then integrating it over the whole space occupied by the wind,

$$J = \int j \, dV \, . \tag{5.25}$$

The estimated values of τ for our various models is listed in Table 5.1. Note that if we assume $\iota = 1/10$ the characteristic braking time scale is of order ~ 1 Myr only for most of our MHD models. Note also that for the models with $\eta_* \leq 1$ and the same rotational velocities, the characteristic braking time scales are comparable since the field is too weak to force the wind to co-rotate, and the momentum gained by the wind depends mainly on the surface rotation.

5.4.6 Observational Implications

As discussed in chapter 3, the stellar winds of hot stars are variable on large scale due to the presence of persistent structures. They often manifest themselves through the so called Discrete Absorption Components (DACs) which are absorption features in the wind that have an apparent slow outward acceleration. The time-series observations of UV lines with *IUE* (see e.g. Kaper 1999) suggest that DACs are longitudinally extended and spiral shaped structures with recurrence time-scale closely related to the rotation period. This implies that the cause of DACs may be rooted in the processes in the underlying star. One obvious candidate is the magnetic field in association with the stellar rotation.

Our MHD models presented here, although 2D in nature, may provide some hints if the magnetic fields can be responsible, at least, in part for some of the large scale variability inferred from the UV lines. We showed earlier that for high enough magnetic confinement and rotation, the dense material at the top of the closed loops tears through the field lines due to the centrifugal force. Such structures appear ring-like in 2D formulation, but for the rotation tilted w.r.t. the magnetic axis, these

Table 5.1: Summary of Mass-Loss Rates

B_{Pole} (G)	η_*	ω_c	max(r_{cor}) (R_*)	max(v_r) (km/s)	max(v_θ) (km/s)	$\dot{M}_{net}$ ($10^{-6} M_\odot/yr$)	τ ($10^6 yr$)
93	1/10	1/2	1.6	2330	70	3.52	13.75 ι
295	1	1/2	1.6	2560	265	3.45	13.75 ι
520	$\sqrt{10}$	0	-	2830	400	2.20	-
520	$\sqrt{10}$	1/4	2.5	2800	385	2.33	28.4 ι
520	$\sqrt{10}$	1/2	1.6	2720	340	3.38	14.25 ι
800	6.4	1/4	2.5	3000	950	1.88	16.5 ι
800	6.4	1/2	1.6	2860	880	2.07	14.5 ι
930	10	1/20	4.6	3600	1500	1.60	165.5 ι
930	10	1/2	1.6	2920	1000	2.62	16.25 ι
1860	40	1/4	2.5	4330	3500	1.17	21.25 ι

may appear as dense, slow blob-like structures. However, the simulation of such structures requires full 3D formulation, which we leave for future study.

All the observational implications associated with the zero-rotation MHD models, discussed in §3.5.3, apply here as well. As such, we will not repeat the analysis.

5.5 Chapter Summary

In this chapter we studied how rotation can influence the magnetically channeled line-driven stellar winds discussed in chapter 3 and 4. As an initial study, we ignored the effects of oblateness, gravity darkening and limb darkening. Our simulations were based on idealization of isothermal flow driven by radial line-force. Our conclusions can be summarized as follows:

1. The degree of the overall influence of rotation depends largely on the rotation speed ω expressed in the unit of critical velocity, in combination with the wind

magnetic confinement parameter, η_*. Regardless of the confinement parameter, for the models with $\omega \sim 1/20$ and typical stellar and wind parameters of ζ Pup-like O-supergiant, the rotation has very little effect.

2. In general, rotation enhances the equatorial density and reduces the equatorial flow velocity. For small confinements, $\eta_* \leq 1$ and rotation $\omega = 1/2$ the equatorial density is noticeably enhanced compared to the zero-rotation cases. Higher density leads to slower equatorial outflow.

3. For strong magnetic confinements for which the Alfven radius is *smaller* than the co-rotation radius, the simulations are similar to the non-rotational cases. The field remains closed in loops near the equatorial surface. Wind outflows accelerated upward from opposite polarity footpoints are guided towards a strong collision near the loop tops. The material that is stagnated as a result of this, is eventually pulled back by gravity onto the star in a complex flow pattern. Unlike, for the strong confinement cases for which the Alfven radius is *larger*, the stagnated material doesn't reach the co-rotation radius, and thus is not flung away outward.

4. For strong magnetic confinements for which the Alfven radius is *larger* than the co-rotation radius, the situation is quite different from the the zero-rotation case. Some of the material that is stagnated within the closed loops and lies above the co-rotation radius, is spun up to speeds such that the outward centrifugal force is larger than the inward pull of gravity. Consequently, this material punches through the field lines and is flung away bullet/ring-like patterns. On the other hand, the material that lies below the co-rotation radius, is pulled back by the gravity. Thus the co-rotation radius sets an upper limit to the radius of the last closed loop for strong confinement cases.

5. For strong confinements, $\eta_* > 10$ rotation has limited influence on the global wind structure since the region with the highest rotation speeds near the equator is magnetically confined. The global wind structure is determined by the outflow from high latitudes where rotation speed is less by $\sin\theta$ factor. However, some episodic mass ejections, where the material accumulated at the top of the magnetic closed loops is flung outward centrifugally, makes these models somehow more variable compared to non-rotational cases.

6. The magnetic field acts as a moment arm in providing angular momentum to the wind. However, it is not an efficient mechanism to launch material into a Keplerian orbit. A key reason behind this is the significant radial outflow velocities of the spun up material. In order to keep the material in a Keplerian orbit, other physical considerations must be taken into account, e.g. shut off the line force for the dense co-rotating material which can easily be achieved if the gas is very hot. Thus, in our isothermal MHD simulations of line-driven winds, dense slowly outflow equatorial disk-like structure is formed.

7. The stellar wind from a rotating hot star carries away significant amount of angular momentum. Our simulations show that the characteristic spin-down time is about a few million years for ζ Pup-like O-supergiants with surface magnetic fields of a few hundred Gauss and rotation $\omega = 1/2$.

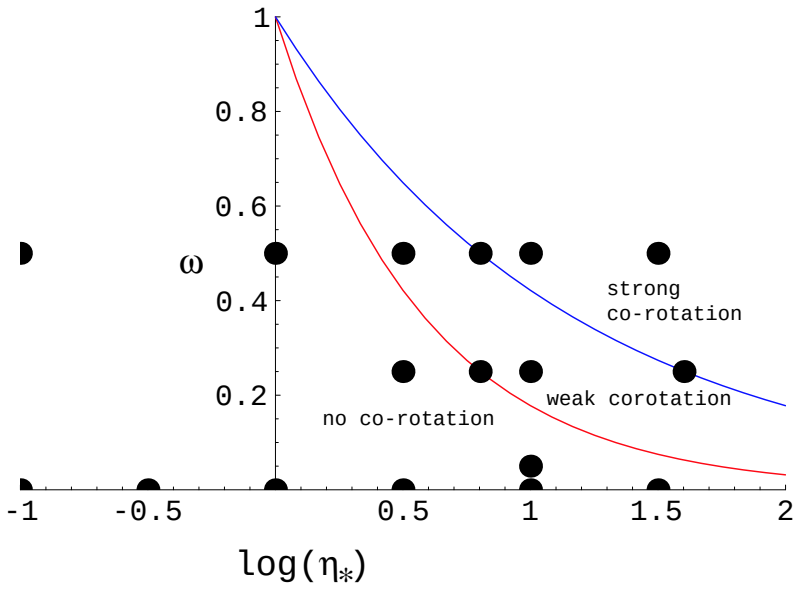

Figure 5.1: The rotation rate ω vs $\log \eta_*$ which defines the parameter space of our study in this chapter. The solid lines represent the maximal rotation rate for which co-rotation and Alfven radii are equal (eqn (5.20) for assumed monopole like magnetic field (top, blue) and dipole like field (bottom, red). The dots are the values of ω and η_* used in our simulations. The results of representative simulations are presented in the text.

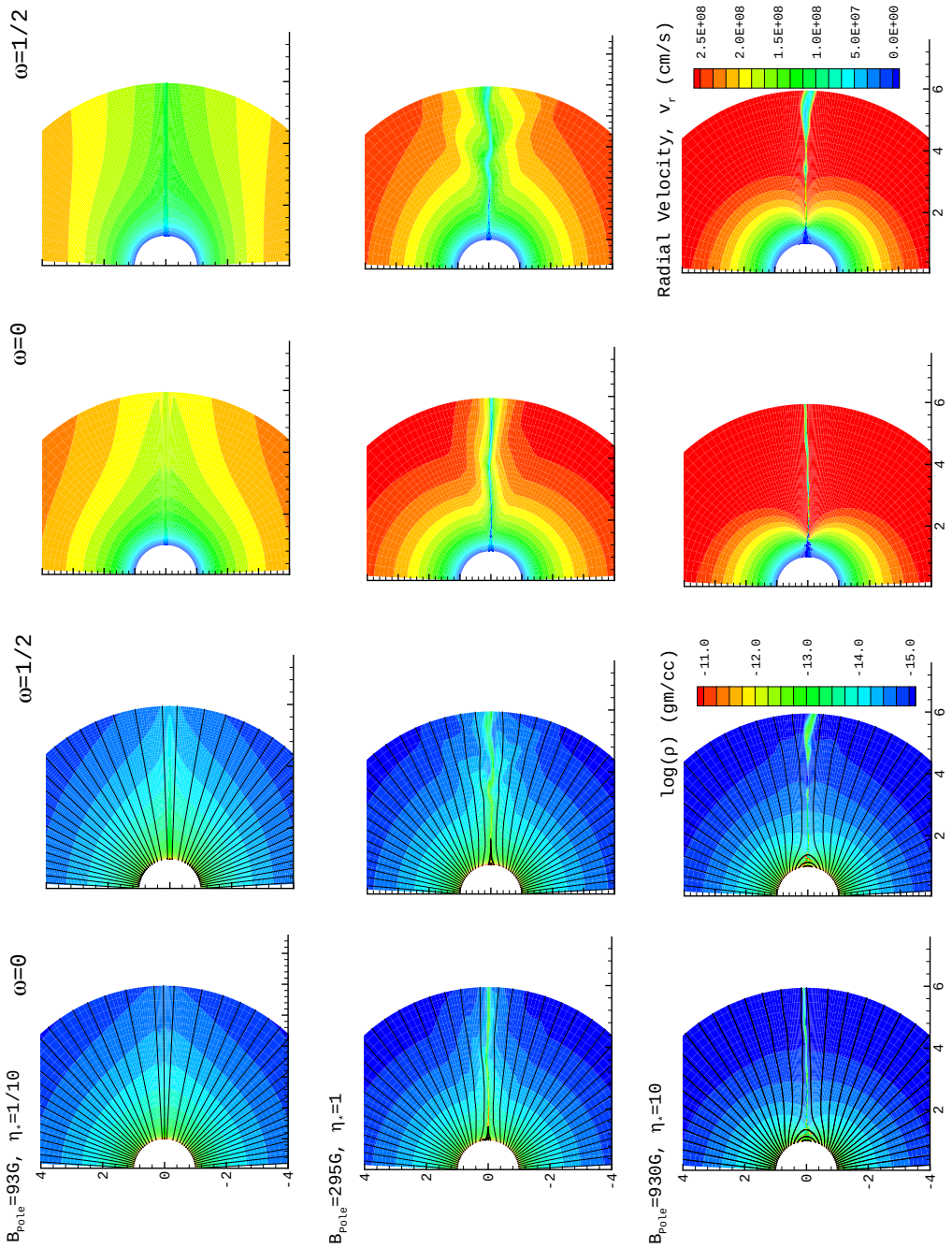

Figure 5.2: Snapshots of density and radial velocity at time, $t \approx$ 500ksec for various models with (the second and the last column) and without (the first and the third column) rotation plotted as color-scale. The solid lines in the left two columns represent field lines.

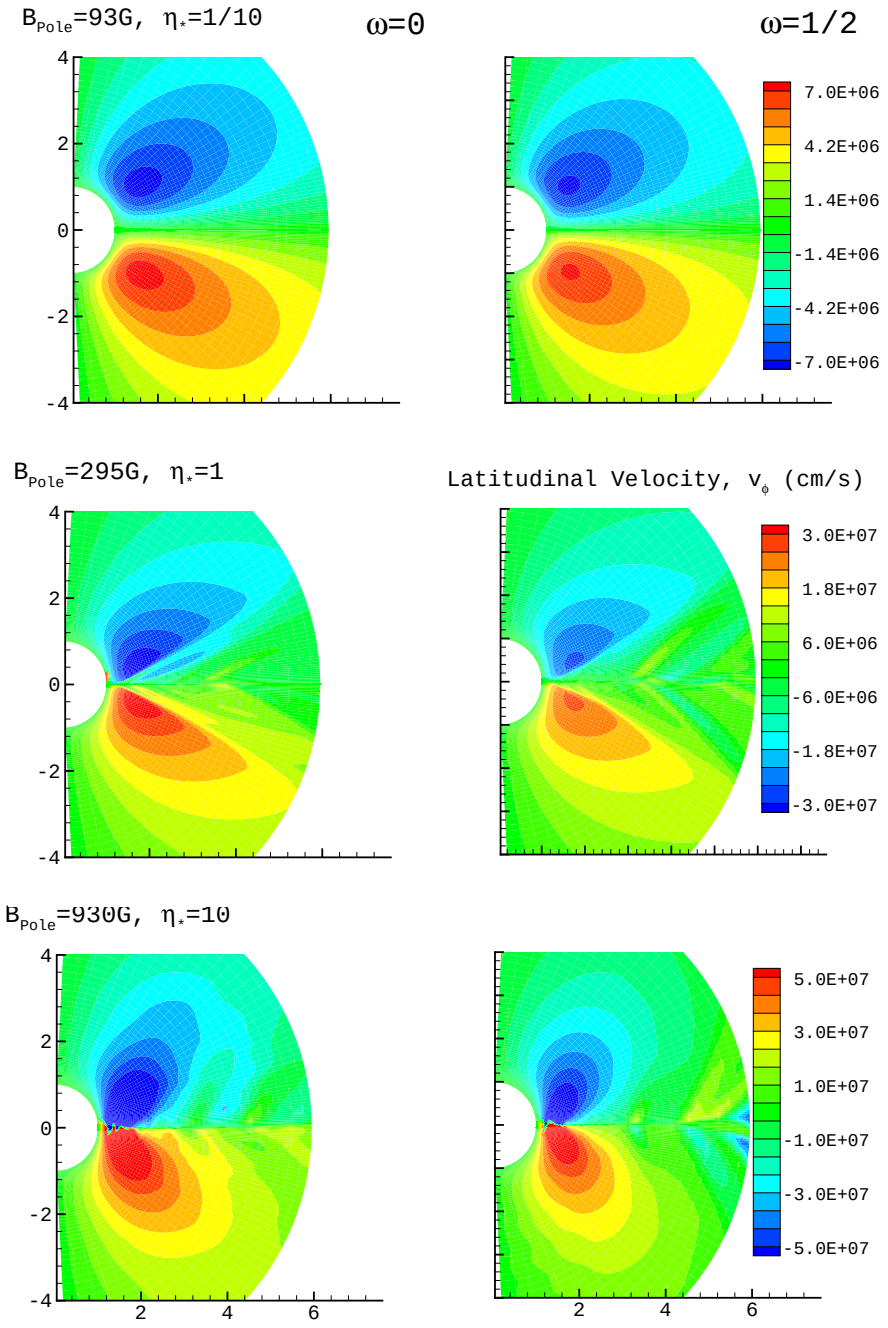

Figure 5.3: Snapshots of latitudinal velocity at time, $t \approx 500$ ksec for various models with (right column) and without (left column) rotation plotted as color-scale.

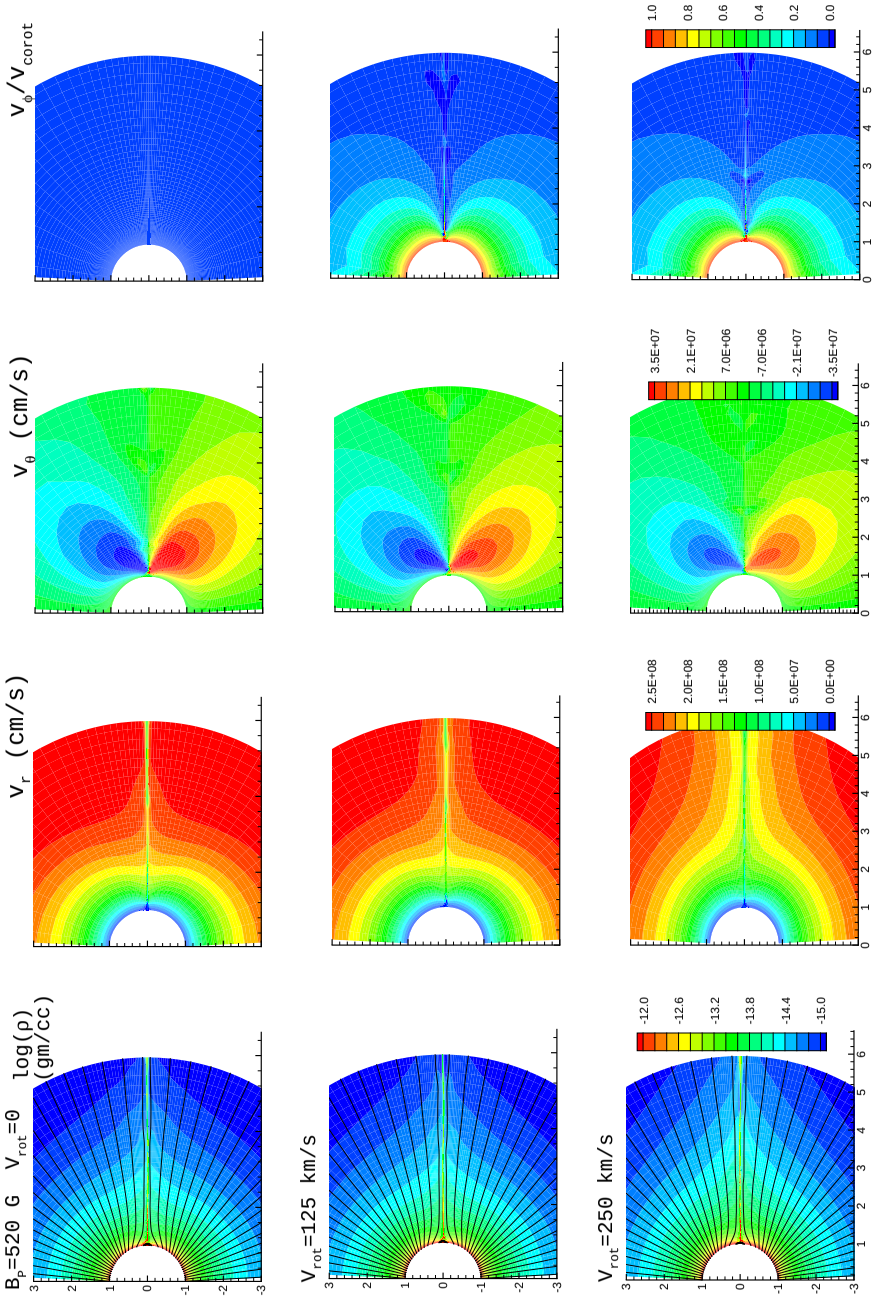

Figure 5.4: Color-scale plot of ρ, v_r, v_θ and v_ϕ with fixed $\eta_* = \sqrt{10}$ and rotation $\omega = 0, 1/4$ and $1/2$ (from top to bottom respectively). The solid lines are the magnetic field lines with the strength proportional to the density of the lines.

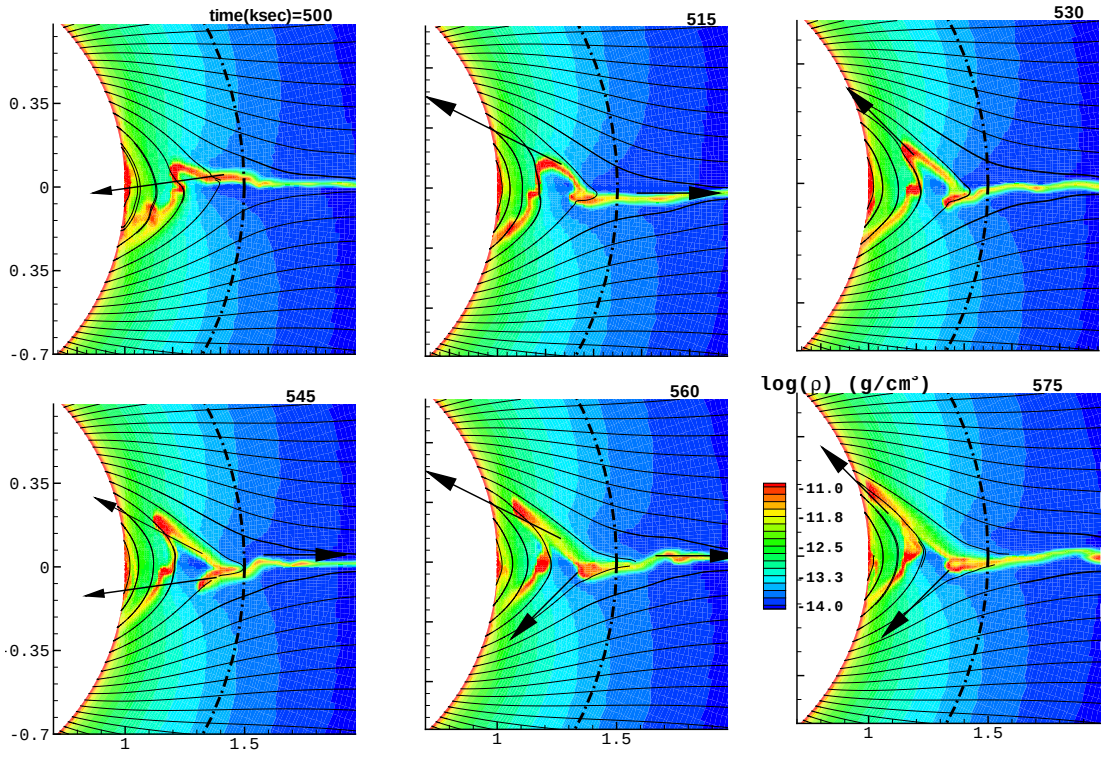

Figure 5.5: Snapshots of density (as logarithmic color-scale) and field lines (solid lines) at the labeled time intervals chosen to show how some of the dense wind material channeled by the field towards the equator falls back onto the star and some of the material that got spun up to high speeds, tears through the field lines and is flung away. This depends on whether the fluid parcel is located below or above the maximum radius of co-rotation (dashed line) beyond which a fluid parcel is gravitationally unbound due the centrifugal force. This model was evolved from the initial condition of a dipole field superimposed upon a spherically symmetric wind of a fast rotating ($\omega = 1/2$ or $V_{rot} = 250 km/s$) star with moderate magnetic confinement, $\eta_* = 6.4$ ($B_{Pole} = 800 G$).

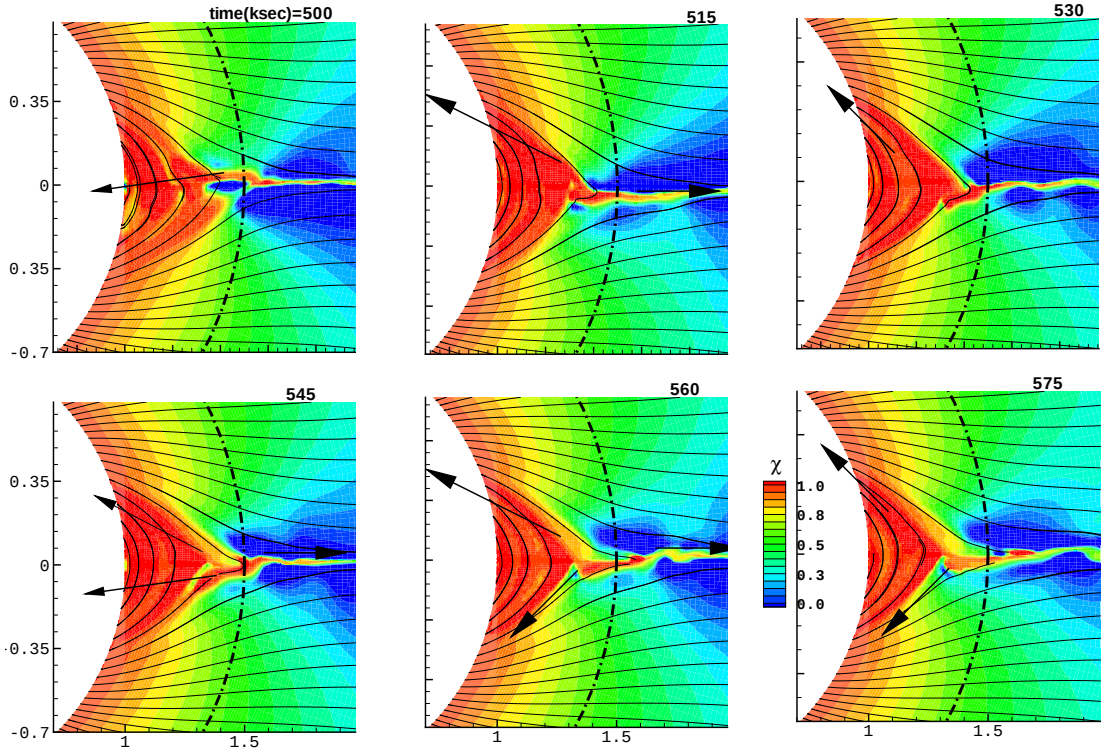

Figure 5.6: Snapshots of the azimuthal velocity (for the same model as in Fig 5.5), v_ϕ expressed in the unit of co-rotation speed ($\chi \equiv v_\phi/\Omega r \sin\theta$) (as color-scale) and field lines (solid lines) at the labeled time intervals to emphasize that the ejected material has high azimuthal velocities.

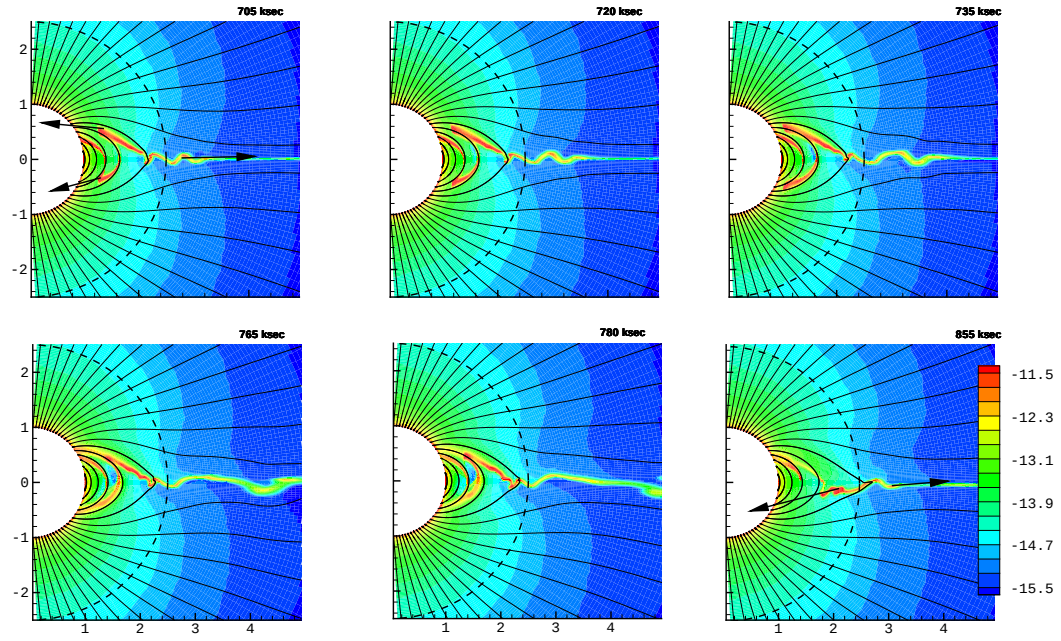

Figure 5.7: Snapshots of density (as logarithmic color-scale) and field lines (solid lines) at the labeled time intervals chosen to show again how some of the dense wind material channeled by the field towards the equator falls back onto the star and some of the material that got spun up to high speeds, tears through the field lines and is flung away. This model has a slow rotation ($\omega = 1/4$ or $V_{rot} = 125 km/s$) but strong magnetic confinement, $\eta_* = 40$ ($B_{Pole} = 1860 G$). This reinforces the idea that the last magnetic closed loop is limited by the co-rotation radius.

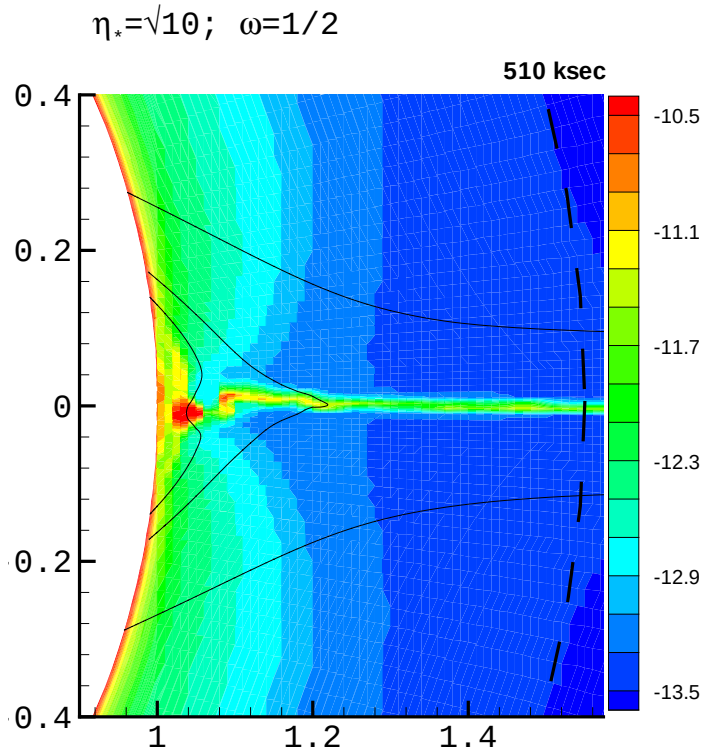

Figure 5.8: Color-scale plot of $\log \rho$ with $\eta_* = \sqrt{10}$ ($B_{Pole} = 520$G). Solid lines are the magnetic field lines, the dashed line is the co-rotation radius. All the dense knots formed within the closed magnetic loops fall back onto the stellar surface. The aim here is to show that if the Alfven radius is less than the co-rotation radius (which the case for this model), then there will be no knots tearing through the field lines and being flung away centrifugally.

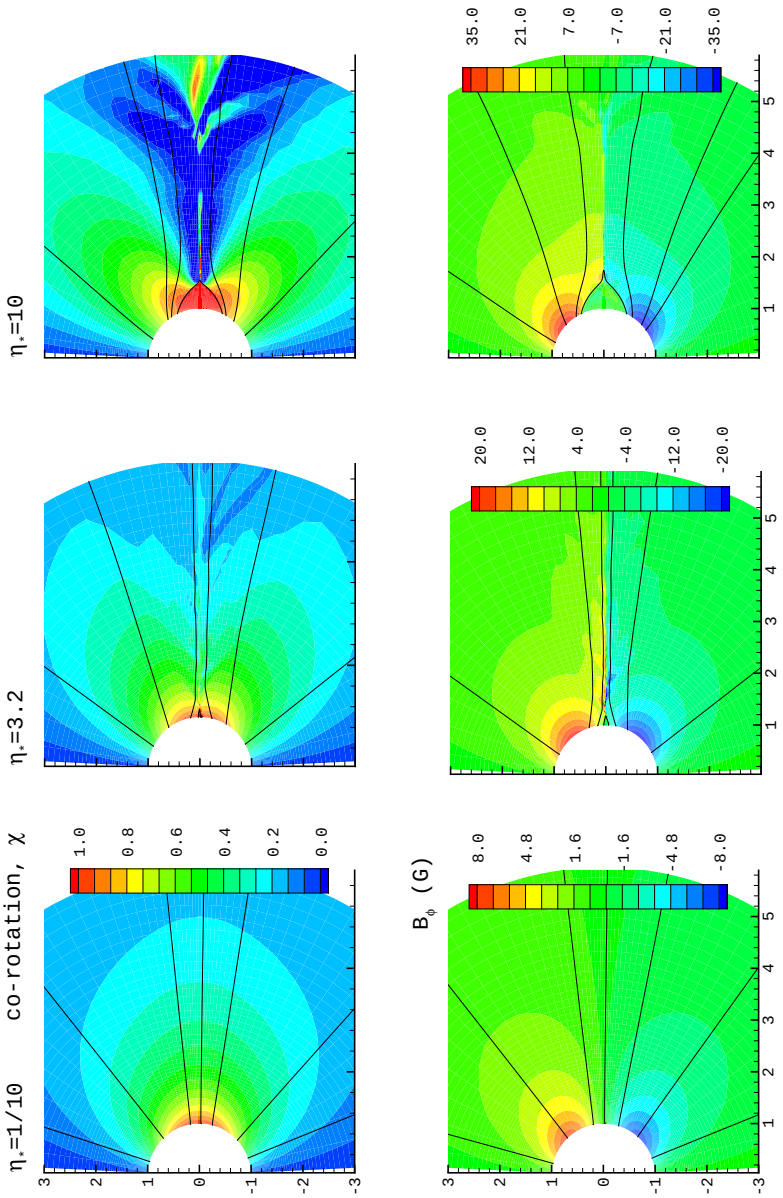

Figure 5.9: Color-scale of the azimuthal velocity v_ϕ expressed in co-rotation unit $\chi \equiv v_\phi/\Omega r$ (top row) and the azimuthal field component B_ϕ (bottom row) for the models with magnetic confinement $\eta_* = 1/10, \sqrt{10}$ and 10 and the rotation $\omega = 1/2$ ($V_{rot} = 250$ km/s). The solid lines are the field lines, chosen arbitrarily to show overall configuration. Note the clear co-rotation region for the highest magnetic confinement case for which $B_\phi = 0$, essentially.

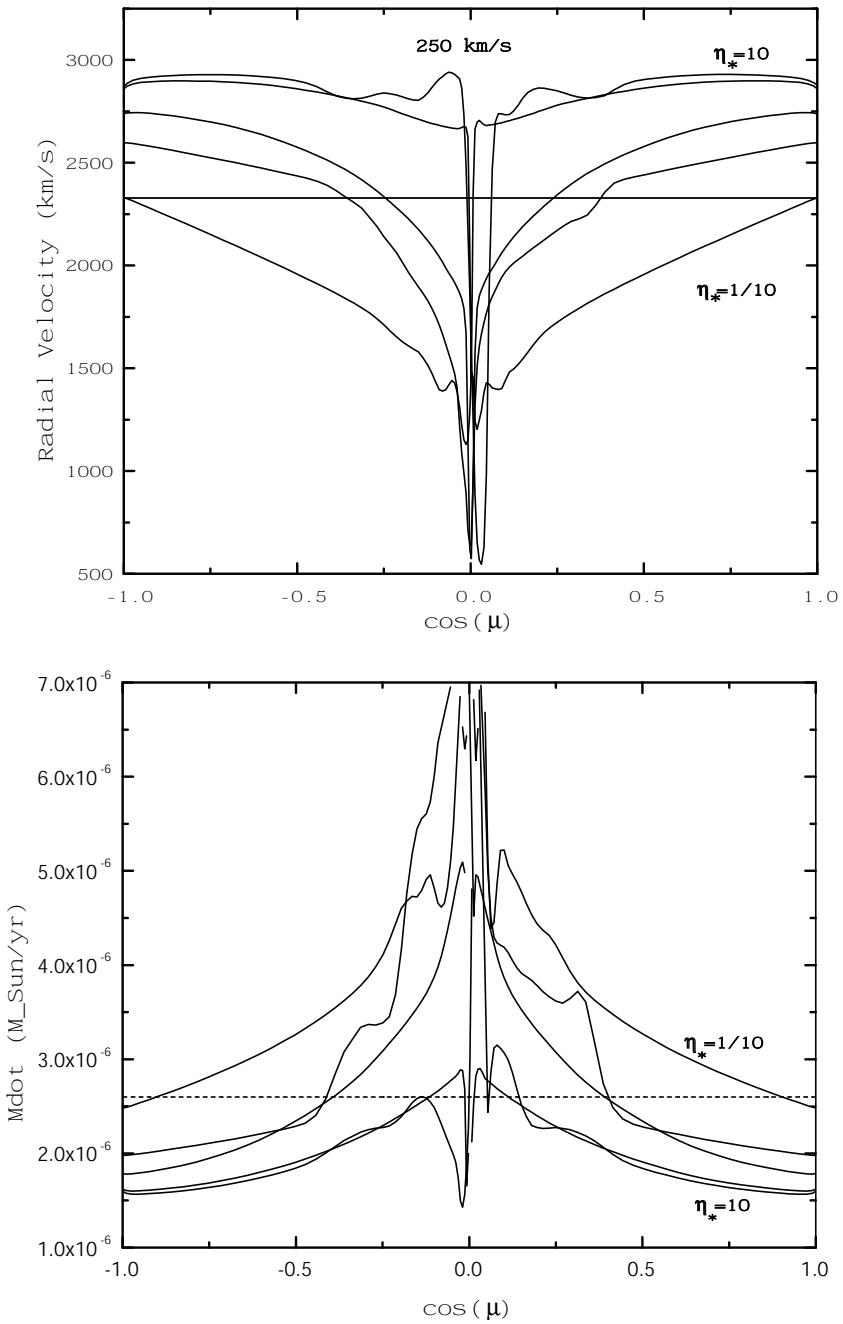

Figure 5.10: a. Computed radial flow speeds (top) b. Mass loss rate (bottom) at $R_{max} = 6R_*$ for models with fixed rotation rate $\omega = 0.5\omega_c$ and values of $\eta_* = 10, 6.4, \sqrt{10}, 1, 1/10$.

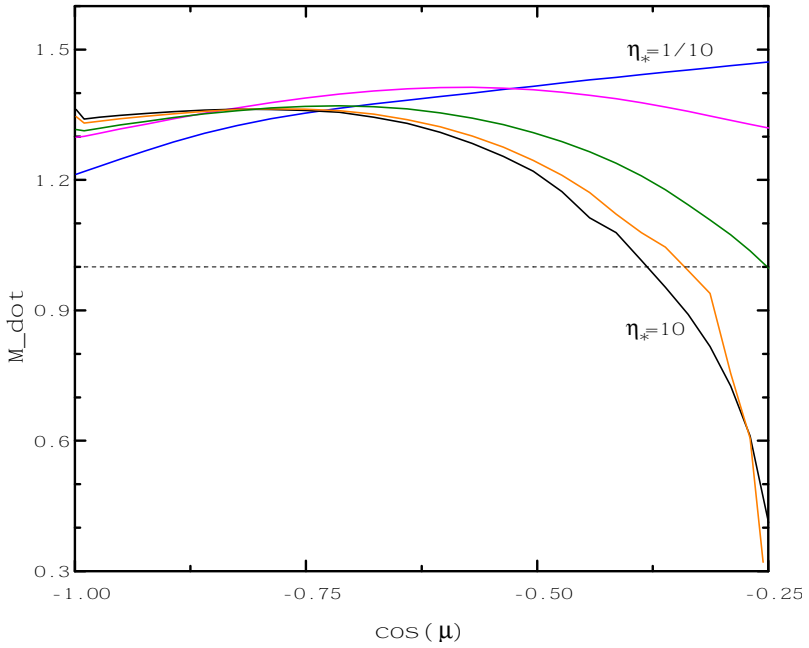

Figure 5.11: Computed mass flux rates at $R_{min} = R_*$ for models with fixed rate $\omega = 1/2$ $\eta_* = 1/10, 1, \sqrt{10}, 6.4$ and 10 normalized by the value of the non-magnetic case plotted against $\mu = \cos\theta$. The range of μ was limited so that the chaotic structure near the equator does not complicate the picture here. The aim here is to show that the rotation increases the mass loss rate in general, but because in the MHD simulations presented here are self-consistent, the wind has to compete with the magnetic fields, leading to reduction of $\dot{M}$ $\sim$ the square of the tilt angle of the flow lines [see Chapter 4]. This explains the reduced $\dot{M}$ near the magnetic equator for higher confinement cases.

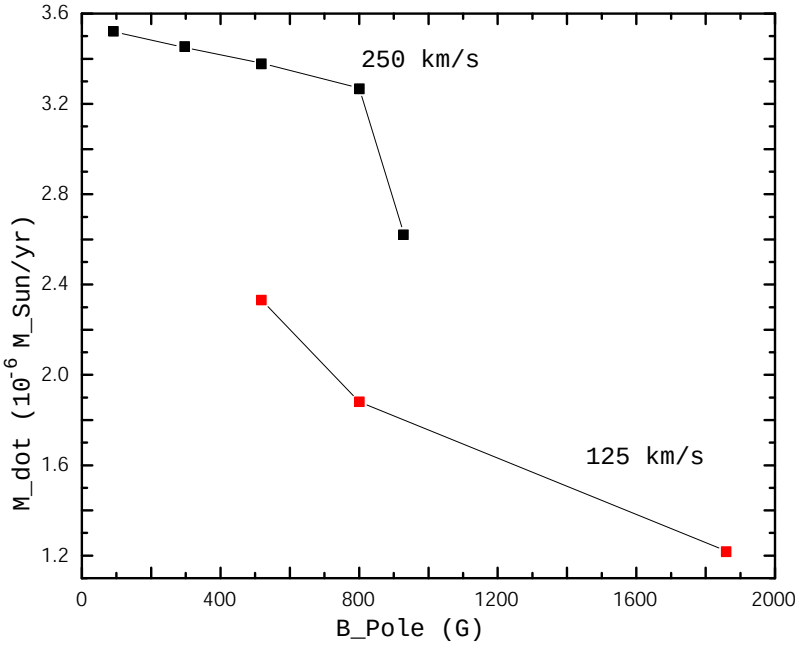

Figure 5.12: Mass loss rates at $R_{max} = 6R_*$ for models with fixed rotation rate $\omega = 0.5, 0.25\,\omega_c$ plotted against magnetic field strength.

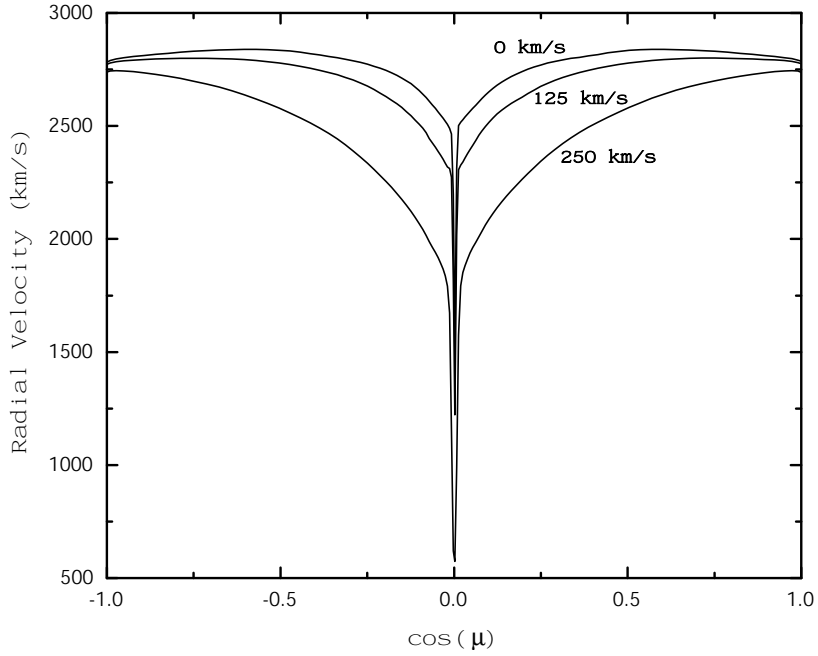

Figure 5.13: Computed radial flow speed at $R_{max} = 6R_*$ for models with fixed $\eta_* = \sqrt{10}$ and various rotation rate $\omega = 0$, 1/4 and 1/2 ω_c corresponding to $v_\phi = 0$, 125 and 250 km/s as noted in the figure.

Chapter 6

MAGNETICALLY CHANNELED ADIABATIC LINE-DRIVEN WINDS

The magnetically channeled line-driven winds discussed earlier (chapters 3-5) were assumed to be isothermal. We argued that the radiative processes in hot-star winds are very rapid compared to dynamical processes, and the UV photo-ionization keeps the wind at near the stellar effective temperature (Drew 1989; Pauldrach 1987). This idealization is valid, as we shall see below, for dense winds near the star, within a few stellar radii from the surface. But we are also interested in less dense winds and low density regions of a dense wind, far from the star. To model such low density regions, one has to consider a full energy equation including the radiative cooling term.

As an initial attempt, we first consider an adiabatic wind with no cooling. Although physically not a plausible case for high $\dot{M}$ winds, this represents the other extreme of an isothermal wind model, where the wind is assumed to cool instantaneously. Here we do not carry out a full parameter study of the adiabatic hot-star winds, but instead present some adiabatic counterparts of the isothermal models, and show that for strong magnetic confinements they are very different from each other.

6.1 Radiative Cooling

In order to understand the importance of radiative cooling in hot-star winds, it is necessary to examine the nature of shocks first. A shock is a very complex

non-equilibrium flow that results from collision of gases of different velocities. It can heat up the gas to very high temperatures estimated to be,

$$T_{shock} \approx 1.5 \times 10^5 \left(\frac{v_0}{100\ km\ s^{-1}} \right)\ K\,, \tag{6.1}$$

where v_0 is the velocity jump of the shock (Castor 1987; Babel and Montmerle 1997b). In the MHD models presented in this thesis the velocity jumps of the shock can be of the order $300 - 1000$ km/s. This corresponds to the gas temperature of order $10^6 - 10^7$ K.

There are a number of processes that occur in a region of a shocked gas. In the isothermal idealization the problem is simplified by assuming that the gas cools instantaneously, leaving the gas temperature unchanged. In practice, the pre-shock kinetic energy of the gas is converted into internal energy. The resultant thermal energy ionizes and excites the atoms. This leads to an out of equilibrium state. The gas has to cool in order to return to a steady state.

A hot gas can cool various ways. The adiabatic cooling due to expansion is relatively unimportant and the radiative cooling has to be considered. A proper cooling calculation must include many different ionic species with all the possible lines (Raymond, Cox and Smith 1976; MacDonald and Bailey 1981). One key quantity is the characteristic cooling time,

$$\tau_{cool} = kT/n_e\Lambda(T) \tag{6.2}$$

where kT is the average energy of the gas, n_e is the electron number density and $\Lambda(T)$ the computed cooling function at temperature T. The cooling time, τ_{cool}, can be used to characterize how fast the radiative processes are compared to competing time-scales. Clearly, low τ_{cool} implies that there is little accumulation of heat, and thus the idealization of a constant temperature wind is valid. To justify our assumption of isothermality of hot-star winds, we require that τ_{cool} be much smaller than the characteristic flow crossing time, $\tau_{flow} \equiv R_*/v$.

The exact value of $\Lambda(T)$ depends on detailed assumptions about the composition of plasma, which usually is assumed to be optically thin. For most astrophysical fluids, we can estimate Λ as a function of temperature, T. Detailed calculations of typical astrophysical fluids show that the cooling function Λ has a maximum, $\Lambda_{max} \approx 10^{-22}$ erg cc/sec, at temperature near 10^5K (Raymond, Cox and Smith 1976), where the cooling is dominated by collisional excitation of abundant lithium-like atoms. Below this temperature, Λ can be fitted roughly by a linear function, i.e. $\Lambda \propto T$. For temperatures above about 3×10^5K, Λ declines slowly as a power law, $\Lambda \propto T^{-1/2}$. Figure 6.1 shows an example of such a cooling function adopted from Raymond, Cox and Smith (1976).

6.1.1 Column Density for Cooling Layer in a Shock

Mathematically, a shock is idealized by discontinuities in density, pressure, temperature and velocity dictated by the hydrodynamic equations of motion, like the mass, momentum and energy conservation laws. In reality, such discontinuities occur over small but non-zero length and time scales. As noted earlier, the characteristic time scale for the fluid to go from initial to the final state is assumed to be short relative to other competing dynamical timescales. This is equivalent to the requirement that the characteristic length scale of the shock front be small compared to the flow length scales (Zel'dovich and Raizer 1967). These length scales can be related to the particle column densities, $N = \int n\, dl$ where n is the particle number density.

Let us first estimate the column density for a shock needed for cooling. From equation (6.2) we have $\tau_{cool} \propto T/\Lambda(T)$, and from the cooling function (see figure 6.1) we have $\Lambda(T) \propto T^{-1/2}$ for $T > 3 \times 10^5$K. This implies that the characteristic cooling time, $\tau_{cool} \propto T^{3/2}$ for this range of temperatures. We know that the temperature

$T \propto v_0^2$ (eqn. 6.1) leading to $\tau_{cool} \propto v_0^3$. We can relate this to the column density by

$$N_{cool} = n\, l_{cool} \propto n\, \tau_{cool} v_0\,. \tag{6.3}$$

This implies that $N_{cool} \propto v_0^4$. Numerically, for the range of temperatures $10^6 - 10^7$ K,

$$N_{cool} \approx 7 \times 10^{17} \Big(\frac{v_0}{100\ km\, s^{-1}} \Big)^4\ cm^{-2} \tag{6.4}$$

(Castor 1987).

Recent *Chandra* observations show that the x-ray emission from θ^1 Ori C and τ Sco is quite hard, of the order a few keV which corresponds to the velocity jump shock $v_0 \approx 1000$ km/s and temperatures of ~ 15 MK (Cohen and Gagne, private communication). The characteristic cooling column density for such a shock to cool is $N_{cool} \approx 7 \times 10^{21}\, cm^{-2}$. This number will be a reference value in the analysis that follows next.

6.1.2 Competing Wind Column Density

Let us next estimate the column density for the ambient wind, N_{wind}. The assumption of isothermality is valid for $N_{wind} \gg N_{cool}$. By definition the column density of the wind at radius r is,

$$\begin{aligned} N_{wind} &\equiv \int_r^\infty n\, dr \\ &= \frac{\dot{M}}{4\pi v_\infty m} \int_r^\infty \frac{dr}{r^2 (1 - R_*/r)^\beta}\,, \end{aligned} \tag{6.5}$$

where m is the mean molecular weight. In the second line of the above equality, we used $\rho = n\, m = \dot{M}/4\pi r^2 v$ with an assumed β-velocity law $v(r) = v_\infty (1 - R_*/r)^\beta$. For the simple cases of $\beta = 0$ and $\beta = 1$, this can be integrated analytically. For $\beta = 1$ case,

$$N_{wind}(r) = \left[\frac{\dot{M}}{4\pi v_\infty m R_*} \right] \left[\ln \left(1 - R_*/r\right)^{-1} \right]\,, \tag{6.6}$$

and for $\beta = 0$ case,

$$N_{wind}(r) = \left[\frac{\dot{M}}{4\pi v_\infty m R_*} \right] \left[\frac{R_*}{r} \right]\,. \tag{6.7}$$

The spatial variation is isolated within the right square bracket and is plotted in figure 6.2 where the top curve represents the $\beta = 1$ and the bottom one represents $\beta = 0$ case. Note that for radii, $2 > x = r/R_* > 1$ this spatial dependence is of order unity, while at large radii they become arbitrarily small. Clearly, $N_{wind}(r) \ll N_{cool}$ for large radii for all winds regardless of the wind and stellar parameters, implying that the adiabatic approximation is valid for the outer wind. However, for the inner wind, $N_{wind}(r)$ is approximately equal to the constant term in the left square bracket, which therefore can determine whether the particle column density of the wind is high enough to validate the approximation of an isothermal wind. Thus, we define a characteristic wind particle density,

$$N_* \equiv \frac{\dot{M}}{4\pi v_\infty m R_*} \,. \tag{6.8}$$

For the standard ζ Pup model with $\dot{M} \sim 2.6^{-6} M_\odot/\mathrm{yr}$, $m = 1.0 \times 10^{-24}\mathrm{gm}$ and $v_\infty \sim 2500$ km/s this gives $N_* \sim 5 \times 10^{22}\mathrm{cm}^{-2}$. This is comparable to $N_{cool} \sim 7 \times 10^{21}$ cm^{-2}, typical of 1000 km/s shocks, implying that radiative cooling may be important.

For dense winds with $N_* \gg 7 \times 10^{21}\, cm^{-2}$ the assumption of an isothermal wind is a good one. For the less dense winds with $N_* \ll 7 \times 10^{21}\, cm^{-2}$ the adiabatic approximation is more appropriate. For the winds in the intermediate regime, full energy equation with a proper cooling function is necessary.

6.1.3 Thermal Conduction

Another mechanism for cooling hot gas is via thermal conduction, which we ignore in this work, but which can be important under certain circumstances. In a classic paper, Spitzer (1962) showed that in an *unmagnetized* plasma, the thermal conduction has a diffusion constant, $\kappa_{Sp} \sim \lambda\, v_t \propto T^{5/2}\, n^{-1}$, where λ and v_t are the mean free path and the thermal speed of electrons with number density n. This is

related to the thermal conductivity, $K = n\, k_B\, \kappa_{Sp}$, which can be approximated by $K \approx 10^{-6} T^{5/2}$ in cgs units.

In order to understand the relative importance of the thermal conduction in hot-star winds, let us do the following dimensional analysis. Consider the equation for the internal energy e with thermal conduction included,

$$\rho \frac{D}{Dt}\left(\frac{e}{\rho}\right) = -p\nabla\cdot\mathbf{v} - \nabla\cdot(K\nabla T)\,, \tag{6.9}$$

where v is the characteristic flow velocity. If the characteristic length scale is L, then we can compare the conduction to the adiabatic expansion term on the RHS:

$$x = \frac{KT/L^2}{pv/L} \sim \frac{10^{-6}T^{7/2}/L}{\rho v k/\mu} \tag{6.10}$$

where μ is the mean molecular weight, and k is the Boltzmann constant. For typical values of $\dot{M} = 3\times10^{-6} M_\odot/\mathrm{yr}$, temperature $T = 40,000$ K and length scale $L = R_* \sim 10^{12}$ cm, this ratio is very tiny, on the order $x \sim 10^{-10}$, implying that the thermal conduction can be ignored for most of the wind.

However, for the magnetically channeled wind outflows modeled in this thesis, the situation can be quite different, most notably behind strong shocks, where temperatures can exceed 10^7 K, implying a thermal conductivity that can be more than 10 orders of magnitude higher than in the mean wind. Given this, and the generally lower density and lower characteristic length scales in such regions, thermal conduction could significantly alter their structure, e.g. by smoothing out temperature contrast. Unfortunately, proper inclusion of conduction in shock-heated regions can be quite complex (see, e.g., Lyu & Kan 1986 and Saxton & Wu 2001). As it thus seems beyond the scope of this thesis, it will be left for future study.

6.2 Line-Force for Non-Isothermal Models

The ionization state of shock-heated gas can change with the increase of temperature. This can affect the line force, which depends strongly on the number

of lines available. Let us describe how the line force is modified in such a non-isothermal hot-star wind.

In all our work thus far, we used 1D radial CAK line-force of the following form (see eqn 2.87):

$$g_{lines} = \frac{f}{(1-\alpha)} \frac{\kappa_e L \bar{Q}}{4\pi r^2 c} \left(\frac{dv/dr}{\rho c \bar{Q} \kappa_e} \right)^{\alpha} . \tag{6.11}$$

The meaning of all the symbols here have been discussed in §2.5.4 and §3.2.2. It was assumed that the ionization state of the plasma remained constant throughout the wind. But the adiabatic wind models we deal with here can become quite hot, leading to a change in the ionization state which in turn can reduce the line force due to fewer available lines. Here we approximate this reduction in the strength of the line force by adding a temperature weighted exponential factor to equation 6.11,

$$g_{lines} = \frac{f}{(1-\alpha)} \frac{\kappa_e L \bar{Q}}{4\pi r^2 c} \left(\frac{dv/dr}{\rho c \bar{Q} \kappa_e} \right)^{\alpha} e^{1-T/T_{eff}} , \qquad T \geq T_{eff} . \tag{6.12}$$

where T is the local temperature of the gas, assumed equal to at least the effective temperature of the star, T_{eff}. We assume that the photo-ionizing heating does not allow the gas to cool below the effective temperature of the star, $T \geq T_{eff}$.

Note that, for high temperatures the radiation force approaches zero asymptotically. This implies that once the gas becomes hot, the line-force is inefficient in driving, leading to possible stagnation.

6.3 Energy Equation

An important component of the adiabatic MHD models of hot-star winds is the energy equation. Because of the radiative processes, the energy equation needed to integrate is,

$$\rho \frac{D}{Dt} \left(\frac{e}{\rho} \right) = -p \nabla \cdot v + H - Q , \tag{6.13}$$

where e is the specific internal energy, $e = p/(\gamma - 1)$, Q is an arbitrary cooling term assumed to be zero for the moment, and H is an external heating term. For

the adiabatic case $H = Q = 0$. In our case, we assume that the stellar luminosity keeps the wind at least at T_{eff}. Numerically, this is implemented by setting a floor temperature $T = T_{eff}$ whenever T falls below T_{eff}. The pressure $p \propto \rho^{\gamma}$ for $T > T_{eff}$, with polytropic index γ $(= 5/3)$.

6.4 Initialization of Simulations

The numerical specifications for grids and boundary conditions are identical to the ones discussed in chapter 6 with only one additional quantity, the temperature of the gas at the base to be specified which we implement at two ghost zones by fixing the temperature to the stellar effective temperature, T_{eff}.

In the adiabatic models, shocks heat the gas, and despite the adiabatic cooling due to expansion, with no radiative losses, the gas cannot cool down easily. Thus it is important to specify initial conditions in such a way as to minimize the amount of initial shocks. The isothermal 2D MHD models presented in chapter 3 & 4 were initialized by a spherically symmetric wind that was previously relaxed in a 1D simulation. Here, we evolve in time the adiabatic 2D MHD models from an initial condition at time $t = 0$ when all the MHD variables like density, flow velocity and magnetic field components are set equal to the values obtained from the end state of the corresponding isothermal models ($t = 450$ ks) with identical stellar and wind parameters. To ensure that our results do not depend on the initial condition, we run our model for at least 900 ksec which is very long compared to a characteristic flow crossing time, $t_{flow} = 5R_*/v_\infty \approx 25$ ksec.

6.5 Results and Discussion

Let us now examine the results of our 2D MHD adiabatic models for line-driven winds. The stellar and wind parameters for our models are chosen to allow direct comparison with the earlier simulations, but again the results here can be re-scaled to different sets of η_* and ω values for different stars. All the models here

use the stellar and wind parameters characteristic to ζ Pup, as listed in Table 3.1. We first confirm that for sufficiently weak magnetic confinements ($\eta_* \leq 1/10$) the results are very similar to the corresponding isothermal models with identical stellar and wind parameters.

But we find that the models with moderate to strong confinement are very different from isothermal ones. In fact, the magnetic confinement $\eta_* = 1$ seems to define a sharp transition between these two different regimes.

In the isothermal models the combination of η_* and the rotation parameter ω was important in determining the properties and configuration of the wind. In the adiabatic cases, the magnetic confinement parameter seems to be more important, as we shall see below. The amount of hot gas trapped within magnetic closed loops is determined by η_*, and when the trapped gas becomes very hot, the resultant sound speed can be comparable to flow speeds, implying that, as is the case in the solar corona, a static stratification is possible.

6.5.1 Adiabatic Models with Zero Rotation

Our approach is to evolve a self-consistent solution for a line-driven wind that takes into account an adiabatic energy equation (eqn. 6.13) with a floor temperature at $T = T_{eff}$. To determine if the new solution is different from the isothermal model, we initialize the simulation with the end state of the isothermal run, i.e. at time $t = 0$ we set all the MHD variables like density, flow velocity and magnetic field components equal to the values obtained from the end state of the corresponding isothermal models ($t = 450$ ks) with the same stellar and wind parameters.

We find that for a magnetic confinement less than unity ($1 < \eta_*$), the adiabatic models differ very little from the isothermal models with identical stellar and wind parameters discussed in chapter 3. To demonstrate this, figure 6.3 shows logarithmic color-scale of density for the isothermal (left panel) and adiabatic (right

panel) models with $\eta_* = 1/\sqrt{10} = 0.3$ with no rotation at time $t = 450$ ksec. In both cases the models relax to a steady state after about $t = 160$ ksec.

However, for confinements $\eta_* \geq 1$, the adiabatic models are very different. Figure 6.4 shows time snapshots of density (left column; logarithmic color-scale) and temperature (right column; logarithmic color-scale) of the adiabatic model with magnetic confinement $\eta_* = 1$ ($B_0 = 295$G) and zero rotation at labeled time intervals. The top row, the initial state for the adiabatic model, shows the final state for the isothermal model with identical stellar and wind parameters discussed in chapter 3.

Thus figure 6.4 illustrates the evolution of magnetic field lines (solid lines), density and temperature after the introduction of the adiabatic equation of state with $\gamma = 5/3$. This sudden change leads to numerous shocks, especially near the magnetic equator where outflows accelerated upward from opposite polarity footpoints are channeled into collision. This naturally heats the gas, which in turn reduces the line force (see eqn 6.12) since the ionization state of the plasma is increased. As a result, the hot gas stalls, which allows the field lines to reconnect as the wind flow is not strong enough to keep the field lines of opposite polarity apart. This process continues as more and more of the hot gas gets trapped in the ever growing magnetically confined region. The gas in the upper region of the closed loops is hotter than in the lower region (shock velocity jumps are higher leading to more heat release); it is also rarefied to keep the hydrostatic pressure balance within the closed region. The whole process is rather complex, and can be best illustrated through animations.

Figure 6.5 shows the final time snapshot ($t = 900$ ksec) of the thermal pressure, p (logarithmic color-scale, dyne/cm^2) for the same adiabatic model with magnetic confinement $\eta_* = 1$ and zero rotation. The gas within the closed loops is static with nearly constant pressure. This is in contrast to the isothermal models, where

a hydrostatic corona is not possible due to low sound speed, and the gravity pulls the compressed, stagnated material within closed loops into an infall back onto the stellar surface through quite complex flow patterns. Here, the rarefied gas gets very hot, and thus the sound speeds are high relative to gravitational escape speed. The relatively low densities and low flow speeds, implying low kinetic energy density, allow the closed magnetic loops to remain static.

For the isothermal models, the magnetic field influences the wind by enhancing the density and decreasing the flow speed near the magnetic equator. In the case of the adiabatic winds, we find that the equatorial region is rarefied with still decreased flow speed. Figure 6.6 shows the mass flux ($= \rho v_r$) (top panel) and the radial velocity (bottom panel) for the adiabatic model with $\eta_* = 1$ and no rotation at the maximum radius of our computational domain, $r = R_{max} = 6R_*$ normalized to the values of the isothermal non-magnetic case. The integrated net mass loss rate for this model is about $\dot{M} = 6.8 \times 10^{-7}\, M_\odot/\mathrm{yr}$, which is about 1/4 of the mass loss rate for the corresponding isothermal case with identical stellar and wind parameters.

In isothermal models, the density jumps across shocks can be arbitrarily high, while for the adiabatic models with the polytropic index $\gamma = 5/3$ the the density jump is at most factor 4 only (Zel'dovich and Raizer 1966). Thus, for isothermal models it is possible to have a very thin and dense equatorial disk-like structure. For the adiabatic models, the nature of shocks limits how dense the equatorial compression can be. In addition, because the blotted out magnetic closed loops inhibit mass outflow from the stellar surface, the open region above the loops is filled in by material flowing from a limited area in the mid-latitudes. This implies that relatively small amount of mass fills in a large volume, leading to the rarefied equatorial regions seen in our simulations.

A natural question to ask next is: how does the above solution depend on the

initial condition? There is no simple answer to this question since the amount of hot gas can depend strongly on the initial condition. However, we tested our simulations using a different set of initial conditions, e.g. using 1D relaxed CAK solution to initialize 2D spherically symmetric wind; and we arrived to similar solutions. Figure 6.7 shows the final time snapshot of density and temperature (logarithmic color-scale) superimposed with the magnetic field lines (solid lines) for two models with $\eta_* = 1$ and no rotation that were initialized differently. The first model (top panels) was initialized with the end state of the isothermal run with identical stellar and wind parameters, the standard approach in the models presented in this chapter. While the second model (bottom panels) was initialized with a previously relaxed, 1D spherically symmetric CAK wind along with a dipole magnetic field. Clearly, the overall wind structures are similar. Note that the low density regions at the top of the loops are very hot since small amount of heat can lead to high temperatures.

It appears that the magnetic confinement parameter η_* is the key value that determines the overall properties of the solution, although the details may be dependent on the initial condition.

6.5.2 Adiabatic Models With Rotation

Let us now examine how rotation can affect the adiabatic hot-star wind models. Figure 6.8 shows time snapshots of density (left column; logarithmic color-scale) and temperature (right column; logarithmic color-scale) of the adiabatic model with magnetic confinement $\eta_* = 1$ ($B_0 = 295$ G) and rotation $\omega = 1/2$ (250 km/s) at labeled time intervals. The top row represents the final state for the isothermal model with identical stellar and wind parameters discussed in chapter 3, and which is also the initial condition for the simulations here. The ranges for the density and temperature have been chosen to match the ranges of the figure for the adiabatic model without rotation (figure 6.4) to facilitate the direct comparison. Overall evolutions of the magnetic field (solid lines), density and temperature are similar to

the adiabatic case with no rotation. However, there are noticeable differences, e.g. the extent of the last magnetic closed loop is significantly smaller compared to the adiabatic model with no rotation.

The gas trapped within the closed loops co-rotates with the star, and if the outward centrifugal force is larger than the inward pull of gravity, the gas can tear through the field lines. However, the maximum radius of the closed loops here can extend beyond the co-rotation radius r_c because of the low density of the wind within the closed loops, which does not provide enough kinetic energy density necessary to break through the field lines.

Note that the highest temperatures within the magnetically confined region is lower than in the case with no rotation. The main reason is that the rotation reduces the effective gravity lowering the outflow velocities implying lower shock velocity jumps. This leads to lower shock temperatures.

The figure 6.9 shows the mass flux ($= \rho v_r$) (top panel) and the radial velocity (bottom panel) for the adiabatic model with $\eta_* = 1$ and rotation $\omega = 1/2$ (250 km/s) at $r = R_{max}$ normalized to the values of the isothermal non-magnetic case. The integrated net mass loss rate for this model is about $\dot{M} = 1.3 \times 10^{-6}\, M_\odot/\mathrm{yr}$, which is about 1/3 of the mass loss rate for the corresponding isothermal case with identical stellar and wind parameters, and about 1/2 of the non-magnetic case. This also supports the general notion that rotation increases the mass loss rates and lowers the outflow velocities.

Figure 6.10 shows time evolution of density (left column) and temperature (right column) of another adiabatic model with magnetic confinement $\eta_* = 6.4$ ($B_0 = 800$ G) and rotation rate $\omega = 1/2$ (250 km/s). The magnetic field configuration reaches an equilibrium within ∼300 ksec. Again, rotation plays an important role in shaping the field lines; it reduces the extent of the closed loops compared to the adiabatic models with zero rotation. However, compared to the isothermal

model with identical stellar and wind parameters (top row), the extent of the last closed loop is significantly larger. Qualitatively, this model is very similar to the model described above, and as such we shall not repeat the analysis.

There is a noteworthy feature in all the adiabatic models that we discuss next. It seems that the gas outflowing near the the magnetic closure latitude, gets heated up through, perhaps magnetic reconnection or some other processes we are yet unable to determine. In any case, this leads to formation of hot 'lobes' that in the case of the models with significant rotation, are episodically ejected on dynamical timescales, $\sim$ 50 ksec. Figure 6.11 illustrates such an ejection event for the model with $\eta_* = 6.3$ and rotation $\omega = 1/2$. The top row shows the density and the bottom row shows the temperature (logarithmic color-scale) at labeled time intervals chosen to make the point more clearly. We do not understand this process very well at the moment and so further investigation is required.

6.5.3 Implication for X-ray Emission

The MHD models discussed here can be used for interpreting the detection of x-ray emission from some hot stars. In chapter 3 we applied an approximate analysis of our isothermal MHD model results to yield a rough estimates for the expected level of compressional heating and associated x-ray emission. Here, the results of our adiabatic MHD models allow us to determine x-ray production directly, although it is still not fully consistent since by assumption there is no heat loss (adiabatic), even then we wish to compute x-ray emission. For a fully self-consistent x-ray production calculation we need models that take into account the full energy equation with an accurate cooling function.

The volume rate of x-ray emitted from a hot gas of temperature T is directly proportional to the density squared, $\Upsilon \propto \rho^2$. It is appropriate to truncate the x-ray emission to a level that corresponds roughly to the maximum shock energy E_x we

are interested in (Owocki and Cohen 1999). Thus,

$$\Upsilon \propto \rho^2 \, e^{-E_x/kT_6} \, , \tag{6.14}$$

where T_6 is temperature of the gas in million degrees, and E_x is a given threshold x-ray energy.

Figure 6.12 shows time snapshots of the measure of x-ray emission above 5 MK ($E_x = 0.43$ keV) for the adiabatic models with $\eta_* = 1$ and zero rotation (left panels) and 250 km/s rotation (right panels) at labeled time intervals, plotted as logarithmic color-scale. The most x-ray production occurs near the base where the wind is the densest. But the hottest gas, the possible source of the hardest x-rays, at the top of closed loops is rarefied (see e.g figure 6.4), and thus emits very little x-ray. This is a different scenario from the x-ray production estimate for the isothermal models (see Figure 3.9) where most of the emission comes from loop tops and the dense equatorial outflow region.

The adiabatic models of hot-star winds here suggest that the cases with the magnetic confinement $\eta_* < 1$ have no x-ray emission, while for the cases with $\eta_* \geq 1$ x-rays are produced mostly near the stellar surface. Because the whole region about the magnetic equator is evacuated, absorption will be reduced if viewed along the equator.

6.6 Conclusion

We have carried out preliminary study of the adiabatic hot-star winds. Because we have not included an accurate cooling function necessary for the proper treatment of the energy equation, we do not claim this study to be complete. We summarize our initial results below:

1. The assumption of an isothermal hot-star wind is valid for the dense winds with the characteristic wind column densities, $N_* \gg 7 \times 10^{21}$ cm^{-2}. For the less dense winds with $N_* \ll 7 \times 10^{21}$ cm^{-2} the adiabatic approximation is more

appropriate. For the winds with N_* in the intermediate regime, full energy equation along with a proper cooling function must be considered.

2. In the isothermal hot-star wind model, it was assumed that the hot gas radiated away energy instantaneously. In the adiabatic models, the gas does not cool at all. Thus the adiabatic model of hot-star winds represents the opposite extreme of the idealization of an isothermal wind. In practice, one should consider something intermediate, i.e. take into account full energy equation with an accurate cooling function.

3. For the adiabatic models with the magnetic confinement parameter $\eta_* < 1$, the solutions are similar to the corresponding isothermal models with identical stellar and wind parameters.

4. The adiabatic models with the magnetic confinement parameter $\eta_* \geq 1$ are dramatically different from their isothermal counterparts. The confinement parameter $\eta_* = 1$ marks a sharp boundary for this transition.

5. Our simulations show that for the adiabatic models with the magnetic confinement parameter $\eta_* \geq 1$, the magnetically confined region is greatly extended compared to their isothermal counterparts. These regions are filled in with very hot (up to order 100 MK) low density gas that is in hydrostatic equilibrium. This is in contrast to isothermal confined region where hydrostatic atmospheres are not possible due to relatively low sound speeds, and stellar gravity pull of the compressed, stagnated material within closed loops into an infall back onto the stellar surface through quite complex flow patterns.

6. For the adiabatic models with zero rotation, unlike in the isothermal cases, there is no compressed dense, slowly outflowing equatorial disk. Instead, the region above the magnetic closed loops is very low density.

7. The net mass loss rate for the adiabatic models is reduced compared to the isothermal models.

8. Because most of the hottest gas within and above the closed loops is low density, the x-ray emission from these regions is negligible. However, a significant amount of soft x-ray may be emitted near the surface about the magnetic equator where the gas is very dense.

In the future, we plan to extend this study to include an accurate cooling function, and carry out more quantitative analysis of our results.

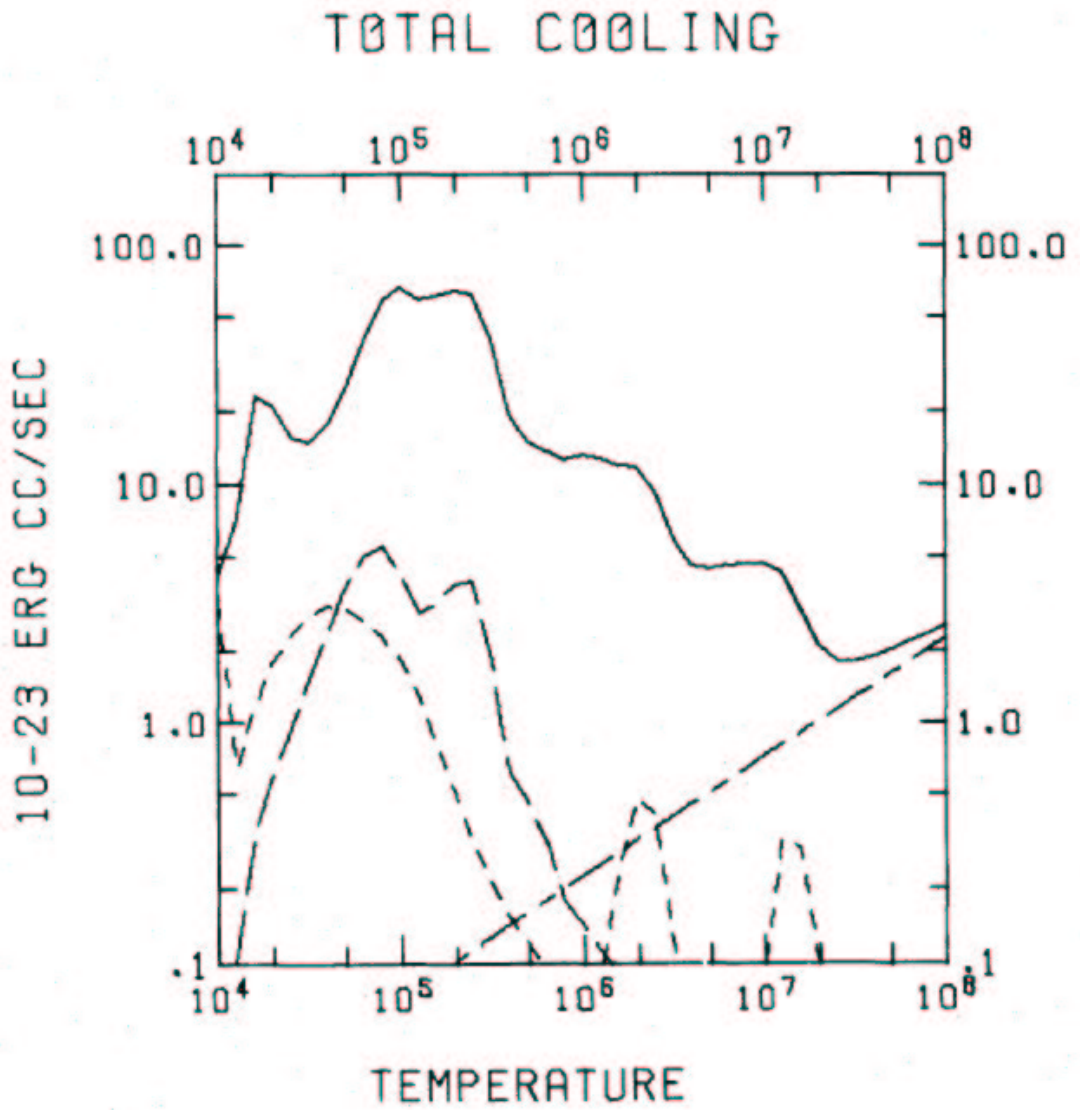

Figure 6.1: A sample cooling curve adopted from Raymond, Cox and Smith (1976). The solid line curve represents the total cooling function that include forbidden line cooling (short dashes), semiforbidden line cooling (long dashes), and bremhstahlung (long-short dashes).

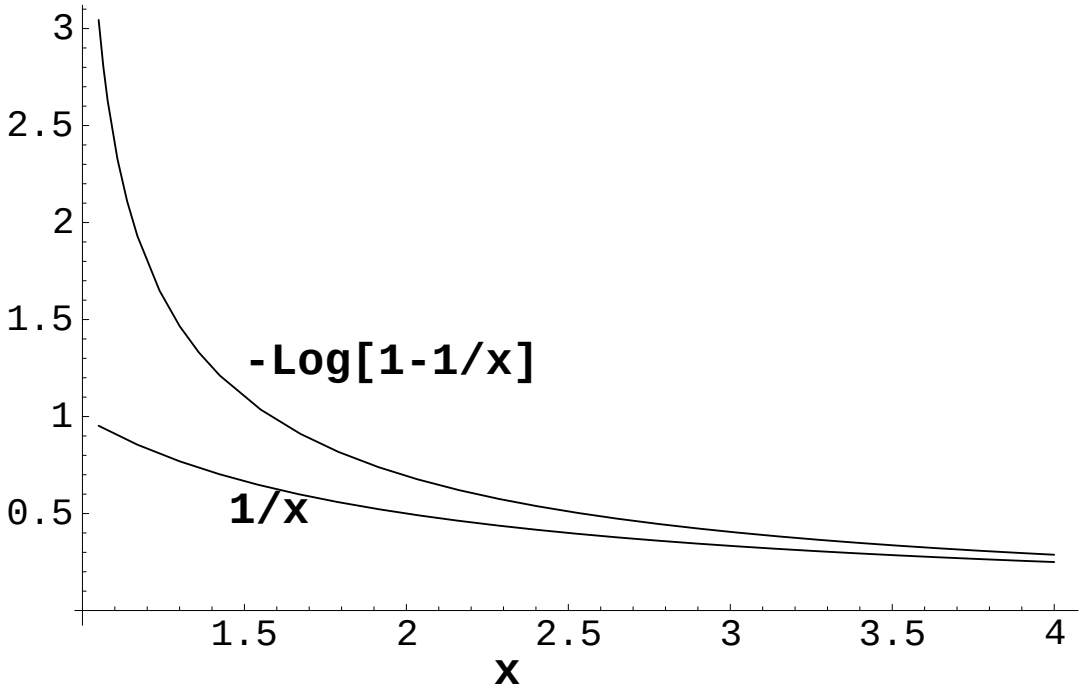

Figure 6.2: Spatial ($x = r/R_*$) dependence of N_* for the case with $\beta = 1$ (top curve) and $\beta = 0$ (bottom curve). Note that for $2 > x > 1$ both functions are of order unity.

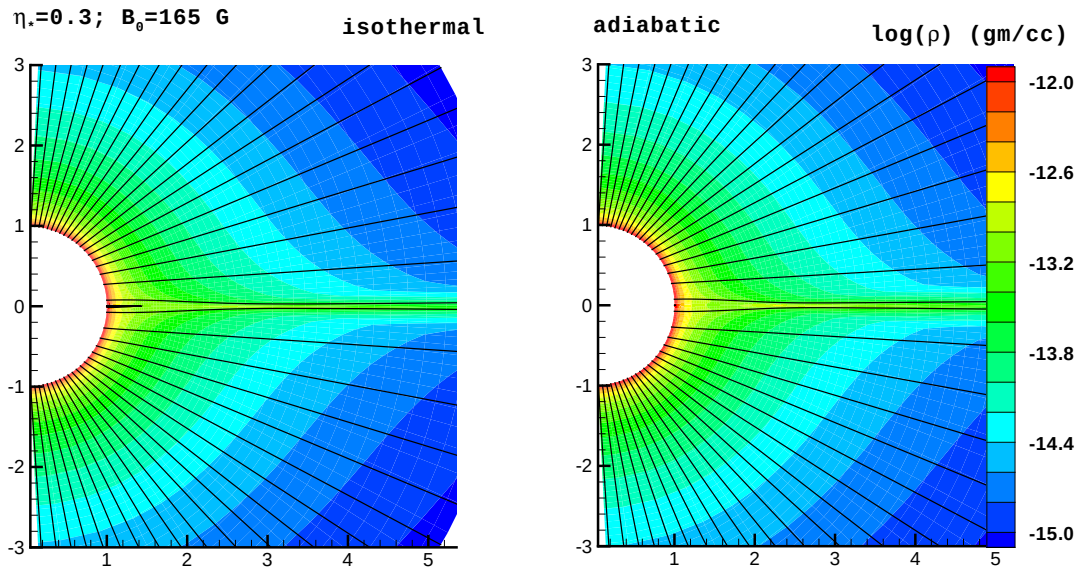

Figure 6.3: Time snapshots (t = 450 ksec) of density (logarithmic color-scale) of the isothermal (left) and the adiabatic model (right) with $\eta_* = 1/\sqrt{10} = 0.3$ and no rotation. They both reach a steady state, and are very similar. The aim here is to show that the isothermal and adiabatic models are similar for $\eta_* < 1$.

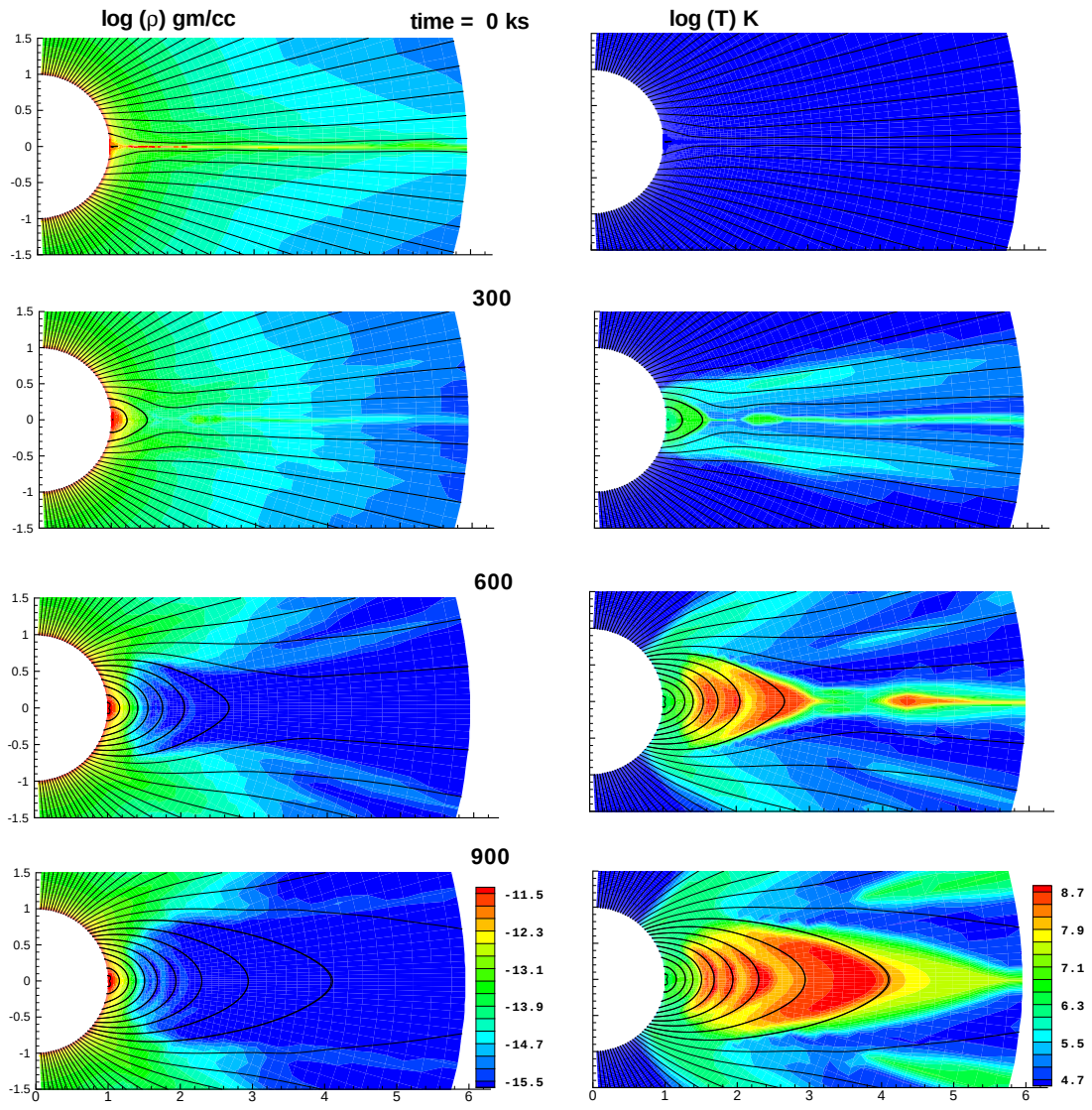

Figure 6.4: Time snapshots of density (left column; logarithmic color-scale) and temperature (right column; logarithmic color-scale) of the adiabatic model with magnetic confinement $\eta_* = 1$ and zero rotation at labeled time intervals. The top row shows the final state for the isothermal model with identical stellar and wind parameters discussed in chapter 3. The hot and rarefied gas within the closed loops are nearly isobaric (see Figure 6.5).

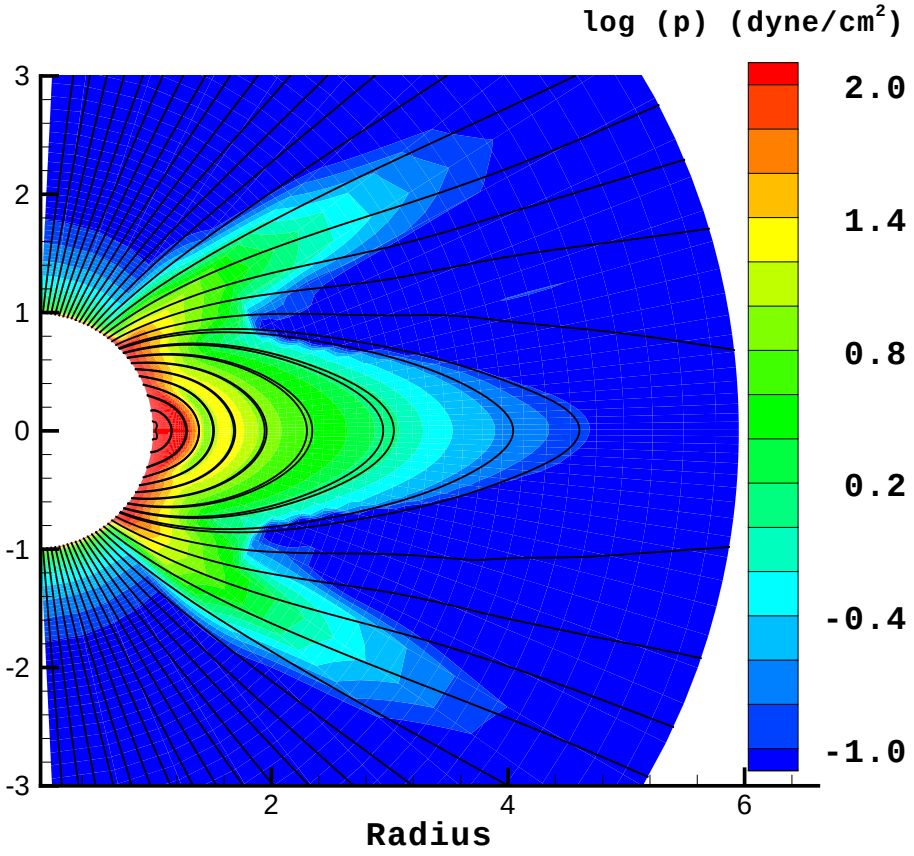

Figure 6.5: Final time snapshot ($t = 900$ ksec) of the thermal pressure (logarithmic color-scale) for the the adiabatic model with magnetic confinement $\eta_* = 1$ and zero rotation.

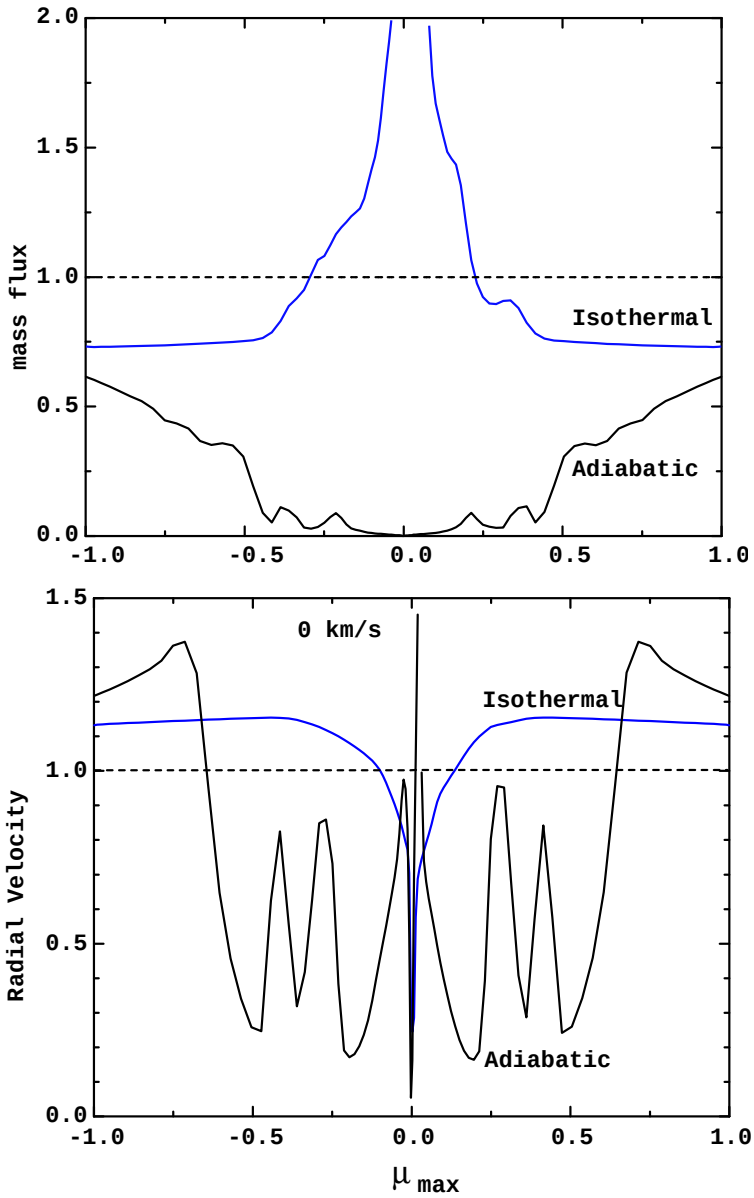

Figure 6.6: Mass flux ($= \rho v_r$) (top panel) and the radial velocity (bottom panel) for the adiabatic model with $\eta_* = 1$ and no rotation at $r = R_{max}$ normalized to the values of the isothermal non-magnetic case.

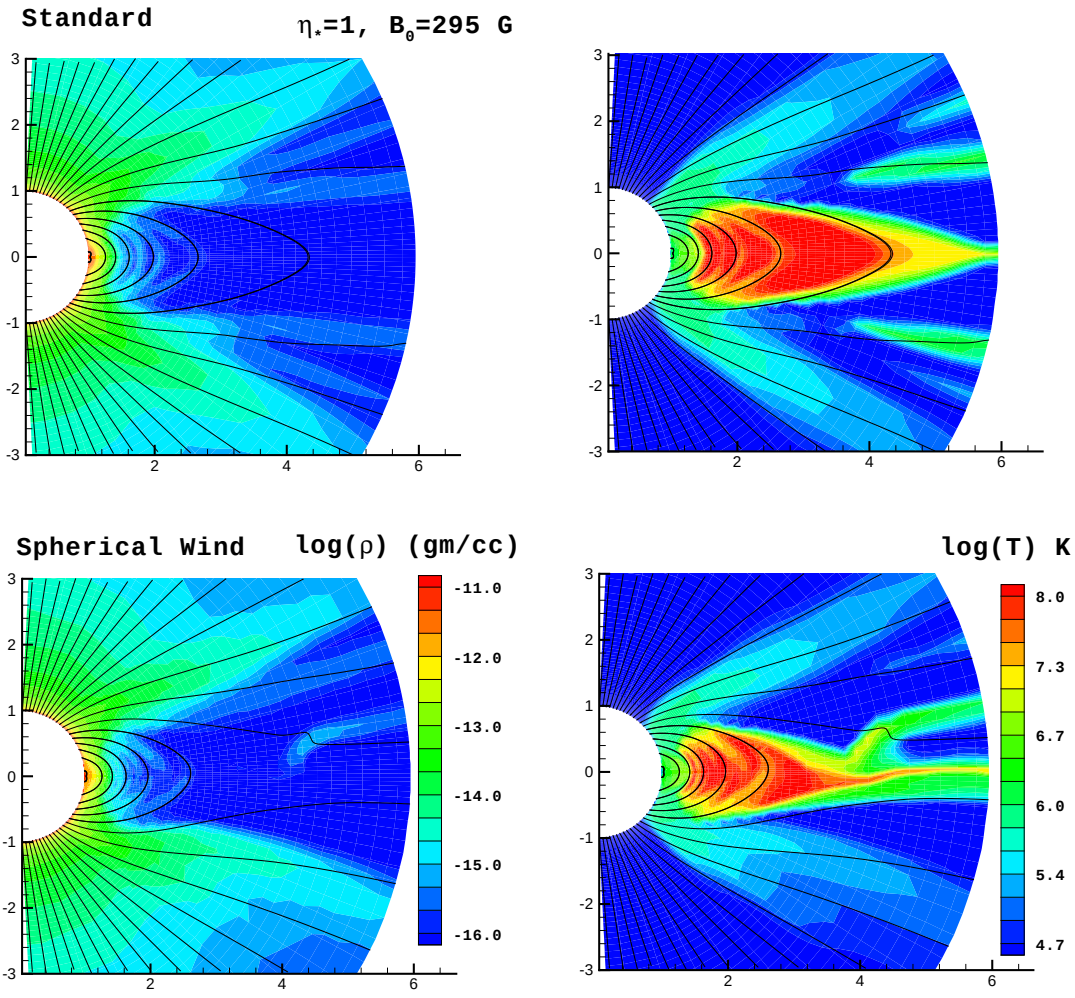

Figure 6.7: The final time snapshots of density (logarithmic color-scale) and temperature (logarithmic color-scale) of two adiabatic models with magnetic confinement $\eta_* = 1$ ($B_0 = 295$ G) and no rotation that were initialized in two different ways. The top row shows the final state for the model initialized with the end result of the isothermal run. The bottom row shows the same model initialized with a previously relaxed, 1D spherically symmetric wind and a dipole magnetic field. The solid lines represent the magnetic field lines.

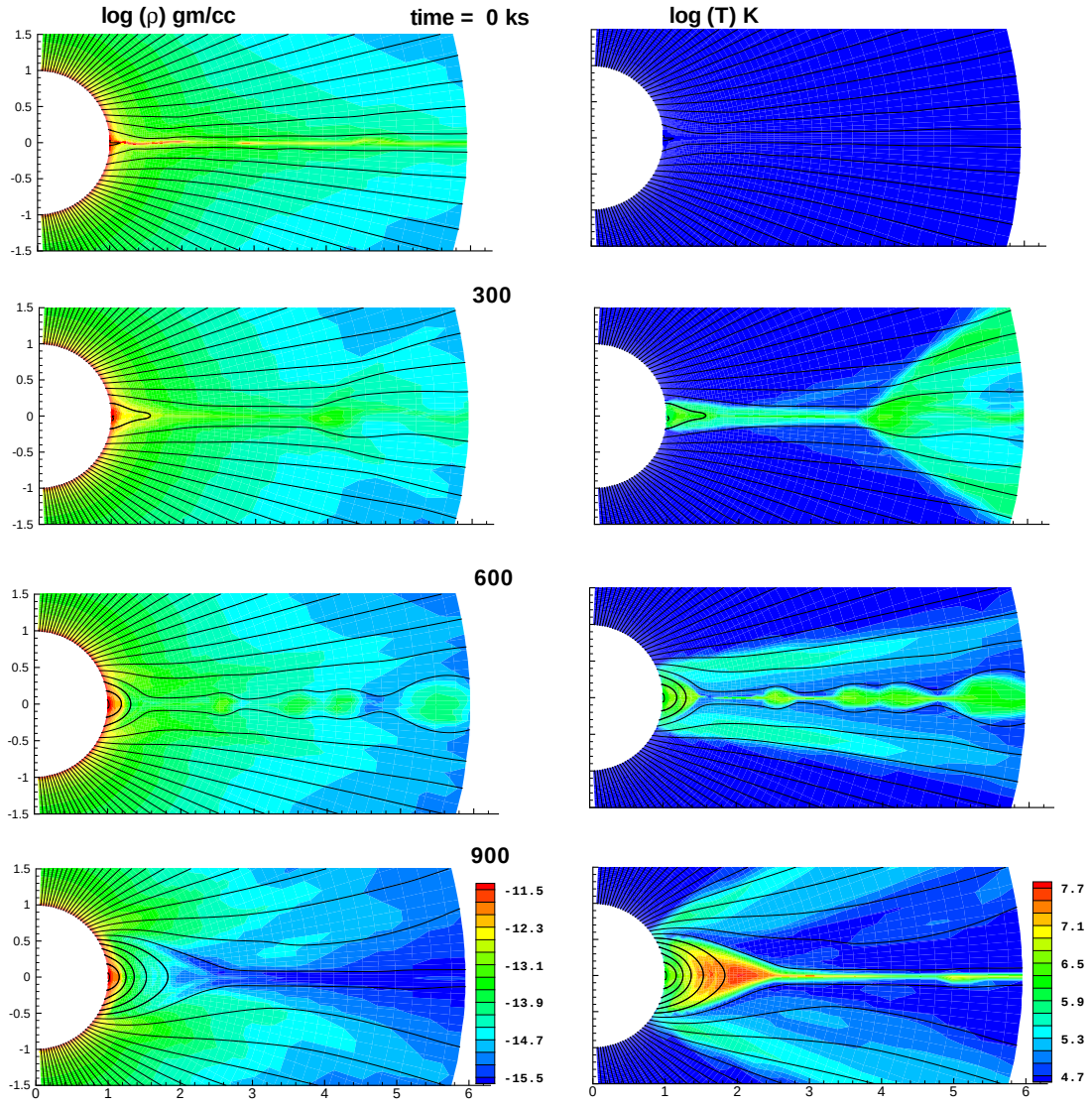

Figure 6.8: Time snapshots of density (left column; logarithmic color-scale) and temperature (right column; logarithmic color-scale) of the adiabatic model with magnetic confinement $\eta_* = 1$ ($B_0 = 295$ G) and rotation $\omega = 1/2$ (250 km/s) at labeled time intervals. The top row shows the final state for the isothermal model with identical stellar and wind parameters discussed in chapter 3.

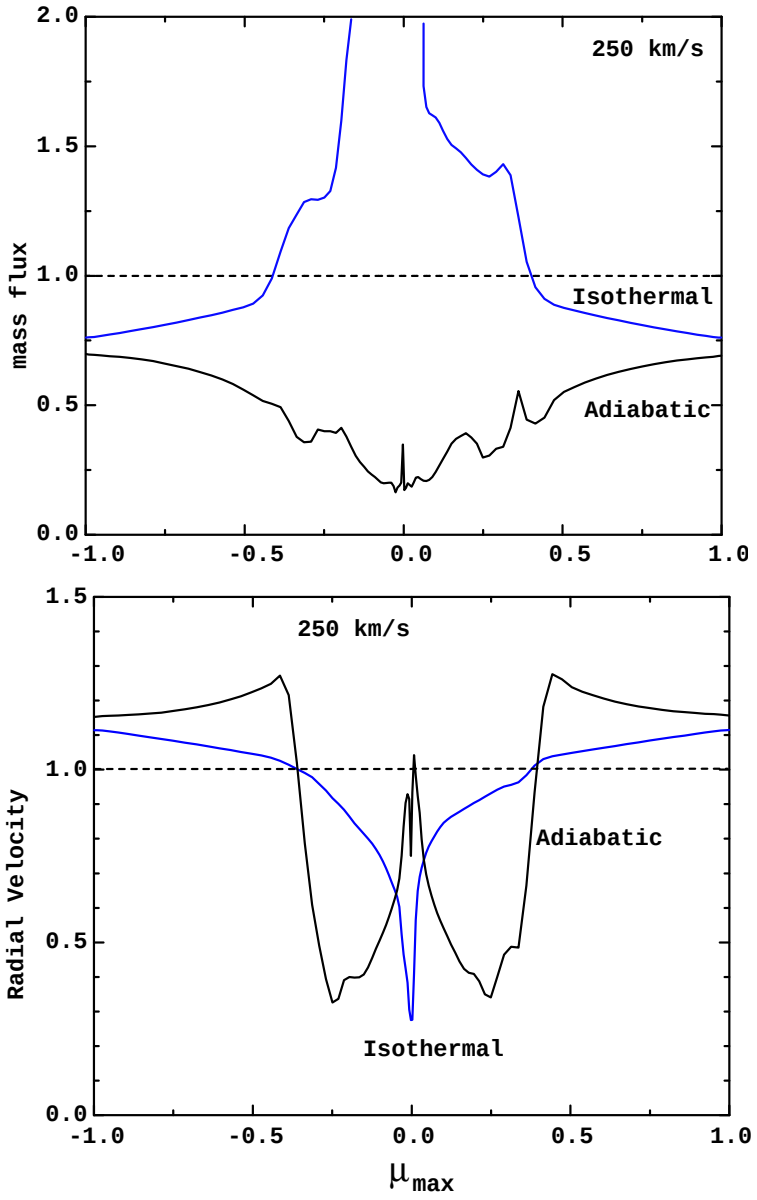

Figure 6.9: Mass flux ($= \rho v_r$) (top panel) and the radial velocity (bottom panel) for the adiabatic model with $\eta_* = 1$ ($B_0 = 295$ G and rotation $\omega = 1/2$ (250 km/s) at $r = R_{max}$ normalized to the values of the isothermal non-magnetic case.

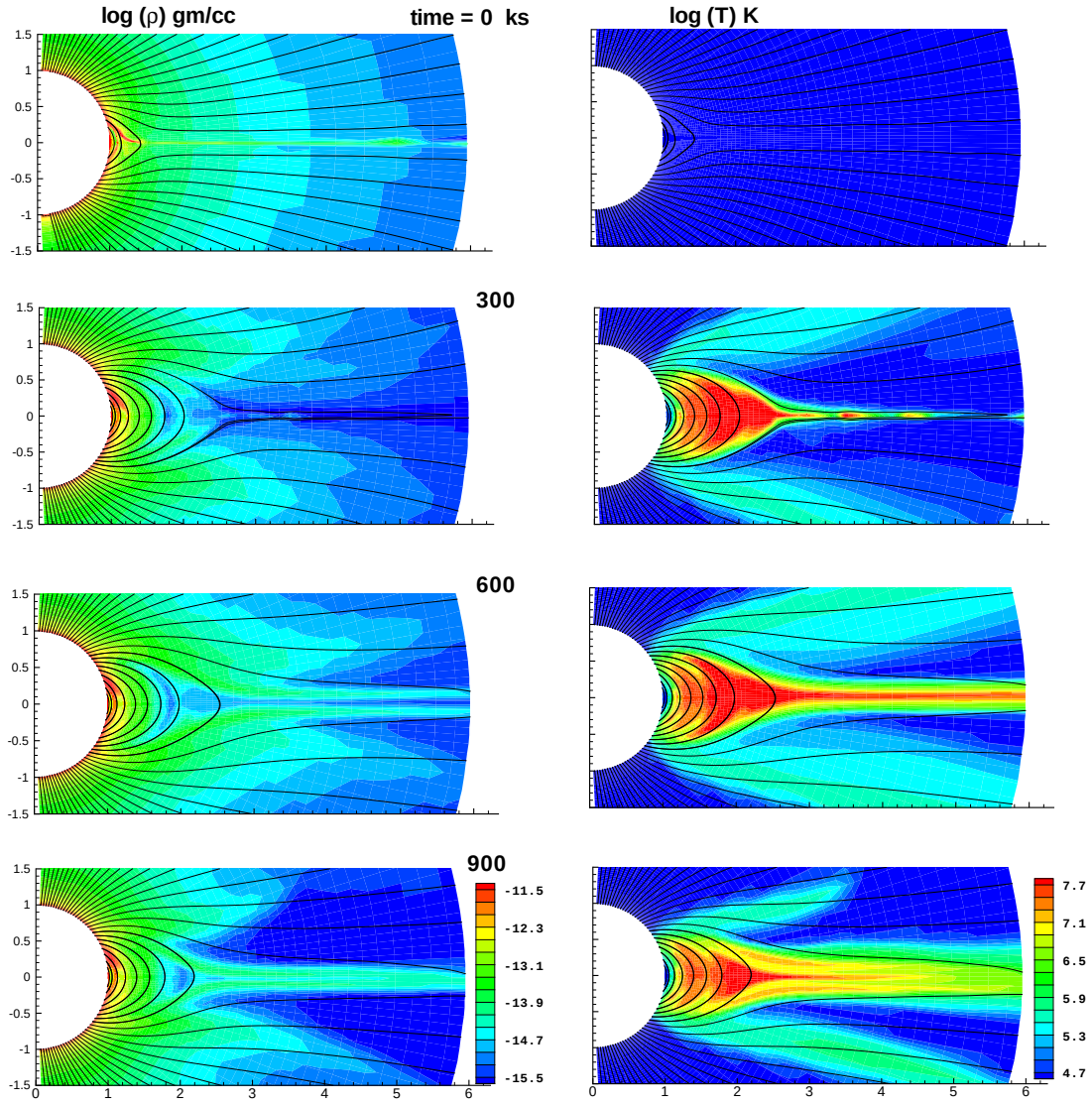

Figure 6.10: Time snapshots of density (left column; logarithmic color-scale) and temperature (right column; logarithmic color-scale) of the adiabatic model with magnetic confinement $\eta_* = 6.4$ ($B_0 = 800$ G) and rotation $\omega = 1/2$ (250 km/s) at labeled time intervals. The top row shows the final state for the isothermal model with identical stellar and wind parameters discussed in chapter 3.

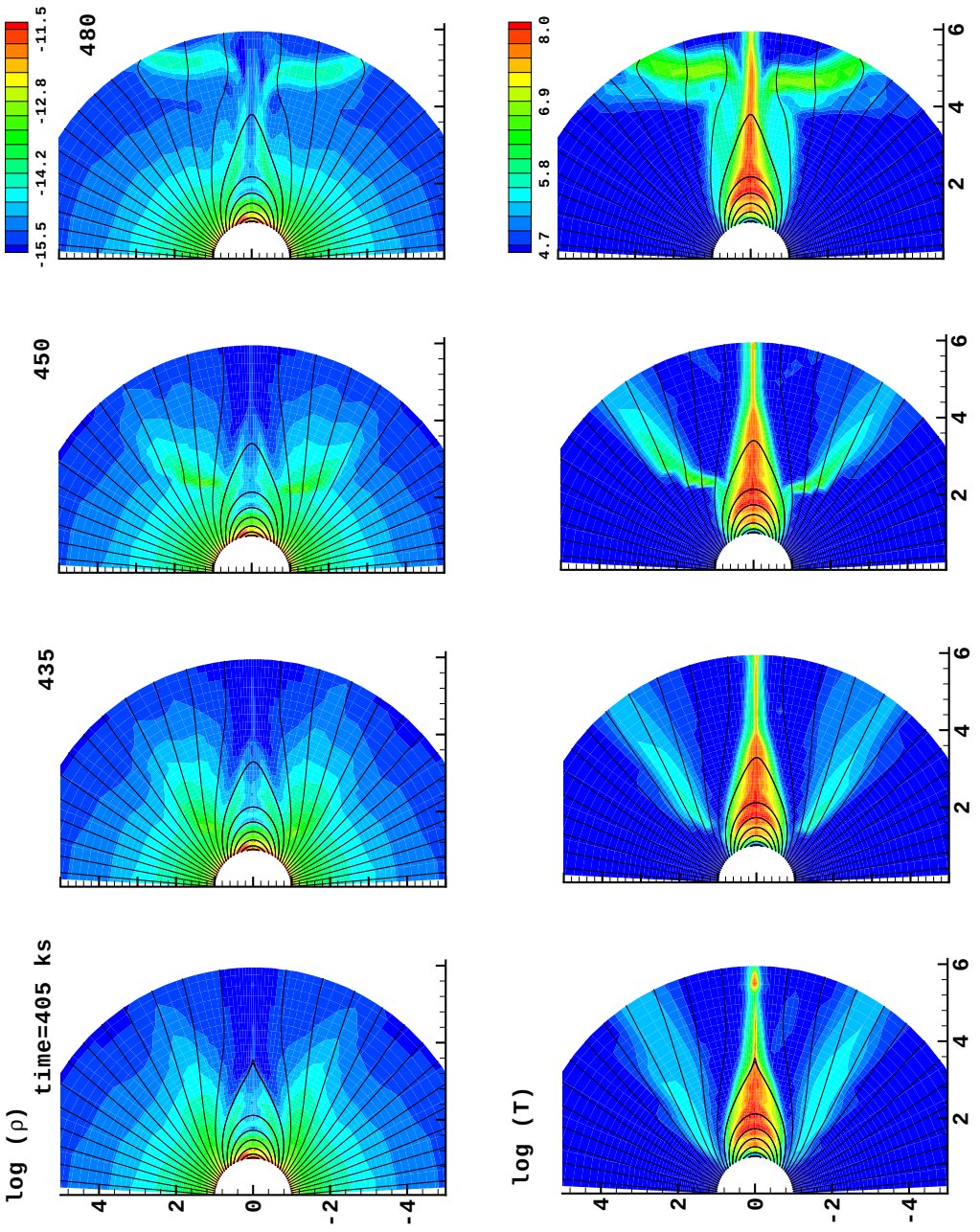

Figure 6.11: Time snapshots of density (top row; logarithmic color-scale) and temperature (bottom row; logarithmic color-scale) of the adiabatic model with magnetic confinement $\eta_* = 6.4$ ($B_0 = 800$ G) and rotation $\omega = 1/2$ (250 km/s) at labeled time intervals to demonstrate the ejection of hot 'lobes' that are formed near the magnetic closure latitude.

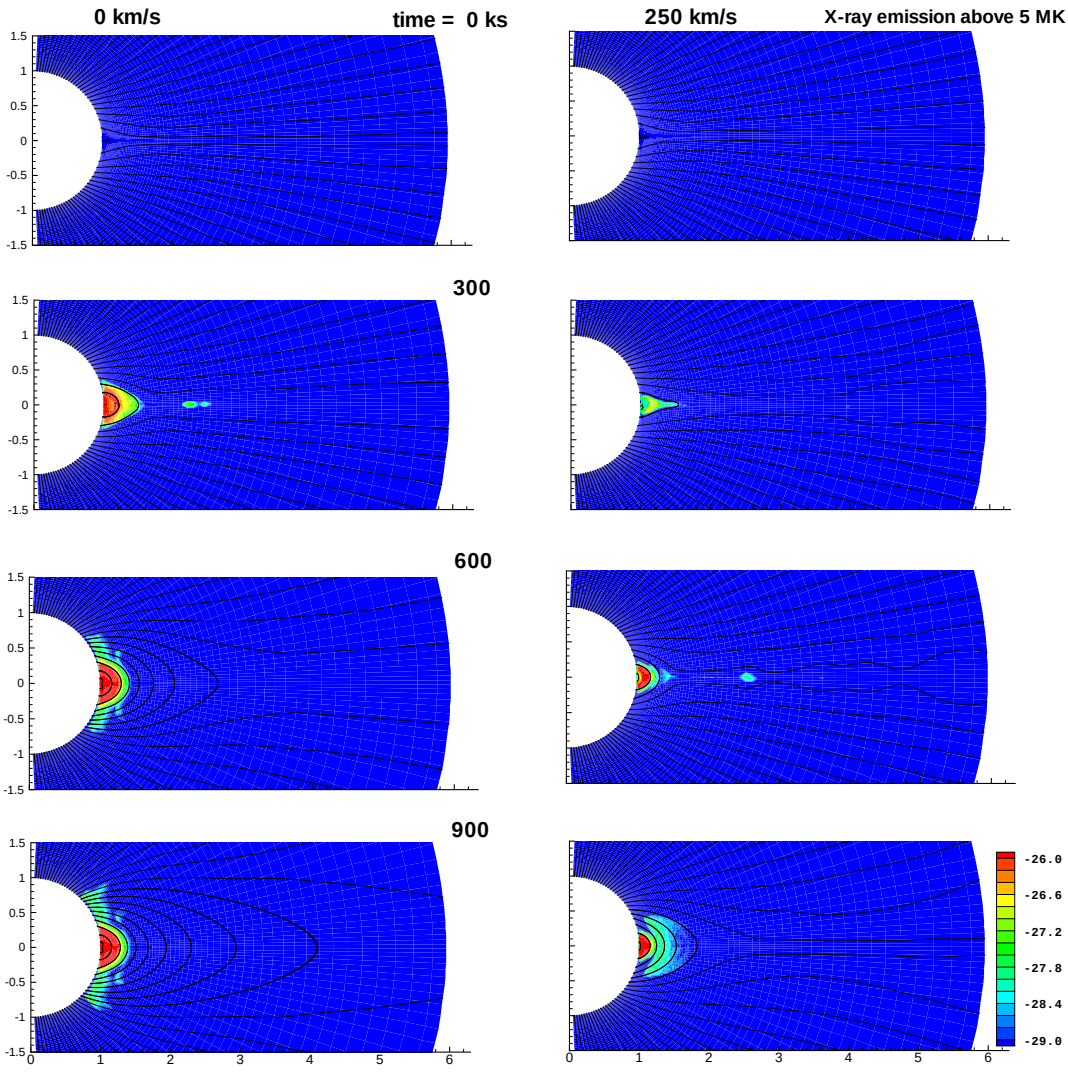

Figure 6.12: Time snapshots of the measure of x-ray emission above 5 MK for the adiabatic models with $\eta = 1$ with zero rotation (left panels) and 250 km/s rotation (right panels) plotted as logarithmic color-scale computed from $\Upsilon \propto \rho^2 \, e^{-5/T_6 \, K}$ with T_6 temperature of the gas in million degrees. Notice that the hottest gas at the top of closed loops is rarefied, and thus have very little emission. Compare this with the estimate for the isothermal models (see Figure 3.9) where most of the emission comes from loop tops and the dense equatorial outflow region. The unit here is arbitrary, the relative values are important.

Chapter 7

SUMMARY AND FUTURE WORK

7.1 Summary of the Thesis

The goal of this dissertation was to study the effect of the magnetic fields on line-driven hot-star winds. In this section we summarize the main conclusions of the thesis.

In chapter 1, we highlighted the reasons why we think that the subject of line-driven winds of early type stars is interesting. In chapter 2 we introduced the theory of line-driven winds along with a brief discussion of gas-pressure-driven solar wind . Thus we laid out the theoretical framework for the research chapters that follow.

In chapter 3 we presented numerical magnetohydrodynamic (MHD) simulations of the effect of stellar dipole magnetic fields on line-driven wind outflows from hot, luminous stars. Unlike previous fixed-field analyses, we took full account of the dynamical competition between field and flow. We showed that the key result is that the overall degree to which the wind is influenced by the field depends largely on a single, dimensionless, 'wind magnetic confinement parameter', η_* ($= B_{eq}^2 R_*^2/\dot{M}v_\infty$), which characterizes the ratio between magnetic field energy density and kinetic energy density of the wind.

For weak confinement $\eta_* \leq 1$, the field is fully opened by the wind outflow, but nonetheless for confinements as small as $\eta_* = 1/10$ can have a significant back-influence in enhancing the density and reducing the flow speed near the magnetic

equator. For stronger confinement $\eta_* > 1$, the magnetic field remains closed over a limited range of latitude and height about the equatorial surface, but eventually is opened into a nearly radial configuration at large radii. Within closed loops, the flow is channeled toward loop tops into shock collisions that are strong enough to produce hard X-rays, with the stagnated material then pulled by gravity back onto the star in quite complex and variable inflow patterns. Within open field flow, the equatorial channeling leads to oblique shocks that are again strong enough to produce X-rays, and also lead to a thin, dense, slowly outflowing 'disk' at the magnetic equator. Overall, the results in chapter 3 provide a dynamical groundwork for interpreting many types of observations – e.g., UV line profile variability; red-shifted absorption or emission features; enhanced density-squared emission; X-ray emission – that might be associated with perturbation of hot-star winds by surface magnetic fields.

Our simulations show that the polar flow is characterized by a faster-than-radial expansion that is more gradual than predicted by earlier one-dimensional flow tube analyses (MacGregor 1988) and leads to a much more modest increase in the terminal speed ($< 30\%$), consistent with observational constraints. In chapter 4 we show that a key reason behind the MacGregor (1988) terminal speed prediction of up to a factor of 3 faster than a spherical wind was the neglect of the finite-disk correction factor. In our analysis we include both the finite-disk correction and the divergence factors. With these two factors and radial tilt angle of the field and flow included, we are able to explain our numerical results not only for the polar speed, but also for the latitudinal scaling of both the speed and mass flux. In particular, we find that the even stronger increase in flow speed seen at mid-latitudes in the strongest field model ($\eta_* = 10$) does not reflect any stronger divergence factor, but rather is largely a consequence of a *reduced* base mass flux associated with a non-radial tilt of the source flow near the stellar surface. As the flow becomes nearly

radial somewhat above the wind base, the lower density associated with the lower mass flux implies a stronger line-acceleration and thus a faster terminal speed along these mid-latitude flow tubes.

Following this analysis, as a natural extension, we discuss the effects of field-aligned rotation on magnetically channeled line-driven winds in chapter 5. We find that the degree of the overall influence of rotation depends largely on the rotation speed ω expressed in the unit of critical velocity, in combination with the wind magnetic confinement parameter, η_*. Regardless of the value of magnetic confinement, for the models with $\omega \sim 1/20$ the rotation has very little effect. In general, rotation enhances the equatorial density and reduces the equatorial flow velocity.

For strong magnetic confinements for which the Alfven radius is *smaller* than the co-rotation radius, the simulations are similar to the non-rotational cases. The field remains closed in loops near the equatorial surface. Wind outflows accelerated upward from opposite polarity footpoints are guided towards a strong collision near the loop tops. The material that is stagnated as a result of this, is eventually pulled back by gravity onto the star in a complex flow pattern.

For strong magnetic confinements for which the Alfven radius is *larger* than the co-rotation radius, the situation is quite different from the the zero-rotation case. Material that is stagnated within the closed loops and lies above the co-rotation radius, is spun up to speeds such that the outward centrifugal force is larger than the inward pull of gravity. Consequently, this material punches through the field lines and is flung away. On the other hand, the material that lies below the co-rotation radius, is pulled back by the inward gravity. Thus the co-rotation radius sets an upper limit to the radius of the last closed loop for strong confinement cases.

Although the magnetic field acts as a moment arm in providing angular momentum to the wind, our numerical simulations show that, at least in the isothermal

gas approximation, it does not launch material into a Keplerian orbit. Other physical considerations need to be taken into account in order to form a stable Keplerian disk.

In the idealization of the isothermal winds, we assumed that hot gas heated in a shock radiates away its energy instantaneously. The other extreme of this scenario is the adiabatic case assuming absolutely no radiative losses. We present a few preliminary models of such winds in chapter 6. We show that the adiabatic models with the magnetic confinement parameter $\eta_* < 1$ are very similar to their isothermal counterparts. But the adiabatic models with $\eta_* \geq 1$ are very different. The magnetically confined region in these models is greatly extended compared to their isothermal counterparts. These regions are filled in with very hot (up to order 100 MK) low density gas that is in hydrostatic equilibrium, in contrast to isothermal models where hydrostatic atmospheres are not possible due to relatively low sound speeds, and stellar gravity pull of the compressed, stagnated material within closed loops into an infall back onto the stellar surface through quite complex flow patterns. We conclude that the magnetic confinement parameter η_* marks a sharp boundary for this transition.

We note that the assumption of isothermality of hot-star winds is reasonably valid for dense winds with $\dot{M} \geq 10^{-6} M_\odot/\mathrm{yr}$. To model the less dense winds properly one needs to consider full energy balance with an accurate cooling function. This is a key topic for future research.

7.2 Future Plans

The work presented in this thesis is just a step towards better understanding of the role of magnetic fields in channeling and modulating hot-star winds. As an initial study, we made a number of assumptions some of which were necessitated by limited time and computer resources, and some others to keep the physics simple.

In all our computations in this thesis, we assumed purely radial, 1D form (see eqn 3.5) for the line force, within a 2D, axisymmetric model of a non-rotating stellar wind. In the 2D wind models discussed here, the line force should in principle be modified to take account of gradients in other velocity components, such as might arise from, e.g., latitudinal flow along magnetic loops. Such latitudinal gradients can lead to a non-zero *latitudinal* component of the full vector line force. In a rotating stellar wind, asymmetries in the velocity gradient between the approaching and receding stellar hemisphere can even lead to a net *azimuthal* line force (Owocki, Cranmer, and Gayley 1996; Gayley and Owocki 2000).

We believe the effects of such non-radial forces are not likely to be significant in the context of magnetically channeled winds. However, they are important in the context of the WCD models wherein the latitudinal flow velocities were small compared to the radial values, and latitudinal forces of order only ~ 10 % can influence the wind significantly and inhibit the the disk formation (Owocki, Cranmer, and Gayley 1996). In the 2D MHD models here, the latitudinal velocities can be a substantial fraction of the radial flow, and so non-radial forces should not be as important. In addition, the magnetic field tension may inhibit the effects of these forces. Our limited tests which do take account of gradients in all directions, confirm this notion. However, more rigorous and quantitative analyses are required in future.

Another topic for our near future study is the effect of tilted rotation (with respect to the magnetic axis) on magnetically channeled hot-star winds. Our MHD simulations show that even for the models with the strongest magnetic fields, the fastest streams are not much in excess of $\sim$3000 km/s. In conjunction with the reduced flow speeds toward the magnetic equator, there is sufficient speed contrast to yield very strong CIRs, if applied in a rotating magnetic star with some substantial tilt between magnetic and rotation axes. Through extensions of the current 2D

models to a full 3D configuration, we plan in the future to carry out detailed simulations of winds from rotating hot-stars with such a tilted dipole surface field, applying these specifically toward the interpretation of observed UV line profile variability.

Most of our work here was based on the idealization of an isothermal gas. We mentioned earlier that to model hot-star winds properly one needs to consider full energy balance with an accurate cooling function. Although the approximation of isothermality may be well justified near the base of dense winds, it fails for the low density wind in the outer regions. In this thesis we presented some models of adiabatic hot-star winds with no cooling, but we plan to augment this study by including an appropriate cooling function in the future. This will enable us to compare our computed x-ray with the observed x-ray emissions from hot stars obtained by *Chandra*.

Currently, we are actively collaborating to analyze *Chandra* x-ray data for θ^1 Ori C and τ Sco in order to find a way to analytically parameterize the velocity, density, and emissivity of x-ray emitting "magnetospheres" (closed loop regions) based on MHD simulations presented in this thesis (collaborators: David Cohen, Marc Gagne and their undergraduate students).

REFERENCES

Abbott, D. C. 1982, ApJ, 259, 282

Baade, D. & Lucy, L. B. 1987, A&A, 178, 213

Babcock, H. W. 1960, ApJ, 132, 521

Babel, J. & Montmerle, T. (BM97a) 1997, A&A, 323, 121

Babel, J. & Montmerle, T. (BM97b) 1997, ApJL, 485,L29

Beals, C. S. 1929, MNRAS, 90, 202. Bjorkman, J. E. & Cassinelli, J. P. 1993, ApJ, 409, 429

Bohlender, D. A., Landstreet, J. D., & Thompson, I. B. 1993, A&A, 269, 355

Borra, E. F. & Landstreet, J. D. 1980, ApJS, 42, 421

Cassinelli, J. P., Brown, J. C., Maheswaran, M., Miller, N. A., & Telfer, D. C. 2002, ApJ, in press. 46 pages, 12 figures, 7370

Cassinelli, J. P. & MacGregor, K. B. 2000, ASP Conf. Ser. 214: The Be Phenomenon in Early-Type Stars, 337

Cassinelli, J. P., Miller, N. A., Waldron, W. L., MacFarlane, J. J., & Cohen, D. H. 2001, ApJL, 554, L55

Cassinelli, J. P. & Olson, G. L. 1979, ApJ, 229, 304

Castor, J. I. 1979, IAU Symposium 83, *Mass Loss and Evolution of O-Type Stars*, p. 175

Castor, J. I. 1987, ASSL Vol. 136: Instabilities in Luminous Early Type Stars, 159

Castor, J. I., Abbott, D. C., & Klein, R. I. 1975, ApJ, 195, 157

Chapman, S., 1957, Smithsonian Contrib. Astrophys. J., 126, 227

Charbonneau, P. & MacGregor, K. B. 2001, ApJ, 559, 1094.

Cohen, D. H., Cassinelli, J. P., & Waldron, W. L. 1997, ApJ, 488, 397

Conti, P. S. & Ebbets, D. 1977, ApJ, 213, 438

Cooper, R. G. 1994, Ph.D. Thesis, 22

Courant, R. & Hilbert, D. 1953, New York: Interscience Publication, 1953,

Cranmer, S. R., 1996, PhD Dissertation

Cranmer, S. R. & Owocki, S. P. 1996, ApJ, 462, 469

de Jong, J. A., 2000, PhD Dissertation

Donati, J.-F., Wade, G. A., Babel, J., Henrichs, H. F., de Jong, J. A., Harries, T. J. 2001, MNRAS, 326, 1265

Drew, J. E. 1989, ApJS, 71, 267

A&A, 299, 523

Feldmeier, A., Kudritzki, R.-P., Palsa, R., Pauldrach, A. W. A., & Puls, J. 1997, A&A, 320, 899

Feldmeier, A. & Shlosman, I. 2000, ApJL, 532, L125

Friend, D. B. & Abbott, D. C. 1986, ApJ, 311, 701

Fukuda, I. 1982, Publications of the Astronomical Society of the Pacific, 94, 271

Gabriel, A. H. & Jordan, C. 1969, MNRAS, 145, 241 Gagne, M., Caillault, J., Stauffer, J. R., & Linsky, J. L. 1997, ApJL, 478, L87

Gagne, M., Cohen, D., Owocki, S., & ud-Doula, A. 2001, "The X-ray Universe at Sharp Focus", eds. S. Vrtilek, E. Schlegel and L. Kuhi, ASP Conference Series References, 9090

Gayley, K. G. 1995, ApJ, 454, 410

Gayley, K. G. & Owocki, S. P. 2000, ApJ, 537, 461

Hanuschik, R. W. 1996,A&A, 308, 170

Henrichs, H. F. et al. 2000, Magnetic Fields of Chemically Peculiar and Related Stars, Proceedings of the International Meeting, held in Special Astrophysical Observatory of Russian AS, September 23 - 27, 1999, Eds.: Yu.V. Glagolevskij, I.I. Romanyuk, p.57-60, 57

Henrichs, H. F., Kaper, L., & Nichols, J. S. 1994, A&A, 285, 565

Holzer, T. E. 1977, J. Geophys. Res., 82, 23

Horbury, T. S. & Balogh, A. 2001, J. Geophys. Res., 106, 115929

Howarth, I. D. & Prinja, R. K. 1989, ApJS, 69, 527

Howarth, I. D. & Smith, K. C. 1995, ApJ, 439, 431

Howk, J. C., Cassinelli, J. P., Bjorkman, J. E., & Lamers, H. J. G. L. M. 2000, ApJ, 534, 348

Hummel, W. 1998, A&A, 330, 243

Hundhausen, A. J., 1972, Springer-Verlag, New York.

Ignace, R., Cassinelli, J. P., & Bjorkman, J. E. 1998, ApJ, 505, 910

Ignace, R., Cassinelli, J. P., & Nordsieck, K. H. 1999, ApJ, 520, 335

Ignace, R., Nordsieck, K. H., & Cassinelli, J. P. 1997, ApJ, 486, 550

Illarionov, A. F. & Sunyaev, R. A. 1975, A&A, 39, 185

Jackson, J. D., 1967, Wiley & Sons, New York.

Kaper, L., Henrichs, H. F., Nichols, J. S., Snoek, L. C., Volten, H., & Zwarthoed, G. A. A. 1996, A&AS, 116, 257

Kaufer, A. 2000, ASP Conf. Ser. 214: The Be Phenomenon in Early-Type Stars, 37

Keppens, R. & Goedbloed, J. P. 1999, A&A, 343, 251

Keppens, R. & Goedbloed, J. P. 2000, ApJ, 530, 1036

Kopp, R. A. & Holzer, T. E. 1976, Sol. Phys., 49, 43

Lamers, H.J.G.L.M. & Cassinelli, J.P., 1999, Cambridge University Press, Cambridge Long, K. S. & White, R. L. 1980, ApJL, 239, L65

Lamers, H. J. G. L. M., Waters, L. B. F. M., & Wesselius, P. R. 1984, A&A, 134, L17

Lucy, L. B. 1982, ApJ, 255, 286

Lucy, L. B. & Solomon, P. M. 1970, ApJ, 159, 879.

Lyu, L. H. & Kan, J. R. 1986, J. Geophys. Res, 91, 6771

MacDonald, J. & Bailey, M. E. 1981, MNRAS, 197, 995

MacGregor, K. B. 1988, ApJ, 327, 794

Mathias, P., Aerts, C., Briquet, M., De Cat, P., Cuypers, J., Van Winckel, H., Flanders., & Le Contel, J. M. 2001, A&A, 379, 905

Mathys, G. 1995, A&A, 293, 746

Mathys, G., Hubrig, S., Landstreet, J. D., Lanz, T., & Manfroid, J. 1997, A&AS, 123, 353

Matt, S., Balick, B., Winglee, R., & Goodson, A. 2000, ApJ, 545, 965

Miller, N. A., Cassinelli, J. P., & MacFarlane, J. J. 2000, AAS/High Energy Astrophysics Division, 32,

Milne, E. A. 1924, MNRAS, 85, 111.

Morton, D. C., 1967, ApJ, 147, 1017

Mullan, D. J. 1984, ApJ, 283, 303

Owocki, S. P. 1994, Ap&SS, 221, 3

Owocki, S. P., Castor, J. I., & Rybicki, G. B. 1988, ApJ, 335, 914

Owocki, S. P. & Cohen, D. H. 1999, ApJ, 520, 833

Owocki, S. P., Cranmer, S. R., & Blondin, J. M. 1994, ApJ, 424, 887

Owocki, S. P., Cranmer, S. R., & Gayley, K. G. 1996, ApJL, 472, L115

Parker, E. N. 1958, ApJ, 128, 664.

Pauldrach, A. 1987, A&A, 183, 295

Pauldrach, A., Puls, J., & Kudritzki, R. P. 1986, A&A, 164, 86

Peters, G. J. 1986, ApJL, 301, L61

Pizzo, V. 1978, J. Geophys. Res., 83, 5563

Pneuman, G. W. & Kopp, R. A. 1971, Sol. Phys., 18, 258

Porter, J. M. & Skouza, B. A. 1999, A&A, 344, 205

Priest, E.R.,Hood, A.W. 1991, *Advances in Solar System Magnetohydrodynamics*, Cambridge: Cambridge University Press, 1991

Prinja, R. K. & Howarth, I. D. 1986, ApJS, 61, 357

Prinja, R. K. , Massa, D., Howarth, I. D., & Fullerton, A. W. 1998, MNRAS, 301, 926.

Raymond, J. C., Cox, D. P., & Smith, B. W. 1976, ApJ, 204, 290

Rivinius, T., Baade, D., Štefl, S., & Maintz, M. 2001, A&A, 379, 257

Sakurai, T., 1985, å, 152, 121.

Saxton, C. J. & Wu, K. 2001, MNRAS, 324, 659

Shore, S. N. & Brown, D. N. 1990, ApJ, 365, 665

Smith, M. A. 2000, ASP Conf. Ser. 214: The Be Phenomenon in Early-Type Stars, 292

Smith, E. J., Balogh, A., Forsyth, R. J., & McComas, D. J. 2001, Geophys. Res. Lett., 28, 4159

Smith, M. A., Peters, G. J., & Grady, C. A. 1991, ApJ, 367, 302

Sobolev, V. V. 1960, Soviet Astronomy, 4, 372

Spitzer, L. J. 1956, ApJ, 124, 20

Spitzer, L. 1962, Physics of Fully Ionized Gases, New York: Interscience (2nd edition), 1962,

Stella, L., White, N.E., Rosner, R. 1986, ApJ, 308, 669

Stone, J. M., 1990, PhD Dissertation

Stone, J. M. & Norman, M. L. 1992, ApJS, 80, 753

Stone, J. M. Hawley, J. F., Evans, C. R. & Norman, M. L. 1992, ApJ, 388, 415

Telting, J. H., Aerts, C., & Mathias, P. 1997, A&A, 322, 493

van Leer, B. 1977, Journal of Computational Physics, 23, 276

Waldron, W. L. 1984, ApJ, 282, 256

Wang, Y.-M. & Sheeley, N. R. 1990, ApJ, 355, 726

Waters, L. B. F. M. & Marlborough, J. M. 1994, IAU Symp. 162: Pulsation; Rotation; and Mass Loss in Early-Type Stars, 162, 399

Zel'dovich, Ya. B., Raizer, Yu. P. 1966, New York: Academic Press.

Zirker, J. B. 1977, *Coronal Holes and High Speed Wind Streams*, Boulder: Colorado Associated University Press.